Out-of-equilibrium dynamics in a tuneable homogeneous Bose gas

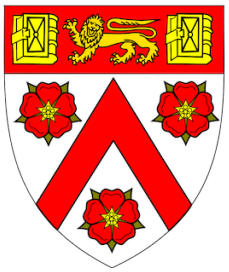

Jake Andrew Paul Glidden

Trinity College

This thesis is submitted for the degree of

Doctor of Philosophy

March 2021

Cavendish Laboratory

Department of Physics

To the memory of
my father, Craig

Declaration

This thesis is the result of my own work and includes nothing which is the outcome of work done in collaboration except as declared in the Preface and specified in the text. I further state that no substantial part of my thesis has already been submitted, or, is being concurrently submitted for any such degree, diploma or other qualification at the University of Cambridge or any other University or similar institution except as declared in the Preface and specified in the text. It does not exceed the prescribed word limit of sixty thousand words, as set out by the Physics and Chemistry Degree Committee.

Jake Andrew Paul Glidden

March 2021

Cavendish Laboratory

University of Cambridge

J J Thomson Avenue

Cambridge CB3 0HE

United Kingdom

Abstract

Out-of-equilibrium dynamics in a tuneable homogeneous Bose gas

Jake Andrew Paul Glidden

This thesis describes studies of out-of-equilibrium dynamics in an interacting homogeneous Bose gas. We use the versatile platform of an ultracold gas of ^{39}K, prepared in an optical box trap. The experiment features both tuneable interaction strengths and a homogeneous atomic density. We examine first a weakly interacting near-equilibrium system, followed by far-from-equilibrium dynamics under moderate interactions, and finally combine strong interactions with highly non-equilibrium dynamics in studies of the unitary Bose gas.

We start with a theoretical study of the effects of three-body recombination on the temperature of a weakly interacting, partially condensed gas. Contrary to the expectation of heating, we find that for appropriate values of the condensed fraction and gas parameter, the system temperature is expected to decrease. Not only do we predict lower temperatures, however, but also for the condensate fraction to grow.

We then present experiments in which we engineer a far-from-equilibrium momentum distribution, and study the dynamics as the gas relaxes. As the distribution evolves, we observe bidirectional dynamic scaling, with a flow of particles to lower momenta while energy is transported to higher ones. These flows are characterised by spatiotemporal scaling exponents, which we find do not vary appreciably over a range of moderate interaction strengths.

Finally, we look to the unitary Bose gas, quenching clouds into the strongly interacting regime. This regime offers insight into universal behaviour that depends only on the interparticle spacing, as well as being an avenue for the study of Efimov physics. However, few things come for free; strongly interacting Bose systems are plagued by high atom-loss and heating rates. We study atom-loss rates and the dynamics of correlations in our gases, isolate the coherent effects from the dissipative ones, and identify a quasi-equilibrium state that features a non-zero condensate fraction.

Acknowledgements

This thesis marks the end of several years of demanding work. The time I have spent in Cambridge has had its share of difficult moments, both from the perspective of the science itself, and as a result of the rather unexpected challenges that arose from the year that was 2020. I would like to acknowledge the support of several people who have helped to overcome these challenges, and to take this thesis from the drawing board to its current form.

First and foremost, I extend my sincere thanks to my supervisor Zoran Hadzibabic for having guided the science, and for bringing what I can only call his 'interminable enthusiasm' to the table. His inputs combine a great attention to detail with a knack for concisely distilling the crucial features of the science; both are invaluable qualities when it comes to quality research.

I also thank Rob Smith, who frequently made himself available at the drop of a hat to discuss new aspects of the physics we were studying, or to help diagnose and fix any finicky problems that arose unexpectedly in the lab. His cool and collected approach balances Zoran's eager enthusiasm, and it was a genuine privilege to have been able to work with him in the first few years of my PhD, before he took up his new position in Oxford.

From a more day-to-day perspective, I would like to acknowledge the colleagues I have worked alongside most closely in the lab. The hours that Christoph Eigen, Lena Dogra, and Timon Hilker have put in over the years not only in terms of research, but also improving and maintaining the experiment, have not gone unnoticed. I owe an enormous debt of gratitude to Chris in particular, who was for me the historical expert for our specific experiment (and indeed on some of Zoran's concepts of beauty in scientific figures that still, after four years, elude me). He has been my go-to person throughout my PhD for just about anything, and has (fortunately for me!) been very happy to engage in a lot of last-minute proofreading.

I was fortunate enough to share our lab with a number of dedicated postdocs: Raphael Lopes, Nir Navon, and Jinyi Zhang. The technical expertise they shared, the advice they provided, and verve they brought to their work made for a very stimulating lab environment.

It was a privilege to have the opportunity to work with the cold-atoms legend Eric Cornell, who spent a good deal of time with us as a visiting researcher during his sabbatical. His knowledge of the unitary regime was instrumental in shaping our own research in that area, and he brought a fresh perspective and new energy to our research efforts.

To the members of our group, past and present, working on other experiments – Jay Man, Panagiotis Christodoulou, Maciej Gałka, Julian Schmitt, Nishant Dogra, Milan Krstajić, An-

dreas von Haaren, and Nathaniel Vilas: it has been a pleasure collaborating with all of you, and hearing about the research avenues you are pursuing, more often than not over lunch in the Cavendish canteen. I share similar sentiments for the broader membership of the Atomic, Mesoscopic and Optical Physics group; there has been many a fruitful discussion in the Rutherford corridors and tea room.

Looking beyond the proverbial four walls of the lab, there are many people that have helped to make my time here in Cambridge a great one. Whilst I cannot hope to list everyone individually, I extend my thanks to the members of Trinity College & Gates Cambridge communities, as well as fellow students I've had the privilege of singing with in Cadenza, and in Fitz Barbershop. Your ears, and in some cases voices, have been an invaluable cathartic outlet that has helped to maintain my sanity during the more stressful moments of the PhD experience.

Last, but by no means least, I want to thank my family at home in Brisbane, Australia. It has been quite the challenge for us all, being separated by some $16,500\,\mathrm{km}$ and 10 time zones for most of the past four years, and life has thrown us some serious curve balls during that time. Your unwavering support and encouragement mean the world to me, and I wouldn't be where I am today without it.

Contents

1 Introduction

Quantum mechanics undeniably numbers among the most successful theories in modern-day physics. Whilst there remain several deep philosophical questions as to what quantum mechanics *means*, the predictive power of the theory speaks for itself: quantum mechanics forms the basis for our understanding of, e.g., lasers, superfluidity and superconductivity, and transistors and other semiconductor devices.

Since the early 20$^{\text{th}}$ century, descriptions of many-particle systems have been a central part of the ongoing development of quantum theory. A series of advances in laser cooling techniques from the mid 1970s through the 1980s led to the formation of the first atomic Bose–Einstein condensates [1, 2] in 1995, and degenerate atomic Fermi gases [3] shortly thereafter. This launched the research field of ultracold atomic gases, which have since become attractive experimental platforms for exploring many-body quantum mechanics. These systems offer many advantages: the gases are typically extremely well isolated from their surroundings, can be manipulated with precision-controlled lasers and magnetic fields, offer experimentally resolvable time- and lengthscales, and for some atomic species, the strength of interactions between atoms can be tuned via an external magnetic field [4]. Many of the key achievements of ultracold-atom research are reviewed in, e.g., [5–8].

In this thesis we focus on ultracold Bose gases. These gases have the rather unusual property that, at low temperatures, they can undergo a statistical phase transition to form a Bose–Einstein condensate, in which the quantum-mechanical ground state is macroscopically occupied. The equilibrium behaviour of these gases is generally well understood, in particular when interactions between particles are weak. Here, we instead explore the gas' non-equilibrium behaviour at interaction strengths ranging from completely non-interacting through to the strongly interacting and strongly correlated unitary regime. We conduct our experiments using ultracold gases of ^{39}K in a quasi-

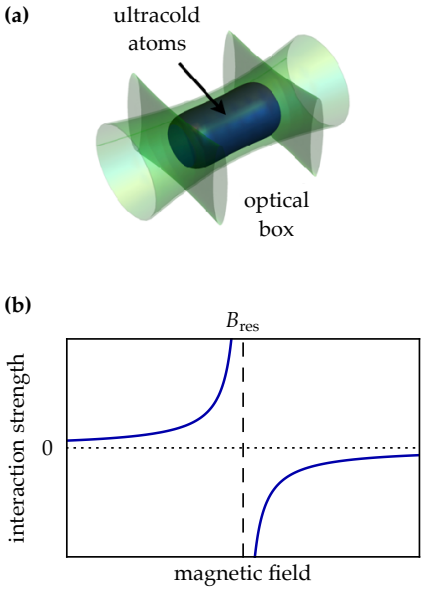

Figure 1.1 | **Key features of our experimental platform.** The combination of **(a)** a uniform trapping potential and **(b)** the ability to tune the interparticle interaction strength allows us to study a range of many-body quantum phenomena in a textbook setting.

uniform optical box potential [9–11]; this platform combines the aforementioned tuneability of the strength of interactions between atoms with a homogeneous gas density (Fig. 1.1).

Uniform box potentials are gaining popularity (e.g., [12–14]) over their more traditional harmonic counterparts, which are more easily realised in experimental settings. Theoretical work often assumes a homogeneous atomic density, e.g., in infinite-system limits, or by enforcing periodic boundary conditions. Whilst methods have been developed to extract uniform-system properties from harmonically trapped samples[1], these techniques are expected to break down for non-equilibrium or critical phenomena, where long-range correlations in the gas become significant. The use of a uniform potential facilitates direct comparison with theory, in particular in these latter cases.

1.1 Thesis outline

This thesis is structured as follows. We begin with a brief introduction to the theory of Bose gases in chapter 2, followed by an overview of our experimental platform in chapter 3. Chapters 4 to 6 closely follow the four papers [15–18]. Chapter 4 introduces our theoretical study of three-body recombination in both ideal and weakly interacting gases; we show that three-body loss, which is traditionally associated with heating, can counterintuitively give rise to a cooling effect. In chapter 5 we turn to the critical dynamics of a far-from-equilibrium Bose gas. Here we observe dynamic scaling in the evolution of the gas that is reminiscent of the behaviour of near-equilibrium gases in the vicinity of a second-order phase transition. Chapter 6 explores the unitary Bose gas, in which interactions between particles are as strong as allowed by quantum mechanics, and the gas displays universal behaviour dependent only on the interparticle spacing. Finally, in chapter 7 we briefly describe some of our future research avenues.

[1] Generally, this involves considering the system as a collection of smaller, locally homogeneous units. Using this *local density approximation* in harmonic systems can be advantageous, since under appropriate conditions one could measure the uniform-system properties at multiple different effective potentials simultaneously.

1.2 Publications during candidacy

A list of publications that have arisen during my candidacy as a PhD student is provided below. These papers explore various aspects of out-of-equilibrium phenomena in a uniform Bose gas, ranging from a weakly interacting gas that remains close to equilibrium, through to a gas quenched into the strongly interacting unitary regime, where the very nature of a possible equilibrium state remains an open question. The work presented in this thesis closely follows the first four of these papers.

- C. Eigen, J. A. P. Glidden, R. Lopes, N. Navon, Z. Hadzibabic, and R. P. Smith. *Universal Scaling Laws in the Dynamics of a Homogeneous Unitary Bose Gas*. Phys. Rev. Lett. **119**, 250404 (2017).

- C. Eigen, J. A. P. Glidden, R. Lopes, E. A. Cornell, R. P. Smith, and Z. Hadzibabic. *Universal prethermal dynamics of Bose gases quenched to unitarity*. Nature **562**, 221 (2018).

- L. H. Dogra, J. A. P. Glidden, T. A. Hilker, C. Eigen, E. A. Cornell, R. P. Smith, and Z. Hadzibabic. *Can Three-Body Recombination Purify A Quantum Gas?* Phys. Rev. Lett. **123**, 020405 (2019).

- J. A. P. Glidden, C. Eigen, L. H. Dogra, T. A. Hilker, R. P. Smith, and Z. Hadzibabic. *Bidirectional dynamic scaling in an isolated Bose gas far from equilibrium*. Nat. Phys. **17**, 457 (2021).

- J. Zhang, C. Eigen, W. Zheng, J. A. P. Glidden, T. A. Hilker, S. J. Garratt, R. Lopes, N. R. Cooper, Z. Hadzibabic, and N. Navon. *Many-body Decay of the Gapped Lowest Excitation of a Bose–Einstein Condensate*. Phys. Rev. Lett. **126**, 060402 (2021).

- T. A. Hilker et al. *First and second sound in a compressible Bose fluid*. In preparation.

2 Theoretical background

This chapter provides an overview of the theoretical concepts that form the basis for the remainder of the thesis. Here we focus on the equilibrium properties of Bose gases comprising a large number of particles. We first present conceptual arguments leading to the quantum statistics that underpin the phenomenon of condensation developed by Bose and Einstein almost a century ago [19–21]. We will then make use of the Bose–Einstein distribution to calculate thermodynamic properties of non-interacting ultracold Bose gases in geometries relevant for our experiments, as well as providing a brief introduction to both interatomic interactions and the nature of excitations above the condensate. Finally, we give an overview of the spatial correlation functions and their applications in the context of this thesis. The bulk of this chapter echoes arguments provided in several graduate physics texts, for example [22, 23].

2.1 Distinguishability

We work with a three-dimensional gas consisting of identical, indistinguishable atoms, at temperatures where quantum mechanical effects influence the distribution of those atoms amongst the available energy states. To illustrate the main concept, let us consider a pair of such indistinguishable particles, and write down their joint wavefunction. Denoting the states of the two particles (s_1, s_2), and their corresponding single-particle wavefunctions (ψ, φ), a first naïve attempt for such a wavefunction might be a straightforward product of the form

$$\Psi(s_1, s_2) = \psi(s_1)\varphi(s_2)\,. \tag{2.1}$$

If the two particles are indeed identical, then swapping them should give a physically equivalent wavefunction that differs at most by a global phase θ, i.e.,

$$\Psi(s_2, s_1) = \exp(-i\theta)\Psi(s_1, s_2)\,. \tag{2.2}$$

Moreover, swapping them a second time must yield the original wavefunction without any additional phase, i.e.,

$$\Psi(s_1, s_2) = \exp(-2i\theta)\Psi(s_1, s_2)\,, \tag{2.3}$$

which implies that either $\theta = 0$ or $\theta = \pi$. The combined wavefunction of two identical particles must therefore either remain unchanged (symmetric), or change *only* its sign (antisymmetric),

under exchange of the particles. This argument is readily extended to systems comprising more than two particles; exchanging *any* two particles twice must leave the wavefunction unchanged.

The canonical representation of the joint wavefunction encodes this symmetry explicitly, by revising our attempt in Eq. (2.1) to instead write

$$\Psi(s_1, s_2) = \frac{1}{\sqrt{2}} \left[\psi(s_1)\varphi(s_2) \pm \psi(s_2)\varphi(s_1)\right] . \tag{2.4}$$

Pairs of identical particles with joint wavefunctions satisfying the antisymmetric form of Eq. (2.4) are known as fermions, while those with symmetric joint wavefunctions are known as bosons.

One profound consequence of the wavefunction symmetry is that the state vectors s_1 and s_2 can never be equal for a pair of identical fermions; for this to be the case, their joint wavefunction would be identically zero. This is the famous Pauli exclusion principle: the maximum occupancy of a single-particle state in an ensemble of identical fermions is one. Pauli exclusion has far-reaching consequences, from quantum descriptions of modern chemistry, which are closely linked to the energy levels of electrons (spin-$\frac{1}{2}$ fermions), through to the degeneracy pressure that prevents neutron stars from collapsing to form black holes.

Identical bosons, on the other hand, are not subject to such restrictions; they *are* able to coexist in the same quantum state simultaneously. This is particularly relevant for the lowest-lying or ground state, which, under appropriate conditions, can become macroscopically occupied as a Bose–Einstein condensate emerges.

Determining the bosonic or fermionic nature of a particle requires knowledge of its intrinsic angular momentum, or spin. The spin-statistics theorem [24] connects the symmetry properties of a particle to its spin[1]. Particles with a spin that is an integer multiple of the reduced Planck constant $\hbar$ are bosons, whereas those with half-integer spin are fermions, and include protons, neutrons, and electrons. The total spin of a composite particle is determined by adding the spins of its constituent particles. Neutral atoms have equal numbers of protons and electrons, each of which contributes a half-integer multiple of $\hbar$ to the total spin, and so their combined sum is an integer multiple of $\hbar$. The fermionic or bosonic nature of neutral atoms is therefore determined solely by the number of neutrons in the nucleus, with different mass isotopes described by different statistics. Neutral atoms with an odd number of neutrons are fermionic, whereas those with an even number of neutrons are bosonic. The experimental platform used in this work uses gases of ^{39}K, which is a bosonic isotope of potassium.

[1] The connection between spin and (anti-)symmetry requires a relativistic treatment; it arises from requiring invariance of the wave equations under Lorentz transformations.

2.2 Quantum statistics

The statistics of classical gases in equilibrium can be modelled by assigning probabilities to the different sets of microscopic parameters. These probabilities are proportional to the Boltzmann factor, i.e., $\propto \exp\left(-\varepsilon/(k_{\mathrm{B}}T)\right)$, where ε is the energy corresponding to the configuration, k_{B} is the Boltzmann constant, and T is the system temperature. Whilst this familiar description works well at the temperatures of $\approx$300 K with which we are most familiar from everyday experience, it breaks down once the typical spacing between energy levels is comparable to the temperature. At these lower energy scales, the quantum statistics become relevant, and the distinction between bosons and fermions becomes very important.

Here we consider the effects of distinguishability upon the distribution functions of particles in equilibrium at low temperatures. Following [25], for example, let us first consider any single-particle state of a system, e.g., one particular eigenstate of a particle in a box. Let the corresponding energy of the state, when occupied by a single particle, be ε. We are interested in finding the average occupancy of the state, given a chemical potential μ and temperature T. When the state is unoccupied, its energy is simply zero. When occupied by N particles, and neglecting the effects of interactions between atoms, it is instead $N\varepsilon$. The probability of the state being occupied by N particles, $P(N)$, is then given by

$$P(N) = \frac{1}{\mathcal{Z}} \exp\left(-\frac{N(\varepsilon-\mu)}{k_{\mathrm{B}}T}\right) \tag{2.5}$$

$$\mathcal{Z} = \sum_N \exp\left(-\frac{N(\varepsilon-\mu)}{k_{\mathrm{B}}T}\right), \tag{2.6}$$

where $\mathcal{Z}$ is the grand partition function, and the sum is to be taken over all permissible values of N.

For fermions, N can only be zero or one, and so the Fermi probability $P_{\mathrm{F}}(N)$ is

$$P_{\mathrm{F}}(N) = \frac{\exp[-N(\varepsilon-\mu)/(k_{\mathrm{B}}T)]}{1+\exp[-(\varepsilon-\mu)/(k_{\mathrm{B}}T)]}, \tag{2.7}$$

whereas for bosons, where N is not restricted as for fermions, the Bose probability $P_{\mathrm{B}}(N)$ is instead

$$\begin{aligned} P_{\mathrm{B}}(N) &= \frac{\exp[-N(\varepsilon-\mu)/(k_{\mathrm{B}}T)]}{1+\exp[-(\varepsilon-\mu)/(k_{\mathrm{B}}T)]+\exp[-2(\varepsilon-\mu)/(k_{\mathrm{B}}T)]+\ldots} \\ &= \exp[-N(\varepsilon-\mu)/(k_{\mathrm{B}}T)](1-\exp[-(\varepsilon-\mu)/(k_{\mathrm{B}}T)]). \end{aligned} \tag{2.8}$$

In order for the sum to converge, we must have $\mu < \varepsilon$. This must apply to all states, and so for the bosonic case, μ must be less than the zero-point energy $\varepsilon_{\mathrm{min}}$ of the ground state.

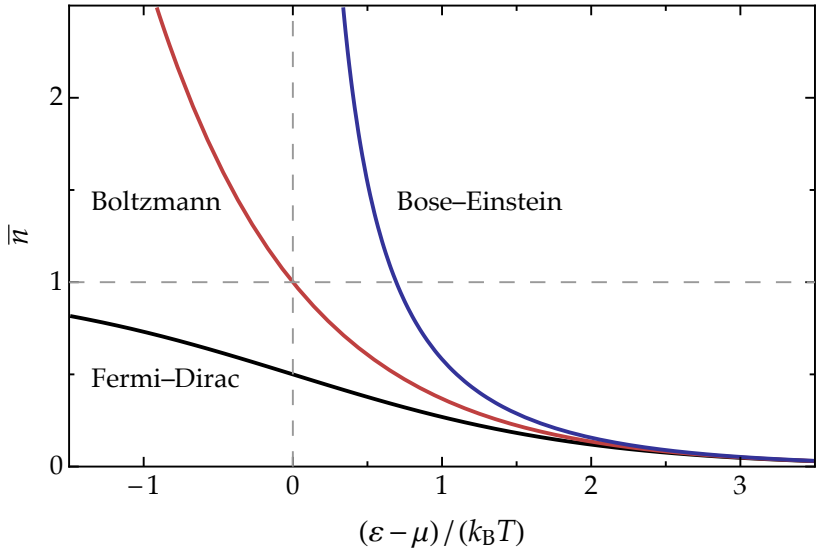

Figure 2.1 | **Comparison of statistical distributions.** Indistinguishability dramatically influences the particle statistics. The Fermi–Dirac distribution (black) always takes values between 0 and 1, while the Bose–Einstein distribution (blue) diverges for $\mu \to \varepsilon^-$. Both are asymptotically equivalent to the classical Boltzmann distribution (red) in the limit $\varepsilon - \mu \gg k_\mathrm{B}T$.

The distribution functions are then the average occupancies, which are

$$\begin{aligned} \bar{N}_\mathrm{F} &= \sum_{N=0}^{1} N P_\mathrm{F}(N) \\ &= \frac{1}{\exp[(\varepsilon-\mu)/(k_\mathrm{B}T)]+1}, \quad \text{and} \end{aligned} \tag{2.9}$$

$$\begin{aligned} \bar{N}_\mathrm{B} &= \sum_{N=0}^{\infty} N P_\mathrm{B}(N) \\ &= \frac{1}{\exp[(\varepsilon-\mu)/(k_\mathrm{B}T)]-1}. \end{aligned} \tag{2.10}$$

These are known as the Fermi(–Dirac) and Bose(–Einstein) distributions respectively. The key difference between the two results is the sign in the denominator.

The distributions are plotted together in Fig. 2.1. In the limit that $\varepsilon - \mu \gg k_\mathrm{B}T$, both the Fermi and Bose distributions are asymptotically equivalent. In fact, this corresponds to the classical or Boltzmann limit familiar from any undergraduate course in statistical mechanics, which is also plotted in Fig. 2.1 for comparison. In this limit, the number of accessible single-particle states far exceeds the number of particles that need to be distributed amongst them, such that the average occupancies are low for all states.

When $\varepsilon - \mu \lesssim k_\mathrm{B}T$, however, the differences between the distributions are dramatic. The Fermi–Dirac distribution takes on values within the interval $[0, 1]$ for all values of ε; low-energy states ($\varepsilon \ll \mu$) are at most singly occupied. For bosons, however, as $\mu \to \varepsilon_\mathrm{min}^-$, the occupancy of the ground state diverges. Physically, μ cannot increase further, as this would cause the distribution function to become negative. This critical value of μ is the threshold for the onset

of Bose–Einstein condensation.

2.3 The ideal Bose gas

From now on, we shall restrict our focus to the bosonic case. In this section we present standard results that link the measurable properties of Bose systems in equilibrium to one another, namely the atomic density, momentum distribution, temperature, and chemical potential. At fixed (T, μ), the total number of atoms in all states is given by the sum of Eq. (2.10) over all available states s, i.e.,

$$N_{\mathrm{tot}} = \sum_s \bar{N}_{\mathrm{B}} \,. \tag{2.11}$$

The sum in Eq. (2.11) is generally cumbersome to evaluate directly. In most physical applications, energy levels are densely spaced relative to the thermal energy scale $k_{\mathrm{B}}T$, and the sum is well-approximated by the integral

$$N_{\mathrm{tot}} \approx N_0 + \int_0^\infty \mathrm{d}\varepsilon \, D(\varepsilon) \, \bar{N}_{\mathrm{B}}(\varepsilon) \equiv N_0 + N_{\mathrm{th}} \,, \tag{2.12}$$

where the density of states, $D(\varepsilon)$, counts the number of states with energy in the interval $[\varepsilon, \varepsilon + \mathrm{d}\varepsilon]$. We have also split the contributions to Eq. (2.11) into two, 'peeling off' the number of atoms N_0 in the lowest-lying state from the thermal contribution N_{th}, and implicitly taken $\varepsilon_{\mathrm{min}} \approx 0$. This final assumption is valid provided N_{tot} is sufficiently large; this condition is satisfied throughout this thesis.

For free particles of mass m in three dimensions, the density of states is (see, e.g., [22])

$$D(\varepsilon) = \frac{V m^{3/2}}{\sqrt{2}\pi^2\hbar^3} \varepsilon^{1/2} \,, \tag{2.13}$$

where V is the system volume. We can then directly evaluate the density of atoms in excited states N_{th} for a given (T, μ) as

$$\frac{N_{\mathrm{th}}}{V} = \lambda_T^{-3} \, g_{3/2}(\exp[\mu/(k_{\mathrm{B}}T)]) \,, \tag{2.14}$$

where $\lambda_T = (2\pi\hbar^2/[m k_{\mathrm{B}} T])^{1/2}$ is the thermal wavelength, and g_ℓ denotes the polylogarithm of order ℓ,

$$g_\ell(z) = \sum_{j=1}^{\infty} \frac{z^j}{j^\ell} \,. \tag{2.15}$$

In the critical case $\mu \to 0$, we find that the phase-space density of non-interacting[2] thermal atoms saturates at the value $\max\{N_{\mathrm{th}}\lambda_T^3/V\} = \zeta(3/2) \approx 2.612$, where ζ denotes the Riemann

[2] We shall return to the *interacting* case in section 4.2.1.

function. The excited states cannot accommodate any additional atoms; the atoms must instead macroscopically occupy the ground state to form a Bose–Einstein condensate[3]. We first continue to explore the properties of atoms in thermally occupied states, and return to the properties of the condensate later in this chapter.

2.3.1 Thermal density and momentum distributions

One can readily determine the density and momentum distribution of the thermal bosons in a more general confining potential $U(\mathbf{r})$. Recasting Eq. (2.10) as a function over the joint phase space of position $\mathbf{r}$ and momentum $\hbar\mathbf{k}$, we can write

$$f_{\mathrm{B}}(\mathbf{r},\mathbf{k}) = \left(\exp\left[\frac{\varepsilon(\mathbf{r},\mathbf{k})-\mu}{k_{\mathrm{B}}T}\right]-1\right)^{-1}, \tag{2.16}$$

where a particle's energy is written *classically* as

$$\varepsilon(\mathbf{r},\mathbf{k}) = \frac{\hbar^2|\mathbf{k}|^2}{2m} + U(\mathbf{r}), \tag{2.17}$$

the sum of independent kinetic and potential energy terms. This is known as the *semi-classical* approximation, which is valid when the length scale of variations in the trapping potential is much larger than λ_T, i.e., locally the gas behaves as if it were a bulk gas. This approximation captures the density and momentum distribution of particles in the thermal cloud (both in the presence or absence of a condensate), whereas particles in the condensate itself generally require a separate treatment [see section 2.6].

We take the density of quantum states in phase space to be $(2\pi\hbar)^{-3}$, such that the total number of particles in thermally occupied states is given by

$$N_{\mathrm{th}} = \frac{1}{(2\pi)^3}\int \mathrm{d}^3\mathbf{r}\int \mathrm{d}^3\mathbf{k}\, f_{\mathrm{B}}(\mathbf{r},\mathbf{k}). \tag{2.18}$$

The thermal densities in coordinate and momentum space are each given by omitting one of the two integrals, i.e.,

$$n(\mathbf{r}) = \lambda_T^{-3} g_{3/2}(\exp[-(U(\mathbf{r})-\mu)/(k_{\mathrm{B}}T)]), \quad \text{and} \tag{2.19}$$

$$n_k(\mathbf{k}) = \frac{1}{(2\pi)^3}\int \mathrm{d}^3\mathbf{r}\left(\exp\left[\frac{\hbar^2|\mathbf{k}|^2/(2m)-\mu}{k_{\mathrm{B}}T}\right]\exp\left[\frac{U(\mathbf{r})}{k_{\mathrm{B}}T}\right]-1\right)^{-1}. \tag{2.20}$$

We shall use the subscript k throughout this thesis to differentiate between the coordinate- and momentum-space densities. We will most often concern ourselves with the momentum distribution of our atoms, and so Eq. (2.20) is of most relevance for our applications. The following two special cases will be of particular interest:

[3] The densities of states for one- and two-dimensional infinite uniform systems are $D_{1\mathrm{D}}(\varepsilon) \propto \varepsilon^{-1/2}$ and $D_{2\mathrm{D}}(\varepsilon) \propto \varepsilon^{0}$ respectively. Neither of these $D(\varepsilon)$ saturates the integral in Eq. (2.12), and so condensation is precluded in these cases.

(i) *The homogeneous trap*

In the ideal case, $U(\mathbf{r})$ is zero within the trapping volume V, and infinite elsewhere. Eq. (2.20) then becomes

$$n_k(\mathbf{k}) = \frac{V}{(2\pi)^3}\left[\exp\left(\frac{\hbar^2|\mathbf{k}|^2/(2m)-\mu}{k_\mathrm{B}T}\right)-1\right]^{-1}. \tag{2.21}$$

(ii) *The harmonic trap*

This potential is parameterised by the three trapping frequencies $(\omega_x, \omega_y, \omega_z)$, with each corresponding to one of the Cartesian axes. The potential is then written as $U(\mathbf{r}) = \frac{1}{2}m(\omega_x^2x^2+\omega_y^2y^2+\omega_z^2z^2)$, which when inserted into Eq. (2.20) yields

$$n_k(\mathbf{k}) = \left(\frac{\hbar}{m\lambda_T}\right)^3\cdot\frac{1}{\omega_x\omega_y\omega_z}\cdot g_{3/2}\left[\exp\left(-\frac{\hbar^2|\mathbf{k}|^2/(2m)-\mu}{k_\mathrm{B}T}\right)\right]. \tag{2.22}$$

2.4 Scattering theory

In the discussion so far, we have completely neglected the effect of interactions between the atoms. This is a significant problem indeed – without interactions, the atoms would never be able to reach thermal equilibrium in the first place. Modelling interactions between atoms amounts to describing the scattering events that occur when two atoms collide with one another. Scattering theory is quite a wide area of study, addressed in the context of ultracold atoms in [26], and more comprehensively in [27]. Here we closely follow the arguments presented in [4,22]. In this section, we consider only elastic scattering, neglecting the possibility for atoms to change their internal states or form bound pairs in a collision; a conceptual extension to a two-channel model follows in the next section.

We consider two atoms, each of mass m, interacting under the influence of a short-range isotropic scattering potential $U_\mathrm{int}(r)$, where r is the separation between the atoms. At large r, we assume that $U_\mathrm{int}(r) \to 0$ and that the atoms have a relative momentum of magnitude $\hbar k$. We separate the motion into the plane-wave centre-of-mass contribution, and a contribution for the relative motion. The scattering is captured by writing the wavefunction of the relative motion as the sum of an incoming planar wave along the z axis, and an outgoing spherical wave. Asymptotically, we have

$$\psi_\mathrm{rel} \underset{r\to\infty}{\approx} \exp(ikz) + f(k,\theta)\frac{\exp(ikr)}{r}, \tag{2.23}$$

where the scattering amplitude $f(k,\theta)$ depends on magnitude k of the relative momentum, and the angle θ that describes the direction of the scattered wave relative to the incoming one. It is convenient to expand ψ_rel in the basis of Legendre polynomials[4] P_ℓ, with angular momentum

[4] The Legendre polynomials can be generated, e.g., using Rodrigues' formula, $P_\ell(x) = \frac{1}{2^\ell \ell!}\frac{\mathrm{d}^\ell}{\mathrm{d}x^\ell}(x^2-1)^\ell$.

ℓ, and the corresponding radial functions $\varphi_{k\ell}(r)/r$ as

$$\psi_{\text{rel}} = \sum_{\ell=0}^{\infty} c_\ell P_\ell(\cos\theta)\frac{\varphi_{k\ell}(r)}{r}\,. \tag{2.24}$$

The radial wavefunctions satisfy

$$\left[-\frac{\hbar^2}{2m_r}\frac{\mathrm{d}^2}{\mathrm{d}r^2} + U_{\text{int}}(r) + \frac{\hbar^2\ell(\ell+1)}{2m_r r^2}\right]\varphi_{k\ell}(r) = \frac{\hbar^2 k^2}{2m_r}\varphi_{k\ell}(r)\,, \tag{2.25}$$

with the reduced mass $m_r = m^2/(m+m) = \frac{1}{2}m$. The coefficients c_ℓ can be determined by demanding consistency between the asymptotic and Legendre-expanded forms. The asymptotic solutions for $r \to \infty$ are given by

$$\varphi_{k\ell}(r) \simeq \frac{\sin(kr - \ell\pi/2 + \delta_\ell)}{k}\,. \tag{2.26}$$

in which all details of the scattering potential enter only via the phase shifts δ_ℓ. Combining Eqs. (2.23), (2.24), and (2.26) yields the partial-wave expansion of the scattering amplitude,

$$f(k,\theta) = \frac{1}{2ik}\sum_{\ell=0}^{\infty}(2\ell+1)[\exp(i2\delta_\ell) - 1]P_\ell(\cos\theta)\,. \tag{2.27}$$

In the low-energy limit, the phase shifts for $\ell \neq 0$ are negligible [28], and the scattering amplitude is dominated by the $\ell = 0$ (s-wave) contribution. In this limit, the phase shift δ_0 satisfies

$$\tan\delta_0 = -ka\,, \tag{2.28}$$

where the corresponding scattering length a depends on the properties of $U_{\text{int}}(r)$, and we have,

$$f(k) = \frac{\exp(i2\delta_0) - 1}{2ik} = -\frac{a}{1+ika}\,, \tag{2.29}$$

which is now independent of the scattering angle θ. The scattering cross section σ is in general given by integrating $|f(k)|^2$ over the solid angle. Naïvely we would expect a result of $4\pi a^2/(1+a^2k^2)$, however this neglects the effects of indistinguishability. When two identical particles scatter off one another, the following two outcomes are equivalent: (i) a particle scatters through angle θ, and (ii) the other particle scatters through angle $\pi - \theta$. This leads to a doubling of the s-wave amplitude, $f(k) \to 2f(k)$. The solid angle over which we must integrate is also reduced by a factor of two, from $4\pi \to 2\pi$, to avoid any double counting. The s-wave scattering cross section for two indistinguishable particles is therefore

$$\sigma = \frac{8\pi a^2}{1+a^2k^2}\,. \tag{2.30}$$

Under typical experimental conditions, the denominator can usually be neglected, i.e., the scattering cross section is essentially independent of k, and is determined solely by the scattering length.

The value of the scattering length itself can be determined using the Born approximation. To first order, the scattering length is then[5]

$$a = \frac{m_r}{2\pi\hbar^2}\int \mathrm{d}^3\mathbf{r}\, U_{\mathrm{int}}(r) = \frac{m}{4\pi\hbar^2}\int \mathrm{d}^3\mathbf{r}\, U_{\mathrm{int}}(r)\,, \tag{2.31}$$

such that the whole interaction potential is parameterised by just a single length; the short-range details of $U_{\mathrm{int}}(r)$ are not probed during the scattering event, and only their integral is relevant. In fact, *any* potential giving the same a in Eq. (2.31) is equivalent for our purposes, and so for convenience we usually think of the interaction potential in its contact form,

$$U_{\mathrm{eff}}(\mathbf{r},\mathbf{r}') = \frac{4\pi\hbar^2 a}{m}\delta^{(3)}(\mathbf{r}-\mathbf{r}')\,, \tag{2.32}$$

where here $\delta^{(3)}$ denotes the Dirac delta function. Since this coefficient of the delta function reappears very frequently, it is convenient to define the quantity

$$g \equiv \frac{4\pi\hbar^2 a}{m}\,. \tag{2.33}$$

2.5 Feshbach resonances

One particularly attractive feature of ultracold atom experiments is the ability to readily tune the strength of interatomic interactions, i.e., to vary a. This is achieved through the use of Feshbach resonances, which allow for control over the scattering properties of several commonly used atomic species by applying an external magnetic field. Here we outline the basic operating principle as it relates to our experimental platform. For a more detailed treatment, we refer the reader to [4, 29].

When considering scattering events in the previous section, we considered only one possible collision channel. In reality, however, there may be several such channels available, corresponding, e.g., to different internal states of the colliding atoms. The basic two-channel model is depicted in Fig. 2.2. Here, we have one energetically open entrance channel and one closed channel that admits a bound state: the open channel plays the role of our scattering potential in the previous section, while the bound state of the closed channel can affect the phase shift of the scattered wavefunction. The two energies that predominantly influence the phase shift are the asymptotic ($r \to \infty$) energy of the open channel and the energy of the closed-channel bound state. These energies can be varied by means of an external magnetic field[6] and in general, the magnetic moments of the corresponding internal states are not the same, such that for a fixed change in the magnetic field, the energies of each of the two states change by different

[5] Convergence requires that $U_{\mathrm{int}}(r)$ fall off faster than $\frac{1}{r^{3+\epsilon}}$ for $\epsilon > 0$ as $r \to \infty$. In practice, the van der Waal's interaction is asymptotically $\propto \frac{1}{r^6}$.

[6] The energy levels can also be shifted by other means, e.g., using optical potentials [31].

amounts. For an appropriate choice of field, therefore, the two energies can be brought into resonance.

Near such a resonance, the scattering length can be shown (e.g., in [32]) to obey

$$a(B) = a_{\mathrm{bg}}\left(1 - \frac{\Delta}{B - B_\infty}\right), \tag{2.34}$$

where a_{bg} denotes the background scattering length for fields far from the resonance, B_∞ is the resonance position at which the bound-state and open-channel energies are equal, and Δ is the resonance width. The resonances relevant for our experiments are discussed in more detail in section 3.3.1. Feshbach resonances provide the experimentalist with an invaluable control knob; experiments can be performed in the non-interacting limit $a \to 0$, the unitary regime where $|a| \to \infty$ (see chapter 6), and at all intermediate interaction strengths, whether repulsive or attractive. Indeed, the scattering length can even be varied during the course of an experiment to suit the experimentalist's needs.

The mixing of the open and closed channels near a Feshbach resonance also admits dressed molecular states. The simplest of these states is a weakly bound two-body state on the positive-a side of the resonance, with binding energy $E_{2\mathrm{B}} = -\hbar^2/(ma^2)$. As the magnetic field is adjusted further away from the resonance, additional lengthscales beyond a enter this expression for the

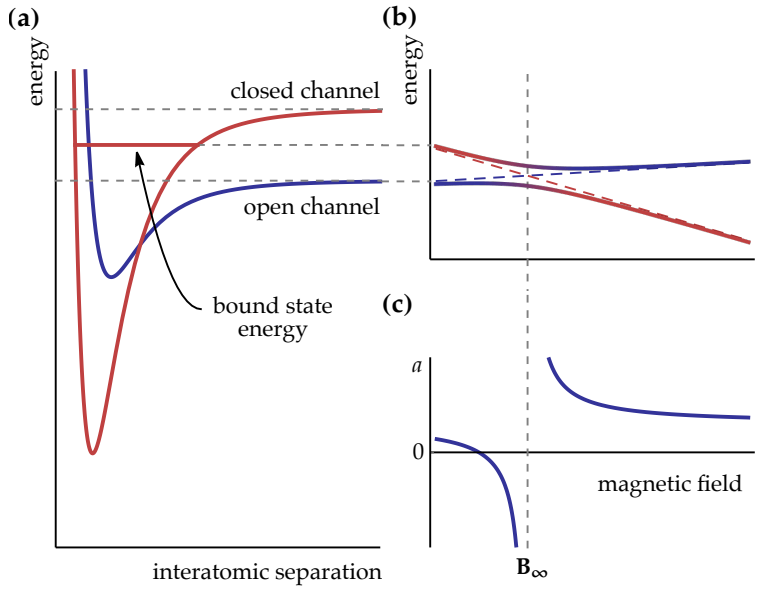

Figure 2.2 | **Two-channel model of a Feshbach resonance.** **(a)** Interaction potential as a function of interatomic separation. A pair of atoms enter along the open-channel (blue) asymptote, acquiring an additional phase shift from the influence of a closed-channel (red) bound state. **(b)** The bound-state and asymptotic open-channel energies vary as a function of the applied magnetic field. Their different gradients reflect the different magnetic moments of the corresponding internal states. **(c)** As the two energies are brought into resonance, the open and closed channels mix significantly, resulting in a pole in the scattering length a. Figure adapted from [30].

binding energy. The so-called 'mean scattering length' $\bar{a}$ is the dominant contribution[7] [4, 33], giving rise to a leading-order refinement to the binding energy,

$$E_{2B} \approx -\frac{\hbar^2}{m(a-\bar{a})^2}\,. \tag{2.35}$$

Further information, including numerical values for several atomic species, can be found in [4].

In general, bound states near a Feshbash resonance may comprise more than two atoms. We will return to this topic in more detail in chapter 6, considering in particular three-body Efimov states [34, 35].

2.6 Condensate wavefunction

In section 2.3.1, we considered the coordinate- and momentum-space distributions of atoms in thermally excited states using the semi-classical approximation. Here we turn to the corresponding properties of atoms in the Bose–Einstein condensate.

We adopt a mean-field approach, and assume that the wave function is a symmetrised product of single-particle wavefunctions. Moreover, when fully condensed, all bosons occupy the same single-particle state, and the joint wavefunction for N_0 condensed particles is therefore given by

$$\Psi(\mathbf{r}_1,\, \mathbf{r}_2,\, \ldots,\, \mathbf{r}_{N_0}) = \prod_{i=1}^{N_0} \varphi(\mathbf{r}_i)\,, \tag{2.36}$$

where the single-particle state φ is normalised to unity. The effective Hamiltonian has contributions from the kinetic energy, external potential, and interatomic interactions, taking the form

$$\hat{H} = \sum_{i=1}^{N_0} \left[\frac{\mathbf{p}_i^2}{2m} + U(\mathbf{r}_i)\right] + g\sum_{i<j}\delta^{(3)}(\mathbf{r}_i - \mathbf{r}_j)\,, \tag{2.37}$$

with g as in Eq. (2.33). The total energy E is then just the expectation value of $\hat{H}$ in our symmetrised state, and is therefore

$$E = N_0 \int \mathrm{d}^3\mathbf{r}\, \left[-\varphi^*(\mathbf{r})\frac{\hbar^2}{2m}\nabla^2\varphi(\mathbf{r}) + U(\mathbf{r})|\varphi(\mathbf{r})|^2 + \frac{(N_0-1)}{2}g|\varphi(\mathbf{r})|^4\right]. \tag{2.38}$$

For $N_0 \gg 1$, it is convenient to renormalise, writing the condensate wavefunction $\psi = \sqrt{N_0}\varphi$, such that the energy is

$$E \approx \int \mathrm{d}^3\mathbf{r}\, \left[-\psi^*(\mathbf{r})\frac{\hbar^2}{2m}\nabla^2\psi(\mathbf{r}) + U(\mathbf{r})|\psi(\mathbf{r})|^2 + \frac{1}{2}g|\psi(\mathbf{r})|^4\right], \tag{2.39}$$

the density $n(\mathbf{r}) = |\psi(\mathbf{r})|^2$, and $N_0 = \int \mathrm{d}^3\mathbf{r}\,|\psi(\mathbf{r})|^2$. Here we have neglected terms $\mathcal{O}(1/N_0)$.

[7] The length $\bar{a}$ is closely related to the more common van der Waals length: $\bar{a}/R_{\mathrm{vdW}} = 4\pi/\Gamma(\frac{1}{4})^2 \approx 0.956$.

The ground-state wavefunction is then found by minimising the energy subject to a fixed value of N_0. This is equivalent to solving $\delta E - \mu \delta N_0 = 0$, where we have introduced the chemical potential μ that plays the role of a Lagrange multiplier in this problem. As the wavefunction is complex, this must hold true for variations both with respect to ψ and its complex conjugate ψ^*. Setting the variation in $E - \mu N_0$ with respect to ψ^* to zero yields

$$-\frac{\hbar^2}{2m}\nabla^2\psi(\mathbf{r}) + U(\mathbf{r})\psi(\mathbf{r}) + g|\psi(\mathbf{r})|^2\psi(\mathbf{r}) = \mu\psi(\mathbf{r})\,, \tag{2.40}$$

which is known as the (time-independent) Gross–Pitaevskii equation (GPE). It takes the form of the familiar Schrödinger equation, but with two distinct differences: there is an additional density-dependent interaction energy, and the eigenvalue is the chemical potential, rather than the average energy per particle.

Armed with the GPE, we are now able to determine the ground state for arbitrary $U(\mathbf{r})$. The density and momentum distributions of the condensed atoms are then given by

$$n(\mathbf{r}) = |\psi(\mathbf{r})|^2\,, \tag{2.41}$$

$$n_k(\mathbf{k}) = \left|\frac{1}{\sqrt{2\pi}}\int \mathrm{d}^3\mathbf{r}\, \exp\left(-i\mathbf{k}\cdot\mathbf{r}\right)\psi(\mathbf{r})\right|^2\,. \tag{2.42}$$

2.6.1 Thomas–Fermi approximation

The solutions to Eq. (2.40) are in general not easy to evaluate. Indeed, the introduction of a non-linear term precludes analytic solutions for most potentials. Under many experimental circumstances, however, the kinetic term may be safely neglected; this is known as the Thomas–Fermi approximation[8]. In particular, this applies when considering clouds of sufficiently large spatial extent with repulsive interactions ($a > 0$). The Thomas–Fermi approximation yields a derivative-free equation for the ground-state wavefunction,

$$U(\mathbf{r}) + g|\psi(\mathbf{r})|^2 = \mu\,, \tag{2.43}$$

which is readily solvable to obtain the Thomas–Fermi density

$$n_{\mathrm{TF}}(\mathbf{r}) = \begin{cases} \dfrac{\mu - U(\mathbf{r})}{g}, & U(\mathbf{r}) < \mu \\ 0, & \text{elsewhere}\,. \end{cases} \tag{2.44}$$

In this context, μ determines both the total number of particles, and the extent to which the condensate 'fills its container'.

In the specific case of a uniform potential, with hard-wall boundaries, the atomic density within the bulk of the trap is also uniform. At the trap walls, however, we must impose a boundary condition on the density: atoms cannot have infinite energy, and so the condensate

[8] In cases where the kinetic energy can *not* be neglected, a computational approach (e.g. appendix A) is needed.

wavefunction cannot extend into the wall. On the boundary, the density must be identically zero. This gives rise to a surface region inside the trap walls within which the density must 'heal' from zero to the bulk value. The size of this region is characterised by the *healing length* ξ. Its value is given by setting the kinetic and interaction-energy terms of the GPE to be equal, i.e.,

$$\begin{aligned} \frac{\hbar^2}{2m\xi^2} &= \frac{4\pi\hbar^2 a}{m}|\psi|^2 \\ \xi &= \frac{1}{\sqrt{8\pi n a}}\,. \end{aligned} \tag{2.45}$$

2.7 Overlap of the gas components

A particularly useful quality of the saturated interacting homogeneous Bose gas is that both the thermal and condensed components have a uniform density, and are completely spatially overlapped (neglecting ξ). From sections 2.3.1 and 2.6.1, the thermal and condensate densities within the trapping volume are

$$n_{\rm th}(\mathbf{r}) = \lambda_T^{-3}\zeta(\tfrac{3}{2})\,, \quad \text{and} \tag{2.46}$$

$$n_{\rm TF}(\mathbf{r}) = \mu/g\,; \tag{2.47}$$

neither explicitly depends on $\mathbf{r}$. This offers an advantage when considering density-dependent processes: in this homogeneous case, one can simply replace the densities $n_{\rm th} \to N_{\rm th}/V$ and $n_0 \to N_0/V$. Here the global, trap-averaged properties are identical to the local ones.

For contrast, in a general trapping potential $U(\mathbf{r})$, the densities of the two components are functions of the position within the trap, and the two components will have different spatial extents. Let us take as an example a saturated non-interacting Bose gas in a harmonic trap, and for convenience we shall take the potential to be isotropic, i.e., $U(\mathbf{r}) = \frac{1}{2}m\omega^2|\mathbf{r}|^2$, where ω is the trap frequency. Here the condensed component of the gas has the density distribution

$$n_0(\mathbf{r}) = N_0\left(\frac{m\omega}{\pi\hbar}\right)^{3/2}\exp(-m\omega|\mathbf{r}|^2/\hbar)\,, \tag{2.48}$$

corresponding to the oscillator's ground state, and from Eq. (2.19) the thermal atoms have

$$n_{\rm th}(\mathbf{r}) = \lambda_T^{-3} g_{3/2}(\exp[-\tfrac{1}{2}m\omega^2|\mathbf{r}|^2/(k_{\rm B}T)])\,. \tag{2.49}$$

In each case, we can determine the mean squared extent according to

$$\langle r^2\rangle = \frac{\int d^3\mathbf{r}\, r^2\, n(\mathbf{r})}{\int d^3\mathbf{r}\, n(\mathbf{r})}\,, \tag{2.50}$$

and we find $\langle r^2\rangle_0 = 3\hbar/(2m\omega)$ and $\langle r^2\rangle_{\rm th} = 3[\zeta(4)/\zeta(3)]k_{\rm B}T/(m\omega^2)$. The relative size of the two components *in situ* is therefore a function of the ratio $k_{\rm B}T/(\hbar\omega)$.

When interatomic interactions are introduced to the problem, the picture becomes more complex. The condensate, centred at the minimum of the harmonic potential, creates an additional mean-field potential that repels the thermal atoms. As a consequence, the thermal atoms are expelled from the trap centre, and they instead occupy the volume surrounding the condensate. This corresponds to a modification of the density of states at a global level that further reduces the overlap between the condensed and thermal components.

Finally, not only do the two components of the gas have different sizes in non-uniform potentials, but their densities vary throughout the trap, and in general have different functional dependencies on the position. It is therefore necessary to resolve density-dependent processes as a function of position. The global nature of the densities for gases in *uniform* potentials therefore represents a significant simplification for studying such processes.

2.8 Bogoliubov equations

In order to study excitations in a Bose-condensed gas, one needs to know not only what the ground state is, but also how the system responds to small perturbations about the ground state. Analogously to the Schrödinger equation, a generalisation of Eq. (2.40) describes the evolution of the wavefunction[9]:

$$i\hbar\frac{\partial}{\partial t}\psi_t(\mathbf{r}) = -\frac{\hbar^2}{2m}\nabla^2\psi_t(\mathbf{r}) + U(\mathbf{r})\psi_t(\mathbf{r}) + g\left|\psi_t(\mathbf{r})\right|^2\psi_t(\mathbf{r})\,. \tag{2.51}$$

The time-dependent form of the ground-state wavefunction is $\psi_t^0(\mathbf{r}) = \psi(\mathbf{r})\exp(-i[\mu/\hbar]t)$, i.e., the product of $\psi(\mathbf{r})$ from the previous section with a time-dependent global phase that rotates at the rate $\mu/\hbar$.

To determine the nature of the excitations described by Eq. (2.51), we linearise the equation by writing ψ_t as the sum of ψ_t^0 and a small fluctuation term $\delta\psi$. We assume that the majority of atoms remain in the condensate, such that the density $|\psi_t^0|^2$ is left unchanged. In general, $\delta\psi$ is linearly independent from its complex conjugate, and so we must consider both. Retaining only linear terms in $\delta\psi$ and $\delta\psi^*$, one finds

$$i\hbar\frac{\partial}{\partial t}\delta\psi = -\frac{\hbar^2}{2m}\nabla^2\delta\psi + U(\mathbf{r})\delta\psi \;\; + g\left[2|\psi_t^0|^2\delta\psi + (\psi_t^0)^2\delta\psi^*\right]\,, \quad \text{and} \tag{2.52a}$$

$$-i\hbar\frac{\partial}{\partial t}\delta\psi^* = -\frac{\hbar^2}{2m}\nabla^2\delta\psi^* + U(\mathbf{r})\delta\psi^* + g\left[2|\psi_t^0|^2\delta\psi^* + (\psi_t^{0*})^2\delta\psi\right]\,. \tag{2.52b}$$

We have suppressed the arguments of the wavefunctions for brevity. We seek solutions $\delta\psi$ with well-defined energies, $\hbar\omega$, and so we separate the time dependence explicitly in the ansatz

$$\delta\psi(\mathbf{r}) = \exp\left(-i[\mu/\hbar]t\right)\left[u(\mathbf{r})\exp\left(-i\omega t\right) - v^*(\mathbf{r})\exp\left(i\omega t\right)\right]\,, \tag{2.53}$$

[9] This result is obtainable formally by using, e.g., an action-minimisation approach.

with the two time-independent functions u and v yet to be determined. Inserting the ansatz into Eq. (2.52), we find the Bogliubov equations

$$\left[-\frac{\hbar^2}{2m}\nabla^2 + U(\mathbf{r}) + 2gn(\mathbf{r}) - \mu - \hbar\omega\right] u(\mathbf{r}) = gn(\mathbf{r})v(\mathbf{r}) \tag{2.54a}$$

$$\left[-\frac{\hbar^2}{2m}\nabla^2 + U(\mathbf{r}) + 2gn(\mathbf{r}) - \mu + \hbar\omega\right] v(\mathbf{r}) = gn(\mathbf{r})u(\mathbf{r})\,, \tag{2.54b}$$

where we have, without loss of generality, taken $\psi(\mathbf{r})$ to be real.

Applying these results to a homogeneous gas gives insight into the nature of excitations present in the experimental system used for the work in this thesis. In a uniform system of volume V, translational invariance[10] requires u and v to take the form of plane waves, i.e.,

$$u(\mathbf{r}) = u_k \frac{\exp(i\mathbf{k}\cdot\mathbf{r})}{V^{1/2}} \tag{2.55a}$$

$$v(\mathbf{r}) = v_k \frac{\exp(i\mathbf{k}\cdot\mathbf{r})}{V^{1/2}}\,, \tag{2.55b}$$

and the chemical potential is simply $\mu = gn$. The Bogoliubov equations then become

$$\begin{pmatrix} \frac{\hbar^2k^2}{2m} + \mu - \hbar\omega & -\mu \\ -\mu & \frac{\hbar^2k^2}{2m} + \mu + \hbar\omega \end{pmatrix} \begin{pmatrix} u_k \\ v_k \end{pmatrix} = \mathbf{0}\,, \tag{2.56}$$

which has non-trivial solutions only when the matrix cannot be inverted. This requires that the excitation energies obey the dispersion relation

$$\hbar\omega = \sqrt{\frac{\hbar^2k^2}{2m}\left(\frac{\hbar^2k^2}{2m} + 2\mu\right)}\,. \tag{2.57}$$

For $\hbar^2k^2/(2m) \ll \mu$, the low-k excitations approximately satisfy $\omega \simeq \sqrt{\mu/m}\,k$, and correspond to acoustic modes with sound speed $\sqrt{\mu/m}$. In contrast to this, for large k, $\hbar\omega \simeq \hbar^2k^2/(2m) + \mu$; these excitations correspond to free particles with a mean-field shift to their energies of μ. The healing length $\xi = 1/\sqrt{8\pi na}$ is the characteristic lengthscale determining the position of the crossover between the acoustic and free-particle regimes.

We note that there are two distinct effects within the Bogoliubov theory that both act to reduce the number of atoms in the zero-momentum state. Firstly, there is a mixing of basis states: the ground state of the interacting gas has some overlap with the finite-$\mathbf{k}$ states from the non-interacting theory, even when there are no real excitations present in the gas. As a consequence, one expects fewer ground-state atoms to be in the zero-momentum state as compared with the non-interacting case; this is termed the *quantum depletion*. Secondly, real thermal excitations in the finite-$\mathbf{k}$ states of the non-interacting theory further deplete the condensate. Adding a

[10] Strictly speaking, this argument requires the rather unphysical assumption of an infinitely large system, or periodic boundary conditions, but it nevertheless provides a reasonable approximation in most instances.

real excitation with momentum $\hbar\mathbf{k}$, while keeping the total atom number constant, reduces the number of particles in the zero-momentum state by [22]

$$p(k) = \frac{\mu + \hbar^2 k^2/(2m)}{\sqrt{\hbar^2 k^2/(2m)[\hbar^2 k^2/(2m) + 2\mu]}}, \tag{2.58}$$

and increases the thermal atom number by the same amount.

2.9 Spatial correlations

We now consider the degree to which properties of the gas at one position are correlated with those at a different position. As in the previous section, our system is a homogeneous Bose gas, prepared in equilibrium at a temperature T. In the $T \to \infty$ limit, the properties of the gas at two different positions are completely uncorrelated with one another and the gas is said to be spatially incoherent. In contrast, as $T \to 0$, all of the particles within the gas occupy the zero-momentum mode and form a pure condensate. This state is perfectly spatially coherent: neglecting finite-size effects, the phase of the condensate's wavefunction is equal at all points within the gas. More generally, including for both finite-temperature and non-equilibrium states, the degree of spatial coherence can be quantified by evaluating the spatial correlation functions.

Before we define the correlation functions, however, we will first introduce some useful notation using the second-quantisation formalism. This inherently many-body formalism compactly describes large numbers of particles, and automatically encodes the bosonic exchange symmetry that we introduced in section 2.1. For a more in-depth treatment of these topics, we refer the reader to [36,37].

We describe the quantum state of the system using Fock (or number) states, i.e., we write $|N_0, N_1, \ldots, N_i, \ldots\rangle$ to denote the state with N_i atoms in the i^{th} momentum mode. Each momentum mode is associated with a mode function $\varphi_i(\mathbf{r})$. The quantum state can be altered using the annihilation and creation operators, $\hat{a}_i$ and $\hat{a}_i^\dagger$ respectively, which we define by their action on a state,

$$\hat{a}_i|N_0, N_1, \ldots, N_i, \ldots\rangle = \sqrt{N_i}|N_0, N_1, \ldots, N_i - 1, \ldots\rangle \quad \text{and} \tag{2.59a}$$

$$\hat{a}_i^\dagger|N_0, N_1, \ldots, N_i, \ldots\rangle = \sqrt{N_i + 1}|N_0, N_1, \ldots, N_i + 1, \ldots\rangle\,. \tag{2.59b}$$

The operators therefore either destroy or create a particle in the i^{th} momentum mode, and can be combined in order to extract the number of particles in a given mode, i.e.,

$$\langle N_0, N_1, \ldots, N_i, \ldots|\hat{a}_i^\dagger\hat{a}_i|N_0, N_1, \ldots, N_i, \ldots\rangle = N_i\,. \tag{2.60}$$

The $\hat{a}_i$ and $\hat{a}_i^\dagger$ operators maintain the exchange symmetry provided they obey certain appropriate commutation relations. For bosonic systems, $\hat{a}_i$ and $\hat{a}_i^\dagger$ satisfy[11]

$$[\hat{a}_i,\, \hat{a}_j^\dagger] = \delta_{ij}\,, \qquad \text{and} \qquad [\hat{a}_i^{(\dagger)},\, \hat{a}_j^{(\dagger)}] = 0\,, \tag{2.61}$$

where δ_{ij} is the Kronecker delta. Since we are interested in correlations in the position basis, however, it is often more convenient to use the Bose field operator,

$$\hat{\Psi}(\mathbf{r}) = \sum_i \varphi_i(\mathbf{r})\hat{a}_i, \tag{2.62}$$

and its Hermitian conjugate[12]. These two new operators destroy and create particles at a position $\mathbf{r}$, rather than in one particular momentum mode, and obey the commutation relations

$$\left[\hat{\Psi}(\mathbf{r}),\, \hat{\Psi}^\dagger(\mathbf{r}')\right] = \delta^{(3)}(\mathbf{r}-\mathbf{r}')\,, \qquad \text{and} \qquad \left[\hat{\Psi}^{(\dagger)}(\mathbf{r}),\, \hat{\Psi}^{(\dagger)}(\mathbf{r}')\right] = 0\,, \tag{2.63}$$

which follow from Eq. (2.61), and the completeness and orthonormality of the set of mode functions, $\{\varphi_i(\mathbf{r})\}$.

Armed with the field operator, we now define the spatial correlation functions. These are the expectation values of products of the field operator and its Hermitian conjugate. Of particular interest for us is the simplest such combination, the so-called first-order two-point correlation function,

$$G^{(1)}(\mathbf{r},\, \mathbf{r}') = \langle \hat{\Psi}^\dagger(\mathbf{r})\hat{\Psi}(\mathbf{r}')\rangle\,, \tag{2.64}$$

which is a measure of the degree of phase coherence between positions $\mathbf{r}$ and $\mathbf{r}'$. The correlation function is often normalised such that its value is unity for $\mathbf{r} = \mathbf{r}'$, i.e.,

$$g^{(1)}(\mathbf{r},\, \mathbf{r}') = \frac{G^{(1)}(\mathbf{r},\, \mathbf{r}')}{\sqrt{G^{(1)}(\mathbf{r},\, \mathbf{r})G^{(1)}(\mathbf{r}',\, \mathbf{r}')}}\,. \tag{2.65}$$

We note that the two terms under the square root correspond physically to densities at $\mathbf{r}$ and $\mathbf{r}'$ respectively. One can show (e.g., [38, 39]) that

$$g^{(1)}(\mathbf{r}, \mathbf{r}') \propto \int \mathrm{d}^3\mathbf{k}\, \exp(i\mathbf{k}\cdot(\mathbf{r}-\mathbf{r}'))\, n_k(\mathbf{k})\,, \tag{2.66}$$

i.e., $g^{(1)}$ is proportional to the Fourier transform of the momentum distribution. This equivalence is key to connecting the equilibrium and non-equilibrium dynamics that we will be considering in chapter 5.

The general j^{th}-order correlation function is given by

$$G^{(j)}(\mathbf{r}_1,\, \ldots,\, \mathbf{r}_j;\, \mathbf{r}_{j+1},\, \ldots,\, \mathbf{r}_{2j}) = \left\langle \left(\prod_{i=1}^{j} \hat{\Psi}^\dagger(\mathbf{r}_i)\right) \left(\prod_{i=1}^{j} \hat{\Psi}(\mathbf{r}_{i+j})\right) \right\rangle\,. \tag{2.67}$$

[11] Fermionic systems can be described with the same formalism, but using instead the *anti*-commutators in Eq. (2.61).

[12] The discrete momentum basis can be extended to a continuous one in the usual way: by replacing sums with integrals, and particle numbers with momentum-space densities.

We state here without proof (see, e.g., [36]) that the set of all possible such functions constitutes complete knowledge of the state of the system, and they are therefore a very powerful tool for studying quantum systems. Equivalently, the expectation values of all Hermitian operators can be expressed in terms of the correlation functions. In practice, and particularly for weakly interacting systems, much of the interesting physics is captured using only the first- and second-order correlation functions. As such, spatial correlation functions can be a relatively compact representation for approximating a complex many-body system.

Finally, we consider the subset of functions of the form given in Eq. (2.67) for which $\{\mathbf{r}_{j+1}, \ldots, \mathbf{r}_{2j}\}$ is a permutation of $\{\mathbf{r}_1, \ldots, \mathbf{r}_j\}$. These functions are usually referred to as the j^{th}-order *density-density* correlation functions, given along with their normalised forms by

$$G^{(j)}(\mathbf{r}_1, \ldots, \mathbf{r}_j) = \left\langle \left(\prod_i^j \hat{\Psi}^\dagger(\mathbf{r}_i) \right) \left(\prod_i^j \hat{\Psi}(\mathbf{r}_i) \right) \right\rangle , \qquad \text{and} \tag{2.68a}$$

$$g^{(j)}(\mathbf{r}_1, \ldots, \mathbf{r}_j) = \frac{G^{(j)}(\mathbf{r}_1, \ldots, \mathbf{r}_j)}{\prod_j G^{(1)}(\mathbf{r}_j, \mathbf{r}_j)} . \tag{2.68b}$$

Note the lack of the square root in the denominator here, which is due to the correlations being density-density ones, rather than correlations in the field itself. These correlation functions give the probabilities of simultaneously finding one particle at each of the $\mathbf{r}_j$, and are useful when evaluating collision rates for two- and three-body collisions (e.g., as in chapter 4).

3 Experimental platform

The experiments described in chapters 5 and 6 of this thesis were performed using a gas of ultracold ^{39}K confined in an optical box trap. Our platform combines the attractive features of its in-house predecessors: it offers a 3D quasi-uniform trapping potential modelled closely upon the ^{87}Rb experiment 'BEC I' [9,40], but drew inspiration for its general design, and makes use of the species-specific cooling techniques, from the ^{39}K experiment 'BEC II' [41–44]. The full details of construction and characterisation of the experiment used in this work (aptly named 'BEC III') can be found in [10, 45], with more up-to-date details available in [11]; here we provide a brief overview to help orient the reader.

In section 3.1 we describe the initial cooling stages of the experiment, which culminate in the formation of quasi-pure condensates in an optical box trap. Section 3.2 provides details of the imaging technique we use to detect our atomic samples. Finally, in section 3.3, we conclude the chapter with a description of some of the tools available to us for manipulating the atoms.

3.1 Producing ultracold samples

Here we outline the initial stages of our experiment, which we use to produce quasi-pure homogeneous BECs with densities of up to $10^{19}\,\mathrm{m}^{-3}$. Section 3.1.1 contains a general overview of the experimental apparatus and the cooling methods we use to reach temperatures in the nanokelvin regime. Section 3.1.2 then describes the phase-imprinting technique we use to create a uniform trapping potential, and provides quantitative benchmarks for the uniformity of the trap.

3.1.1 Bose–Einstein condensation of ^{39}K

The experimental system consists of two optically accessible chambers separated by a long, narrow feedthrough tube. The chambers are kept under ultra-high vacuum by two ion pumps that are located along the feedthrough tube; this configuration maintains a pressure differential between the two chambers.

Our experiments begin at the higher-pressure chamber, where a background vapour of ^{39}K atoms is maintained by regularly discharging getter material that resides inside the vacuum chamber. We capture and laser cool a sample of the atoms from the background vapour in a three-dimensional magneto-optical trap (MOT), which combines a magnetic quadrupole trap

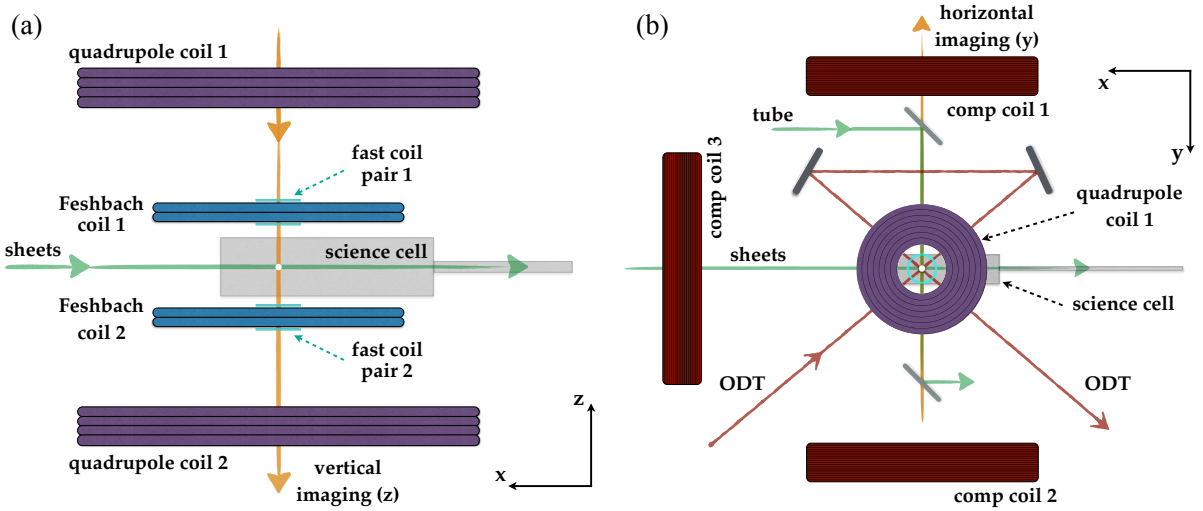

Figure 3.1 | **Schematic of the science cell surroundings.** We show here the laser beams and magnetic-field coils used to prepare and manipulate our samples of ^{39}K. **(a)** Side view along $-y$. **(b)** View from above. The optical dipole trap used for evaporation is shown in dark red, the light used to form the uniform box potential (sheets and tube) is shown in green, and the imaging light is shown in orange. The atom location is marked with a white circle. The Feshbach coils (blue) create a uniform magnetic field. The quadrupole coils (purple) trap and transport atoms to the science cell. Compensation coils (brown), in conjunction with quadrupole coil 2, are used to magnetically levitate the atomic sample. Auxiliary 'fast' coils (cyan) allow the magnetic field to be rapidly changed. Figure reproduced from [11].

with laser beams that are red-detuned from the D2 cooling transition. We then further cool the sample using a grey molasses technique [46–48] on the D1 line[1], reaching sub-Doppler temperatures of $\sim 10\,\mu$K. Next, we optically pump the atoms into the $4^2S_{1/2}\,|F = 2, m_F = 2\rangle$ hyperfine state, and confine them in a magnetic quadrupole trap. The $\sim 3 \times 10^8$ magnetically trapped atoms are then transported mechanically[2] along the feedthrough and into the second, lower-pressure chamber, which we refer to as the 'science cell'. Here, the $\sim 10^{-12}$-mbar pressure supports long sample lifetimes; in the absence of density-dependent loss processes, we measure lifetimes exceeding 100 s.

Fig. 3.1 shows a detailed overview of the coils and laser beams surrounding the science cell. With the atoms still magnetically trapped after the transport process, we ramp on an optical dipole trap (ODT) generated from a 20-W 1070-nm laser beam. The ODT is in a bow-tie configuration, comprising a 30-µm–waist beam crossed with a recycled beam of waist $\sim 100\,\mu$m. Switching off the magnetic trap leaves $\sim 10\,\%$ of the atoms trapped in the ODT. The atoms are then transferred from the $|2, 2\rangle$ state to the hyperfine ground state, $|1, 1\rangle$, using a radio-frequency Landau–Zener sweep. We proceed to cool the cloud further by evaporating optically, reducing the trap depth by a factor ~ 700 over a period of $\sim 5\,$s. In order to optimise

[1] Sub-Doppler cooling techniques are generally less effective when using the D2 line of ^{39}K because of its small hyperfine splitting [49].

[2] The coils that generate the magnetic quadrupole trap are mounted on a programmable motorised track.

the efficiency of the evaporation, we tune the rate of scattering events, which redistribute energy within the sample, using a Feshbach resonance for the $|1, 1\rangle$ state (see section 3.3.1). We typically form BECs in the ODT of up to $\sim 4 \times 10^5$ atoms with condensed fractions of around 50 %[3]. The total time to produce such a condensate in the ODT during a single experimental run is ≈ 20 s.

3.1.2 Optical box potential

We now proceed to load the condensate from the ODT into our quasi-uniform optical box potential. Our implementation of the box potential follows that used in [9,40], and the technical details specific to our experiment are described in [10].

The basic idea is as follows. The optical box is formed using a nearly gaussian 532-nm laser beam, sourced from a Laser Quantum GEM 532 laser. This wavelength is blue-detuned from the D1 and D2 lines of ^{39}K, such that the light creates a repulsive dipole potential for the atoms [26]; the atoms reside in the dark regions bounded by the walls. We stabilise the power of the beam using an acousto-optic modulator and proportional-integral feedback control system. The stabilised beam is then expanded in a telescope and reflected off a phase-only spatial light modulator (SLM), which imprints a position-dependent phase profile onto the beam. This phase information is then converted to intensity by passing the phase-imprinted beam through a focussing lens. In this manner, we produce three spatially-resolved beams in the focal plane: one pseudo-Laguerre–Gauss beam that forms the 'tube' of the cylinder, and two thin 'sheet' beams that form its end caps. We combine these beams to form a cylindrical trap by first separating the tube beam from the two sheets using a D mirror, and reimaging them[4] at a right angle inside the science cell (see Fig. 3.1). The cylinder's rotational axis of symmetry lies along the y direction indicated in the figure.

We partially compensate for aberrations introduced by the optical elements along the beam path by using a wavefront correction procedure [10] based on previous work [50, 51]. Since we want the potential to be uniform within the box, we compensate for gravity by magnetically levitating the atoms, and also cancel the residual magnetic fields. We are able to achieve field gradient cancellation such that the atoms' net acceleration $\sim 10^{-4} g_0$, where g_0 is the local acceleration due to gravity.

We load the partially condensed sample from the crossed ODT into the box potential by first ramping up the intensity of the box, then lowering the intensity of the ODT. To ensure that the box-trapped condensates are as pure as possible, and to compensate for any effective

[3] Whilst evaporating further does achieve higher condensed fractions in the ODT, we find that it actually decreases the final atom number in the box trap. This is partially due to changes in the size of the condensed component, and its overlap with the optical box potential.

[4] The laser's short coherence length ~ 1 cm reduces unwanted interference effects.

heating due to the mode mismatch between the ODT and the box trap, we perform a final stage of evaporation in the box[5] by lowering the depth to $\lesssim k_B \times 50\,\mathrm{nK}$. We produce box-trapped samples that have condensed fractions $> 95\,\%$ and atom numbers of up to 3.5×10^5, with a shot-to-shot standard deviation of around $3\,\%$. We can vary the atom number by tuning the scattering length during the evaporation stage before loading into the box; increased three-body losses at higher a result in lower final atom numbers.

The thermodynamic properties of our Bose gases, trapped in this quasi-uniform potential, are consistent with an $r^{15(4)}$ power-law potential [10]. For most purposes in this thesis, however, it will suffice to treat the trap as a uniform cylindrical box of length L and radius R. The box dimensions are controlled by parameters of the SLM, which may be varied between experiments[6]. Typically, we have $R \approx 15\,\mu\mathrm{m}$ and $L \approx 50\,\mu\mathrm{m}$, however we are able to achieve reasonable uniformity for box dimensions in the range $(10-70)\,\mu\mathrm{m}$. At the short end of this range, finite optical resolution leads to the walls being insufficiently sharp, and the long end of the range is limited by the residual curvature of the magnetic fields, which is associated with harmonic (anti-)trapping frequencies of magnitude $\approx 2\pi \times 1\,\mathrm{Hz}$ [10, 11].

Should we wish to begin with a thermal or partially condensed sample, rather than a quasi-pure condensate, we first load a pure condensate into the box as described above, and then 'reheat' it. This approach, as opposed to transferring a thermal sample directly from the ODT, avoids loading cold atoms into trapping regions outside of the box potential[7]. To heat the sample, we raise the depth of the box trap by increasing the green laser intensity, and then apply a magnetic field gradient along the z direction, which we subsequently oscillate at $\sim 100\,\mathrm{Hz}$. Control over the trap depth, field-gradient amplitude, and initial atom number allows us to prepare samples at various temperatures $\lesssim 200\,\mathrm{nK}$ and condensate fractions [10].

3.2 Imaging atoms

The entire process described in the previous section, starting from a room-temperature gas in the MOT chamber, through to a uniform nanokelvin-temperature gas in the science cell, takes $\approx 20\,\mathrm{s}$. We then perform experiments on the gas (typically between $2\,\mu\mathrm{s}$ and several seconds long), before recording an absorption image [26], from which we are able to determine properties of the sample including the number of atoms and their energy. A typical experimental cycle, accounting for the preparation, manipulation, and detection of a sample, as well as

[5] Evaporation in a three-dimensional box geometry is generally less efficient than in lower-dimensional and harmonic traps, which can benefit from runaway evaporation (see, e.g., [52]).

[6] The 60-Hz refresh rate of our Hamamatsu X10468-04 SLM precludes dynamic changes on experimentally relevant timescales.

[7] Such regions form, e.g., due to the combined effect of weak residual magnetic trapping along the y direction, and confinement in the transverse plane from the tube beam.

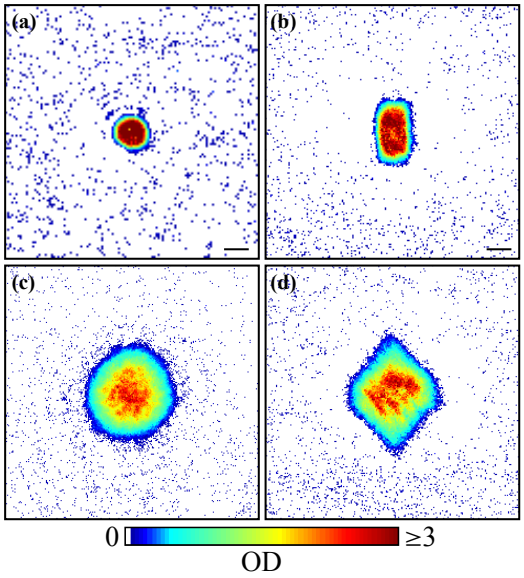

Figure 3.2 | **Absorption images of box-trapped BECs. (a, b)** In-situ images using horizontal and vertical imaging, respectively. The actual optical density in the trap centre is greater than the maximum value of ≈ 3 that we can measure reliably. The scale bar corresponds to 30 µm. **(c, d)** Time-of-flight images taken after a period of expansion in the presence of interactions. Figure reproduced from [11].

technical overheads, yields a new image of the atoms every $\approx 30\,\mathrm{s}$. This imaging process is destructive; after taking an image, we must prepare a fresh ultracold sample starting from a room-temperature gas.

To image the atoms, we turn off the magnetic fields, optically pump the atoms into the $|F = 2\rangle$ manifold[8], and then shine an imaging beam onto the atoms, which is resonant with the $|F = 2\rangle \rightarrow |F' = 3\rangle$ transition of the D2 line. As shown in Fig. 3.1, the imaging beam can be directed either horizontally, i.e., along the cylinder's symmetry axis, or vertically. The imaging beam has a low intensity, $I \approx 0.1\, I_\mathrm{s}$, where $I_\mathrm{s} = 1.75\,\mathrm{mW\,cm^{-2}}$ is the saturation intensity of the transition[9].

After the imaging beam passes through the atoms, we capture its intensity using a camera[10]. We calculate the optical density (OD), the logarithm of the ratio of incident to transmitted intensity, at each position in the beam's transverse profile. Combining this with the cross-section for absorption, we can infer the column density of our atomic sample, i.e., the two-dimensional, line-of-sight–integrated density. In Fig. 3.2 we show typical absorption images of quasi-pure homogeneous condensates, taken along our two imaging directions. We show in-

[8] We pump on the D1 transition, into the $|F' = 2, m'_F = 2\rangle$ state, which subsequently decays back to the $|F = 2\rangle$ manifold of the $4^2\mathrm{S}_{1/2}$ state. The decay branches into both $|2, 2\rangle$ and $|2, 1\rangle$. Since only the former of these branches corresponds to a closed imaging transition, our atom-number detection is not 100 % efficient. Replacing the pumping with an essentially 100-%–efficient LZ transfer increases the measured atom number by a factor of 1.32(1) [11]. We account for this factor in all the data presented in this thesis.

[9] Various properties of transitions in potassium are summarised in [30].

[10] We use a pco.pixelfly usb CCD camera for vertical imaging, and an Andor Zyla sCMOS camera for horizontal imaging.

situ images in Fig. 3.2(a,b), which highlight the cylindrical shape of the trap. In Fig. 3.2(c,d) we show time-of-flight absorption images, for which the samples have been allowed to expand in the presence of interactions; the diamond-like shape reveals the gas' quantum nature [40,53,54].

3.3 Manipulating the cloud

In this section, we describe some of the tools that are available to us for manipulating and probing the cloud. We begin in section 3.3.1 with our ability to tune interactions via our Feshbach coils, and a description of our auxiliary 'fast' coils, which allow us to change the interaction strength on timescales $\sim 1\,\mu s$. In section 3.3.2 we describe our radio-frequency spectroscopy, which we can use both to transfer atoms from $|1,1\rangle \rightarrow |1,0\rangle$, and to precisely determine the magnetic field strength at the location of the atoms. Finally, in section 3.3.3, we summarise the main features of our implementation of Bragg spectroscopy, which can be used to impart momentum to our atomic samples.

3.3.1 Tuning interactions

One of the key features of our experimental platform is the ability to tune the strength of interactions between atoms in the gas. We discussed in section 2.5 how this can theoretically be achieved via molecular Feshbach resonances; here we describe our experimental implementation.

We recall from Eq. (2.34) the dependence of the scattering length a on the magnetic field strength B in the vicinity of a Feshbach resonance,

$$a(B) = a_{\mathrm{bg}}\left(1 - \frac{\Delta}{B - B_\infty}\right), \tag{3.1}$$

where a_{bg} is the background scattering length, Δ is the resonance width, and B_∞ is the resonant field strength. The width is defined as the change in magnetic field between the resonance and the zero crossing, i.e., $a(B_\infty - \Delta) = 0$. In Fig. 3.3 we show a sketch of the resonances for both the $4^2S_{1/2}\,|1,\,1\rangle$ and $|1,\,0\rangle$ hyperfine states of ^{39}K at around 400 G.

We generate the Feshbach magnetic field using two coils in close-to-Helmholtz configuration [10], as shown in Fig. 3.1. Each coil comprises two layers of seven turns of hollow-core, 4-mm–diameter wire. The coil centres are symmetric about the science cell, located a distance of ≈ 23 mm above and below the atoms, and have an inner diameter of 70 mm. The coils produce a magnetic field of $B \sim 395$ G at an operating current of 167 A. Additional compensation coils provide fine adjustment of the field orientation, compensation for gravity, and cancellation of any residual magnetic gradients.

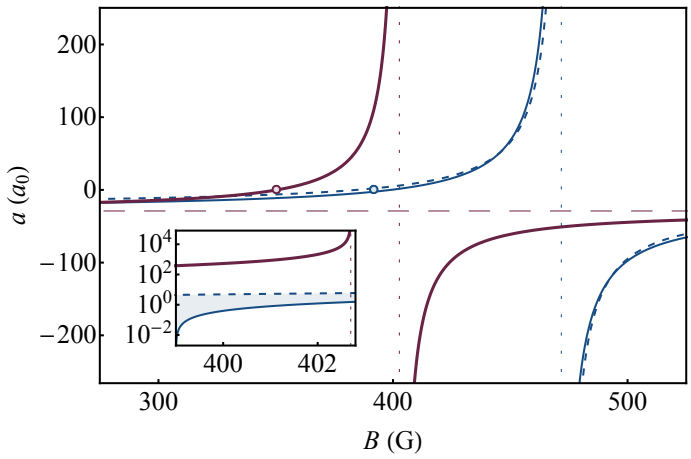

Figure 3.3 | **Feshbach resonances in ^{39}K.** We plot the resonances in the $|1, 1\rangle$ (red) and $|1, 0\rangle$ (blue) hyperfine states at around 400 G. Vertical dotted lines indicate the approximate positions of the resonance, while the horizontal dashed line shows the background scattering length a_{bg} for the $|1, 1\rangle$ state; a_0 denotes the Bohr radius. Open circles indicate the positions of the zero crossings. For the $|1, 1\rangle$ state, we plot Eq. (3.1) with $a_{\mathrm{bg}} = -29\,a_0$ [55, 56], and the empirical values $B_\infty = 402.70(3)$ G [57] and $\Delta = -52.25(4)$ G [58]. For the $|1, 0\rangle$ state, we plot theoretical predictions from [55] (solid) and [56] (dashed). Inset: Zoom in near the $|1, 1\rangle$ resonance, on log-linear axes. The $|1, 0\rangle$ state is very weakly interacting near the $|1, 1\rangle$ resonance. Figure reproduced from [11].

We vary B, and therefore a, by adjusting the current in the coils, while endeavouring to maintain compensation of the B-field gradients throughout. The inductance of the coils restricts the speed of adjustments to timescales of a few milliseconds [11].

Auxiliary 'fast' coils

In experiments that require changes to the scattering length on microsecond timescales, such as our quench experiments into the unitary regime (see chapter 6), we utilise a set of auxiliary 'fast' coils in addition to our main Feshbach coils. As shown in Fig. 3.1, there are four auxiliary coils in total: two are placed symmetrically about the upper Feshbach coil and two symmetrically about the lower one. Each of the four coils consists of three turns of wire, has a 25-mm inner diameter, and is positioned ~ 5 mm above or below the centre of one of the main Feshbach coils. The currents in the two innermost coils flow in the same direction (i.e., Helmholtz-like), so as to add directly to the main Feshbach field; the outer-coil currents flow in the opposite one. The strategic placement of the coils generates a nearly uniform field at the location of the atoms, while producing almost zero field in the planes of the main Feshbach coils. The auxiliary coils therefore have a very low inductive coupling to the Feshbach ones, and so, provided they have sufficiently small self-inductance, can be used to rapidly change the magnetic field at the location of the atoms independently of the main coils.

The auxiliary coils are operated by means of the custom H-bridge electronics shown in

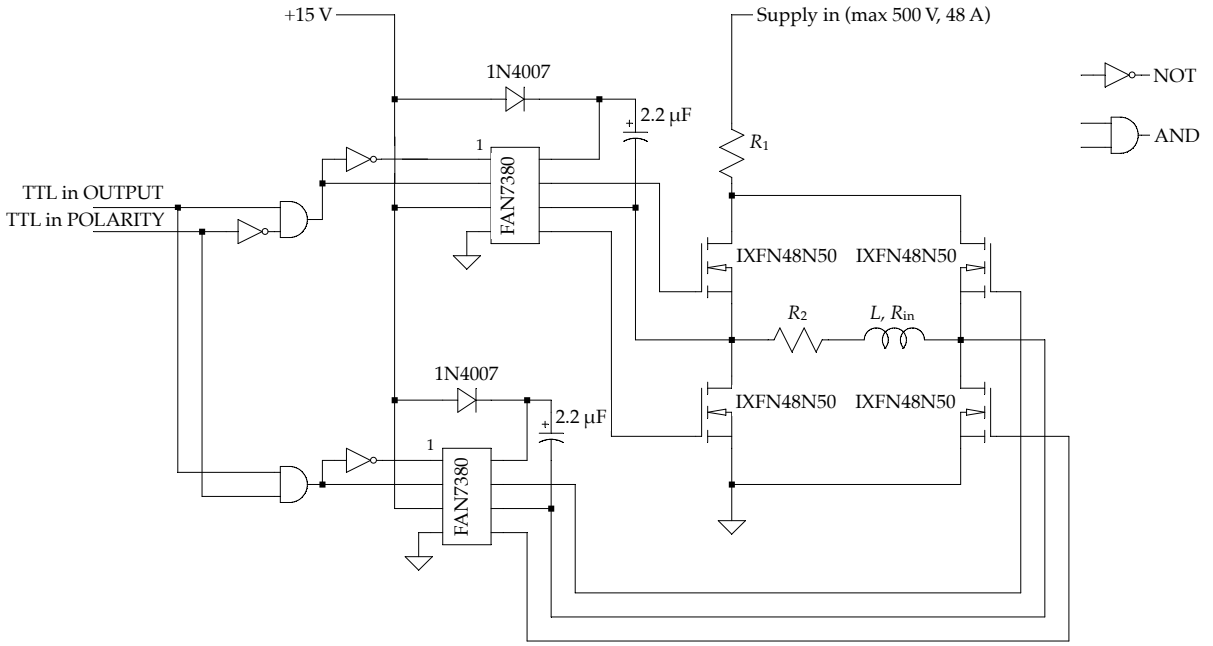

Figure 3.4 | **Circuit diagram of H-bridge used for rapid field switching.** The auxiliary B-field coils are represented by the inductor L_c, which also has an internal resistance R_{in}. Two FAN7380 half-bridge drivers control four N-channel IFXN48N50 MOSFETs, ultimately determining whether current flows through the auxiliary coils from left to right, from right to left, or not at all. The two resistors, R_1 and R_2, can be exchanged to adjust the characteristic LR-circuit response time that sets the rate of change of current in the coil. TTL signals are referenced to the circuit ground.

Fig. 3.4. We represent the coils by the inductor (marked L_c) that also has some internal resistance R_{in}. The purpose of the circuit is to enable rapid switching of the current flow through the coils: it can flow from left to right, from right to left, or the coil can be disconnected from the supply voltage altogether.

We use an Elektroautomatik PS9360-30 1U supply as the coils' main power source. The supply output can be changed via analogue inputs with response times $\sim 15\,\text{ms}$. Since the typical timescales of our experiments using the auxiliary coils are $\lesssim 2\,\text{ms}$, the power supply effectively behaves as a charged capacitor. Four N-channel IXFN48N50 MOSFETs act as electronic switches controlling the route of the conducting path from the supply input to ground. The conducting states of the MOSFETs are controlled by the two FAN7380 half-bridge–driver chips. These chips ensure that only one of the two MOSFETs on the left, and one of the two MOSFETs on the right, is conducting at any given time, thereby preventing short circuits of the main supply voltage to ground.

The electronics take as inputs two 5-V TTL signals: one for switching the H-bridge output on and off, and one for the polarity. If the output is set high, and polarity low, then the top-

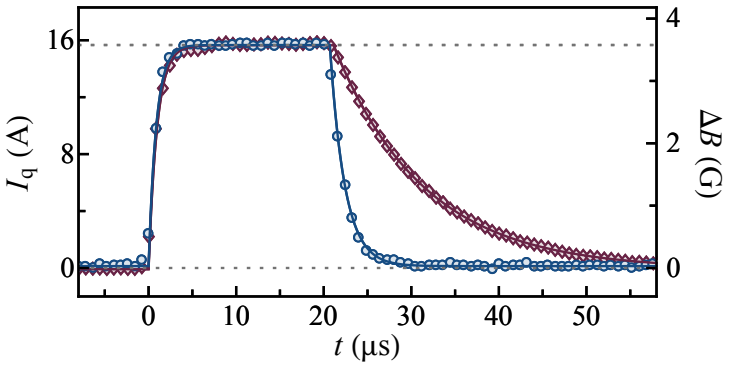

Figure 3.5 | **Current response of the auxiliary 'fast' coils.** The programmed pulse length is 20 μs. We calibrate the field-jump magnitude ΔB using rf-spectroscopy (see section 3.3.2), and assume that ΔB is proportional to the coil current I_q. Blue: $R_1 = 0$, $R_2 = 10\,\Omega$. Red: $R_1 = 10\,\Omega$, $R_2 = 0$.

left and bottom-right MOSFETs are conducting, while the remaining ones are effectively open circuits. This causes current to flow through the field coils from left to right as depicted in Fig. 3.4. If both the output and polarity are high, the MOSFETs' roles are inverted, and the current flows from right to left. If the output is low, the bottom two MOSFETs are conducting, while the top two are effectively open circuits. This final configuration isolates the coil from the supply, allowing the energy stored in the coils' magnetic field to be dissipated[11] over resistances R_{in} and R_2.

The H-bridge circuit can be used with currents of up to 48 A and voltages of up to 500 V; above these maximum ratings, the MOSFETs are liable to break down. The half-bridge drivers have nominal switching times[12] of ~ 200 ns, whereas the typical transient-response timescales for the resistor combinations we use with the coils are (1 – 10) μs. These transient timescales are therefore the dominant ones in determining the speed with which the magnetic field produced by the auxiliary coils changes.

We show the transient behaviour of the current in the coils in Fig. 3.5. Since the coils and resistors form LR circuits, the transient behaviour of the current $I_q(t)$ is described by exponential-decay curves, i.e., $I_q(t) \propto (1 - \exp(-t/\tau_{\text{in}}))$ when switching on, and $I_q(t) \propto \exp(-t/\tau_Q)$ when switching off. Here $\tau_{\text{in}} = L_c/(R_1 + R_2 + R_{\text{in}})$, and $\tau_Q = L_c/(R_2 + R_{\text{in}})$, i.e., the resistors R_1 and R_2 may be exchanged in order to adjust τ_{in} and τ_Q. Note that $\tau_{\text{in}} \neq \tau_Q$: when the H-bridge is in the 'on' state, current flows through both R_1 and R_2, however in the 'off' state, the current no longer flows through R_1. This distinction is important for our studies of the unitary Bose gas, discussed in chapter 6.

Fitting the curves in Fig. 3.5, along with data from additional combinations of R_1 and R_2, we obtain the τ_Q values listed in Table 3.1. We have verified that these extracted time constants are

[11] These MOSFETs always conduct in the reverse direction (i.e., from bottom to top in Fig. 3.4) due to built-in protective source-drain diodes.

[12] This switching time provides a security buffer to prevent shoot-through during switching.

independent of the choice of the supply voltage. For these data we have kept the sum $R_1 + R_2$ constant, and so the rise time $\tau_{in} \approx 1\,\mu s$ for all of these combinations. The values given are consistent with auxiliary coil parameters $L_c = 9.5(6)\,\mu H$ and $R_{in} = 0.94(6)\,\Omega$.

We calibrate the conversion from coil current I_q to magnetic field ΔB using radio-frequency spectroscopy (see section 3.3.2). We typically use a 30 µs time window during which the B field remains constant in order to measure the field with a suitable precision[13]. Since the transient behaviour in the auxiliary coils is faster than this, we assume that the current is directly proportional to the B field[14].

3.3.2 Radio-frequency spectroscopy

The scattering length a is a key control parameter for all of our experiments. In order to determine its value precisely, we first measure the magnetic field strength B where the atoms reside, and from this field strength we infer a. The cell geometry and the requirement for optical access to the science cell make the use of conventional B-field probes impractical. Instead, we determine the B field using radio-frequency (rf) spectroscopy on the atomic samples themselves.

We perform the spectroscopy by driving the transition between two internal hyperfine states of our atomic ensemble. The energies of the internal states depend on the strength of an externally applied magnetic field, and can be calculated using the Breit–Rabi formula [59]. The relevant empirical values for ^{39}K can be found in [60]. In Fig. 3.6(a) we plot the energy shifts, relative to the zero-field, hyperfine-free values, of states in the $4^2S_{1/2}$ $|F = 1\rangle$ and $|F = 2\rangle$ manifolds of ^{39}K as a function of $B \lesssim 500\,G$. For these values of B, both the energies themselves as well as the energy differences between neighbouring states vary with B. In this regime, one can therefore infer the magnetic field strength from the rf-photon energy that corresponds to

Table 3.1 | **Coil current 1/e fall times τ_Q for different resistor combinations.** We keep $R_1 + R_2 = 10\,\Omega$ constant in all cases, giving a rise time of $\approx 1\,\mu s$.

R_1 (Ω)	R_2 (Ω)	τ_Q ($\pm 0.2\,\mu s$)
10.0	0.0	10.2
9.0	1.0	4.5
7.4	2.6	3.0
6.6	3.4	2.3
0.0	10.0	1.2

[13] This is due to a combination of the limited RF power available and the Fourier broadening of the spectrum for shorter pulse times.

[14] We intend to implement two-photon Raman spectroscopy between the $|1, 1\rangle$ and $|1, 0\rangle$ states, which may provide better time resolution for a direct measurement of B than our radio-frequency spectroscopy.

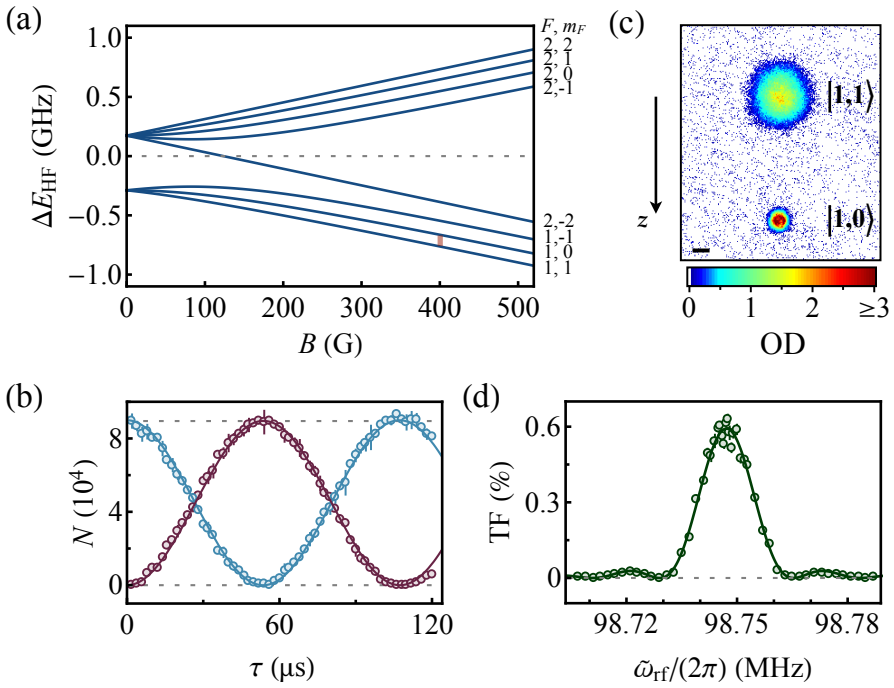

Figure 3.6 | **Radio-frequency spectroscopy. (a)** Hyperfine structure in the $4^2S_{1/2}$ ground state of ^{39}K as a function of B. **(b)** Measured atom number N in $|1, 1\rangle$ (blue) and $|1, 0\rangle$ (red) for an on-resonance pulse of duration τ. **(c)** Absorption image taken after a pulse transferring half of the atoms, and a 45-ms period of Stern–Gerlach separation; here $B = 399.38(1)\,\mathrm{G}$ [red bar in **(a)**], Scale bar corresponds to 50 μm. **(d)** Radio-frequency spectrum, showing the transferred fraction (TF) as a function of the applied frequency. The spectrum is centred at $\omega_{\mathrm{res}} = 2\pi \times 98.7471(1)$ MHz. Figure reproduced from [11].

transitions between the different states[15].

For our spectroscopy we use the transition between the ground state, $|1, 1\rangle$, in which we have typically prepared and experimented upon our atomic sample, and the $|1, 0\rangle$ state. For the purposes of this thesis, we are interested in fields for which the $|1, 1\rangle$ state has a non-negative scattering length, i.e., $\approx 350-405\,\mathrm{G}$ (see Fig. 3.3). In this range, the splitting between the states increases monotonically with the field strength; the transition frequencies, which lie between 95 MHz and 100 MHz, uniquely determine B with a sensitivity $\approx 50\,\mathrm{kHz\,G^{-1}}$.

We produce the rf field using an antenna that comprises a single turn of wire wound into a 70-mm–diameter coil, positioned $\simeq 25$ mm above the location of the atoms; see [61] for details. The antenna produces an electromagnetic wave oscillating at angular frequency $\tilde{\omega}_{\mathrm{rf}}$, introducing a perturbative Hamiltonian of the form

$$\hat{H}_{\mathrm{I}}(\tau) = \hat{H}_{\mathrm{I}}^0 \cos(\tilde{\omega}_{\mathrm{rf}}\tau)\,, \tag{3.2}$$

where $\hat{H}_{\mathrm{I}}^0 \propto |E_0|$ is a constant, and $|E_0|$ is the amplitude of the electric-field oscillation. For an atom initially prepared in the $|1, 1\rangle$ state, such a perturbation results in a probability of finding

[15] In contrast, in the large-B limit, or Paschen–Back regime, the stronger B field disrupts the coupling between the spin and orbital angular momenta of the atom and the energy differences between different internal states are no longer sensitive to B.

the atom in state $|1,\,0\rangle$ after time τ given by [26]

$$P_0 = \frac{\Omega^2}{\Omega^2+\delta^2}\sin^2\left(\sqrt{\Omega^2+\delta^2}\tau/2\right), \tag{3.3}$$

i.e., the system undergoes so-called Rabi oscillations with Rabi frequency $\Omega = \langle 1,\,0|\hat{H}_1^0|1,\,1\rangle/\hbar$. Here, $\delta = \tilde{\omega}_{\mathrm{rf}} - \omega_0$ is the detuning from resonance, and $\hbar\omega_0$ is the energy-level splitting [e.g., Fig. 3.6(a)]. We note that for a single-photon coupling scheme such as this one, Ω scales as $|E_0| \propto \sqrt{P_{\mathrm{rf}}}$, where P_{rf} is the supplied rf power. In Fig. 3.6(b) we plot an experimental measurement of the populations of both the $|1,\,1\rangle$ and $|1,\,0\rangle$ states as a function of time, while the atoms undergo a resonant Rabi oscillation with our rf-power–limited maximum $\Omega \approx 2\pi \times 9.3\,\mathrm{kHz}$. In the off-resonant case, as one can see from Eq. (3.3), one expects a suppressed maximum transfer efficiency and a higher effective Rabi frequency $\Omega_{\mathrm{eff}} = \sqrt{\Omega^2+\delta^2}$.

Fig. 3.6(c) shows a Stern–Gerlach measurement [62] of the populations of both states, where, in the presence of a magnetic field gradient, atoms in the two different m_F states have separated. At moderate field strengths of $\approx 400\,\mathrm{G}$ (as opposed to the zero-field limit), the force on an atom due to the magnetic gradient is given by

$$F_B = \frac{\partial \Delta E_{\mathrm{HF}}}{\partial B}\frac{\partial B}{\partial z}, \tag{3.4}$$

where ΔE_{HF} is a function of the quantum number m_F. We generally apply a magnetic gradient that cancels gravity for the $|1,\,1\rangle$ state, i.e., $mg_0 = (\partial \Delta E_{\mathrm{HF}}^{m_F=1}/\partial B)(\partial B/\partial z)$. The corresponding acceleration for the $|1,\,0\rangle$ state is then $g_0[1 - (\partial \Delta E_{\mathrm{HF}}^{m_F=0}/\partial B)/(\partial \Delta E_{\mathrm{HF}}^{m_F=1}/\partial B)] \approx 0.036 g_0$ for the 399.38(1)-G field used for the cloud shown in Fig. 3.6(c). For our 45-ms time of flight, this would correspond to a separation of $\approx 360\,\mu\mathrm{m}$, in agreement with our measured[16] 358(4) µm. We note also that the two components separate cleanly, with an apparent absence of inter-state scattering; this reflects the weak inter-state scattering length $0 < a \lesssim 10\,a_0$ [56].

We show a typical example of a high-resolution experimental rf spectrum in Fig. 3.6(d). The precision with which we are able to measure the resonance frequency typically corresponds to an uncertainty in the field strength at the milligauss level, which is smaller than the $\sim$ 10-mG drifts that we measure over the course of a day.

Mains oscillation

We can only achieve the few-milligauss precision in B for experiments in which the time required for the field-sensitive part of the experiment does not exceed a few millisecond. In longer experiments, the measured field shows periodic variations in B of amplitude $\sim 100\,\mathrm{mG}$, which occur due to the 50-Hz electric mains cycle.

[16] The effective pixel size of the camera, including the magnification of our imaging optics, has been independently calibrated using both micrometer-precision movements of the quadrupole coil track, and freefall acceleration of the atoms under gravity.

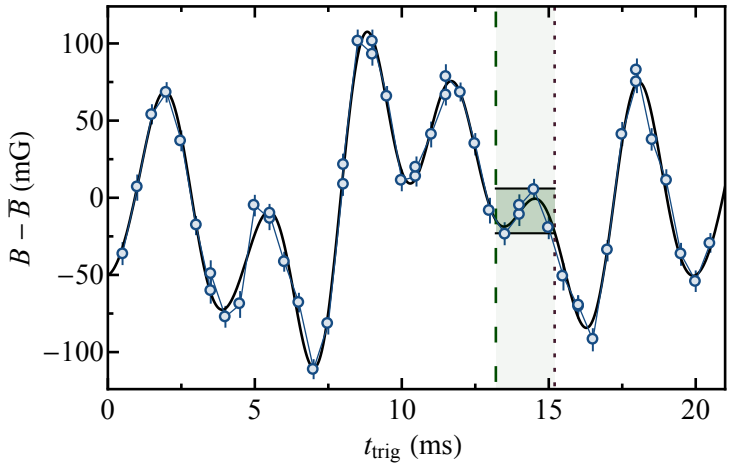

Figure 3.7 | **Characterising the mains oscillation.** We plot the variation in the magnetic field as a function of time t_{trig}, synchronised with the 50-Hz mains oscillation. The shaded region is a 2-ms window we have identified, during which the field changes by $\lesssim 30\,\mathrm{mG}$. We trigger experiments with dynamics on timescales $\ll 20\,\mathrm{ms}$ to begin at the start of this window; longer experiments average over the mains cycle. Figure reproduced from [11].

The magnetic field and its gradient are produced by a combination of coils (see Fig. 3.1) that draw current from power supplies connected to the 50-Hz alternating-current mains. This 50-Hz oscillation has a small coupling into each of the coils, and results in a 20-ms–periodic modulation of B. This $\sim$ 100-mG variation in field is a dominant contribution to our field noise, being larger than both the $\sim$ 10-mG typical drift in the field's time-averaged value over the course of a day, and the variations across the cloud from the $\approx 7\,\mathrm{G\,cm^{-1}}$ field gradient required to compensate for gravity.

Due to the shape of the Feshbach resonance (see Fig. 3.3), the oscillations in a caused by the changing B field can be severe for fields near the resonance, whereas closer to the zero crossing, the variation in a can typically be neglected. As concrete examples, at $B = 402.0\,\mathrm{G}$, corresponding to $2000\,a_0$, $\partial a/\partial B \approx 2720\,a_0\,\mathrm{G^{-1}}$. In contrast, for $B = 391.0\,\mathrm{G}$, corresponding to $100\,a_0$, the same gradient is only $11\,a_0\,\mathrm{G^{-1}}$. Moreover, at these lower values of a, the relevant experimental timescales are typically much longer than the oscillation period, and so we effectively average in time over the mains cycle.

We account for the effects of the mains oscillation by synchronising the experimental clock with the mains cycle immediately before field-sensitive parts of the experiment, including the rf spectroscopy described in the previous section. We can also map out the variation in B in detail, by waiting for a variable time t_{trig} following the mains trigger, and then measuring B using this same rf-spectroscopy technique. Fig. 3.7 shows the obtained deviation of B from

its time-averaged value[17]. The data are well captured by a Fourier series using the first ten harmonics of the base frequency $\nu_0 = 50\,\mathrm{Hz}$, i.e.

$$\sum_{j=1}^{10} c_j \sin(2\pi\,\nu_0\, j\, t_{\mathrm{trig}} + \varphi_j)\,. \tag{3.5}$$

The higher harmonics most likely arise due to coupling between the different power supplies used to control B, however the exact form is not crucial to our experiments.

Our experiments in the unitary regime (see chapter 6) require field stability to within $\lesssim$ 30 mG. We identify a 2-ms window following $t_{\mathrm{trig}} = 13.2\,\mathrm{ms}$ within which the field variations meet this criterion. We therefore use this value of t_{trig} in the unitary experiments, and indeed in any other experiments for which the critically sensitive part of the experiment occurs in $\lesssim 20\,\mathrm{ms}$.

3.3.3 Bragg spectroscopy

Two-photon Bragg scattering [63, 64] has become a staple feature of many modern ultracold atom experiments. An in-depth theoretical treatment can be found, e.g., in [26], and technical details of our implementation are available in [61, 65]. We include here a brief outline of the theory, and an overview of our experimental implementation.

In contrast to the historical x-ray diffraction from crystalline atomic lattices [66, 67], the Bragg spectroscopy used in ultracold atom experiments switches the roles of the light and atoms: here, it is the atoms that diffract from a periodic potential made of light. We illustrate the geometry in Fig. 3.8. Since we have a stationary cloud of atoms, we require a moving optical lattice in order to diffract the atoms. This can be achieved by interfering two beams, of frequencies ω_1 and ω_2, propagating with an angle θ between them. The key elements of the physics are revealed by considering the conservation of energy and momentum as an atom absorbs a photon from one beam, and reemits it into the second beam. The lattice coherently couples momentum states $|\hbar\mathbf{k}\rangle$ and $|\hbar(\mathbf{k}+\mathbf{q})\rangle$ that simultaneously satisfy

$$c|\mathbf{q}| = (\omega_1 + \omega_2)\sin(\tfrac{\theta}{2})\,,\ \text{and} \tag{3.6}$$

$$\hbar(\omega_1 - \omega_2) = \frac{\hbar^2|\mathbf{q}|^2}{2m} + \Delta E_{\mathrm{int}} + \frac{\hbar^2}{m}\mathbf{k}\cdot\mathbf{q}\,, \tag{3.7}$$

via an intermediate state $|i\rangle$. In the latter equation, ΔE_{int} denotes the difference in interaction energy between the two states, and the final term is the Doppler shift for an atom with a component of its momentum initially directed along $\mathbf{q}$.

[17] Each point plotted corresponds to the measured centre frequency of a 31-point rf spectrum, and the data were taken in randomised order. As these particular data were measured over $\approx$ 12 hours, they are also indicative of our field stability. We find the field's central value is stable within $\pm$10 mG over the course of a day, provided the experiment has been running for $\gtrsim$ 3 hours. We also find that this curve is reproducible when repeating the measurements at intervals of several months.

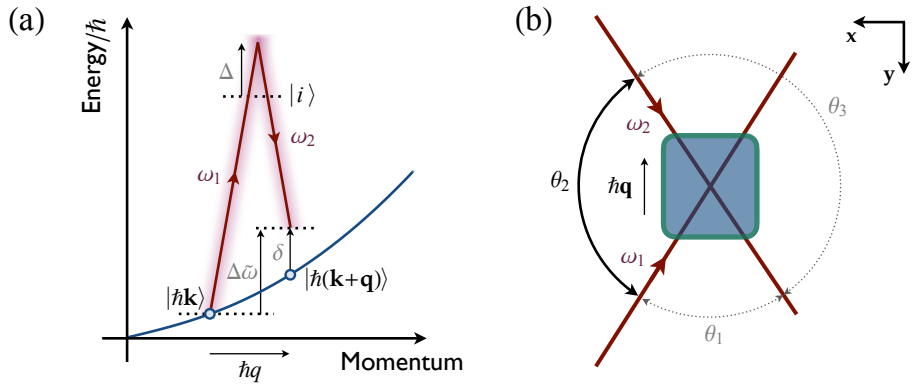

Figure 3.8 | **Schematic of Bragg spectroscopy. (a)** Energetics of the spectroscopy (not to scale). Two laser beams, of angular frequencies ω_1 and ω_2, couple momentum states $|\hbar\mathbf{k}\rangle$ and $|\hbar(\mathbf{k}+\mathbf{q})\rangle$ via the intermediate state $|i\rangle$. The blue line shows the atoms' dispersion relation, and the Bragg beams are resonant for the two states shown when $\delta = 0$. **(b)** Beam geometry (viewed from above), showing the intersection of the Bragg beams (red) at the location of the atoms (blue). In reality, the beam waists are $\approx 1\,\text{mm}$, and the box dimensions are $\approx 50\,\mu\text{m}$. We have access to the three marked angles $\theta_{\{1,2,3\}}$, depending on the direction along which we wish to impart momentum. Figure reproduced from [11].

During the Bragg pulse, atoms undergo Rabi oscillations between the $|\mathbf{k}\rangle$ and $|\mathbf{k}+\mathbf{q}\rangle$ states. The probability of measuring an atom in the state $|\mathbf{k}+\mathbf{q}\rangle$ is then given by the same expression we saw for the rf spectroscopy, Eq. (3.3). In this case, however, the Rabi frequency is given by the two-photon expression, namely

$$\Omega \simeq \Omega_1\Omega_2/(2\Delta)\,, \tag{3.8}$$

where $\Omega_{\{1,2\}}$ are the one-photon Rabi frequencies corresponding to each individual laser beam, Δ is the detuning from the intermediate state, and $|\Delta| \gg \Omega_{\{1,2\}}$. Since in this case the two-photon Rabi frequency contains the product of two transition matrix elements, here it is directly proportional to the light intensity (c.f. the root-power scaling in the single-photon case).

For our implementation, we use a pair of beams that are red detuned by $|\Delta| \approx 2\pi \times 1\,\text{GHz}$ from the D2 line, such that $k_{\text{rec}} = 2\pi/\lambda_{\text{D2}} = 8.2\,\mu\text{m}^{-1}$. The beams are $\hat{\pi}$-polarised, and their intensities are equal to within 5 %. Our beams are configured with $\theta_{\{1,2,3\}} = \{66.4°, 113.6°, 180°\}$ with corresponding $|\mathbf{q}| \in \{1.1, 1.7, 2.0\}\, k_{\text{rec}}$.

4 Saturation-driven cooling

Dissipation is often associated with adverse effects including particle loss, reduced coherence, and heating. It can, however, also be harnessed as a tool to study interesting quantum states [68–74] and non-equilibrium phenomena [9,75,76], or as a control mechanism for quantum computing [77–80]. In the specific context of ultracold Bose gases, atom loss can result in unexpected cooling effects. Collisions with atoms in the background vapour result in the quantum analogue of Joule–Thomson cooling [81,82] and it has recently been shown that three-body loss, which is traditionally considered a particularly egregious source of heating [83–85], can also result in cooling [86,87]. In this chapter we show that, under the right conditions, three-body loss can not only reduce the temperature of a Bose gas, but can even *purify* it, i.e., increase its condensed fraction. We first give an overview of the system, before reviewing some key requirements for the theory. We then examine the loss processes that underpin the cooling effect. Next, we examine an ideal-gas calculation[1] in order to emphasise the key physics. Finally, we show that the qualitative results are robust to the introduction of weak mean-field interactions, and identify a realistic region of experimental parameter space in which the effect might be able to be observed. The main results of this chapter have been published in [17].

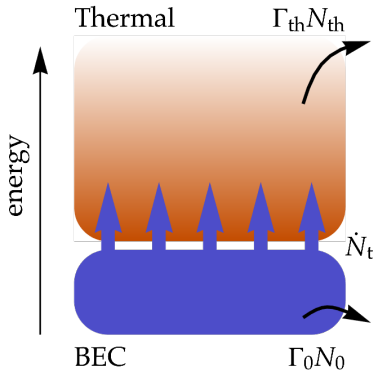

Figure 4.1 | **Saturation-driven cooling.** Thermal atoms (orange) lost at a rate $\Gamma_{\rm th}N_{\rm th}$ lead to a lack of saturation, and must be (partially) replenished by a flow of atoms $\dot{N}_{\rm t}$ (blue arrows) from the zero-energy condensate. Condensed atoms (blue) may also be directly lost at a rate $\Gamma_0 N_0$ without affecting the temperature. Figure adapted from [17].

4.1 Overview of the system

We consider a partially condensed, homogeneous gas of N atoms at temperature T. We are interested in how the thermodynamic properties of the gas evolve as atoms are removed by some generic loss mechanism, which may be density-dependent. It is assumed that the gas is undergoing continuous equilibration; at any instant in time, the number of thermal atoms $N_{\rm th}$ is saturated at the critical value for condensation $N_{\rm c}(T)$, and the remaining $N_0 = N - N_{\rm c}$ atoms are in the condensate.

[1] This calculation uses ideal-gas thermodynamics, but nevertheless assumes two- and three-body collisions take place.

In Fig. 4.1, we show the three kinds of processes that can take place as atoms are lost from the trap. Note that while the BEC and thermal components are depicted separately in terms of their energy, they occupy the same volume. Particles can

(*i*) be directly lost from the condensate, at a rate $\Gamma_0 N_0$;

(*ii*) be directly lost from the thermal cloud, at a rate $\Gamma_{\text{th}} N_{\text{th}}$; or

(*iii*) flow from the BEC into the thermal cloud, at a rate $\dot{N}_{\text{t}}$.

In general, the rates Γ_0 and Γ_{th} are both functions of N_0 and N_{th}, depending on the specific details of a particular loss mechanism.

Process (*iii*) is generically required in order to maintain thermal equilibrium. Atoms lost from the thermal cloud leave behind vacant thermal states that need to be filled. To remain in equilibrium, the gas must fill these vacancies using atoms from the condensate reservoir. The rate $\dot{N}_{\text{t}}$ at which atoms flow from the BEC into the thermal cloud depends on how the system's energy is distributed between the two components. In many typical experimental scenarios, the average energy of a condensate atom is lower than that of an atom in the thermal cloud. When this is the case, the promotion of the low-energy BEC atoms into the thermal cloud results in a decrease in the total thermal energy. This is the microscopic origin of saturation-driven cooling.

4.2 Advantages of homogeneity for cooling

It is important for the theory that the gas be homogeneous, with the condensed and thermal components spatially overlapped. Firstly, this ensures that the thermal component of the gas is saturated. It also allows us to exploit bosonic bunching to enhance the cooling by preferentially removing thermal atoms over condensate ones, an effect that is outweighed in harmonic traps by the much higher densities of condensate atoms [85]. We discuss these two aspects in more detail in this section, before proceeding to the ideal-gas version of our theory.

4.2.1 Saturation in a weakly interacting gas

In section 2.3, we saw that there exists a critical maximum number of thermal atoms, N_{c} in an ideal, fixed-temperature gas of bosons. Whilst the value of N_{c} is expected to vary in different trapping geometries, the basic idea that N_{th} saturates at some N_{c} applies generically for non-interacting Bose gases. Naïvely, one might expect this to also be true in the case of a weakly interacting gas. Experiments in harmonic traps, however, have shown both deviations in the position of the critical temperature [88, 89] as well as equilibrium thermal atom numbers that are significantly above N_{c} [39, 82, 90, 91]. Only by extrapolating to the strictly non-interacting limit could the ideal-gas behaviour be recovered [39, 82].

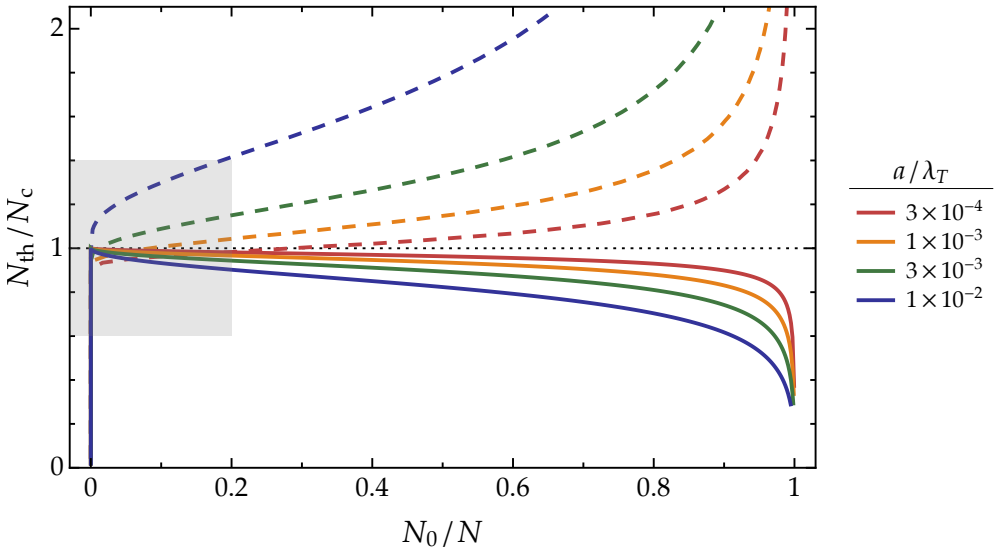

Figure 4.2 | **Numerical solutions of the Popov equations,** shown for various interaction strengths a/λ_T. Curves show the deviations of the thermal atom number $N_{\rm th}$ from its critical value $N_{\rm c}$ for both uniform (solid) and harmonic (dashed) traps, as a function of the condensed fraction N_0/N. The Popov approximation breaks down in the vicinity of the critical number (shaded box).

The violation of the saturation picture can be modelled at mean-field level using the Popov approximation [92–96], which extends the Bogoliubov dispersion [section 2.8] by allowing the condensate density to vary with temperature. We denote the local condensate and thermal densities n_0 and $n_{\rm th}$ respectively, and the local value of the potential is U. The Popov densities are then the self-consistent solutions to the system of equations

$$\varepsilon(k) = \left[\frac{\hbar^2k^2}{2m}\left(\frac{\hbar^2k^2}{2m} + 2gn_0\right)\right]^{1/2}, \tag{4.1a}$$

$$p(k) = \frac{\hbar^2k^2/(2m) + gn_0}{\varepsilon(k)}, \tag{4.1b}$$

$$\mu - U = gn_0 + 2gn_{\rm th}, \quad \text{and} \tag{4.1c}$$

$$n_{\rm th} = \frac{1}{(2\pi)^3}\int \mathrm{d}^3\mathbf{k}\, p(k)\left[\exp\left(\frac{\varepsilon(k)}{k_{\rm B}T}\right) - 1\right]^{-1}. \tag{4.1d}$$

Note the prefactors of the gn terms in Eq. (4.1c): while thermal atoms experience a mean-field energy of $g(2n_{\rm th} + 2n_0)$, condensate atoms have only $g(2n_{\rm th} + n_0)$. This is a consequence of the absence of exchange terms in the interaction between two atoms in the same (i.e. condensed) momentum state [22].

The local densities $n_{\{0,\rm th\}}$ are obtained numerically: after fixing (g, T), selecting n_0 uniquely determines both $n_{\rm th}$ and the difference $(\mu - U)$. This gives the mappings $f_{\{0,\rm th\}} : \mu - U \mapsto n_{\{0,\rm th\}}$, which may be used to generate the solutions for an arbitrary potential. The final solu-

tions are given by evaluating

$$N_{\{0,\mathrm{th}\}}(\mu) = \int d^3\mathbf{r}\, f_{\{0,\mathrm{th}\}}(\mu - U(\mathbf{r}))\,. \tag{4.2}$$

In a fixed geometry, these solutions depend only on the ratio a/λ_T, where λ_T is the thermal wavelength. This can be seen by changing to dimensionless variables. With $K = \lambda_T k/(2\sqrt{\pi})$, $M_{\{0,\mathrm{th}\}} = g n_{\{0,\mathrm{th}\}}/(k_\mathrm{B}T)$, and $\alpha = (\mu - U)/(k_\mathrm{B}T)$, Eq. (4.1) reads

$$p(K) = \frac{K^2 + M_0}{\sqrt{K^2(K^2 + 2M_0)}}\,, \tag{4.3a}$$

$$\alpha = M_0 + 2M_\mathrm{th}\,, \quad \text{and} \tag{4.3b}$$

$$M_\mathrm{th} = \frac{2}{\pi^{3/2}} \cdot \frac{a}{\lambda_T} \int \mathrm{d}^3\mathbf{K}\, p(K) \left[\exp(\sqrt{K^2(K^2 + 2M_0)}) - 1\right]^{-1}\,. \tag{4.3c}$$

The results for both homogeneous and harmonic trapping potentials are shown in Fig. 4.2. We see a strong violation of Einstein's ideal-gas picture (dotted line) for harmonic traps, even at weak interaction strengths, with the thermal atom number increasing significantly above the critical atom number as the condensed fraction increases. The uniform gas, in contrast, shows the opposite effect, and the deviation that it shows from the ideal-gas behaviour is much smaller in magnitude. Since saturation is a crucial ingredient in our cooling effect, homogeneous traps provide a significant advantage over their harmonic counterparts.

4.2.2 Loss mechanisms & correlations

Atoms can be lost from a trap by a number of different mechanisms. Ultracold Bose gases can lose atoms via processes including collisions with particles in the background vapour, interactions with external fields, and n-body collisions between trapped particles. Common examples of the latter are the two-body spin-exchanging collisions and three-body loss. Here we focus on the processes most relevant to our study[2]: background collisions and three-body recombination.

The probability that any particle in the cloud is lost due to a collision with a particle in the background vapour is independent of the atomic density. Since only one trapped particle is involved in this loss process, we refer to this mechanism as one-body loss. The corresponding loss rate depends on the density of background particles, i.e., species other than the atoms that we intentionally cool and trap, which is determined by the quality of the vacuum. The process is not energy-selective; on average, each collision of a background particle with a trapped one removes the average energy E/N. The per-particle loss rates of both the thermal and condensed components are therefore equal to the trap-averaged rate, $\Gamma_{1\mathrm{B}} \equiv -\dot{N}/N$, i.e.,

$$\Gamma_{1\mathrm{B}} = \Gamma_\mathrm{th} = \Gamma_0\,. \tag{4.4}$$

[2] Spin-exchanging collisions cannot occur between atoms in the hyperfine ground state.

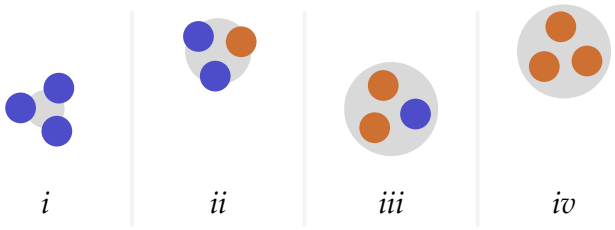

Figure 4.3 | Three-body recombination events in a partially condensed cloud. Recombination events involving different numbers of BEC (blue) and thermal (orange) atoms occur at different rates. Bosonic bunching leads to preferential removal of thermal atoms over condensed ones. The areas of the grey circles show the relative enhancements of the corresponding processes: the relative rates of processes *i–iv* are 1/3!, 1/2!, 1, and 1 respectively. Figure adapted from [17].

Three-body recombination events occur when three atoms in close proximity collide. Typically, two atoms come together to form a bound dimer, and the third atom is required in order to conserve both momentum and energy in the collision. This process is traditionally held as a source of heating in ultracold atom experiments [83–85], but here we show that in a homogeneous system, it can in fact be used to preferentially remove thermal atoms over condensed ones. The loss rate due to three-body recombination, Γ_{3B}, is given by

$$\Gamma_{3B} = -\frac{\dot{n}}{n} = g^{(3)} K_3 n^2 \,, \tag{4.5}$$

where $g^{(3)}$ denotes the zero-distance three-body correlation function (see section 2.9), and the three-body–loss coefficient K_3 includes the dependence on the scattering length a. In terms of the densities of the thermal and condensed atoms,

$$g^{(3)} = \frac{3!}{n^3}\left(\frac{1}{3!}n_0^3 + \frac{1}{2!}3n_0^2 n_{\rm th} + \frac{1}{1!}3n_0 n_{\rm th}^2 + \frac{1}{0!}n_{\rm th}^3\right) . \tag{4.6}$$

This is simply the binomial expansion of the total density $(n_0 + n_{\rm th})^3$, but includes additional factorials in the denominators of each term accounting for the lack of exchange terms involving the macroscopically occupied ground state[3]. The individual terms in Eq. (4.6), from left to right, correspond to the processes (*i-iv*) in Fig. 4.3 respectively.

In a uniform system, we can rewrite Γ_{3B} in terms of the total density $n = n_0 + n_{\rm th}$ and condensed fraction $\eta = N_0/N$, i.e.,

$$\Gamma_{3B} = K_3 n^2 (6 - 9\eta^2 + 4\eta^3) \,. \tag{4.7}$$

One then sees that the presence of three-body correlations makes recombination loss an energy-selective process, with thermal and condensed components of the cloud on unequal footings [83, 97–99]. The loss rate in a pure BEC ($\eta = 1$) is a factor of 3! times smaller than for a purely thermal gas ($\eta = 0$) of the same density. We further quantify this effect by splitting

[3] Similar considerations for the two-body correlation give $g^{(2)} = (n_0^2 + 4n_0 n_{\rm th} + 2n_{\rm th}^2)/n^2$.

each term of Eq. (4.6) into two separate contributions: one for each of the thermal and condensate loss rates. These contributions reflect the number of BEC and thermal atoms lost in the distinct process that corresponds to each term. The per-particle loss rates for each of the components depend on both the thermal and condensed atom numbers as

$$\Gamma_0 N_0 = K_3(\,1\,N_0^3 + 6\,N_0^2 N_{\rm th} + \;\; 6\,N_0 N_{\rm th}^2 + 0\,N_{\rm th}^3\,)/V^2\,, \tag{4.8}$$

$$\Gamma_{\rm th} N_{\rm th} = K_3(\,0\,N_0^3 + 3\,N_0^2 N_{\rm th} + 12\,N_0 N_{\rm th}^2 + 6\,N_{\rm th}^3\,)/V^2\,. \tag{4.9}$$

or written in terms of the total density and the condensed fraction,

$$\Gamma_0 = K_3 n^2(6 - 6\eta + \eta^2)\,, \quad \text{and} \quad \Gamma_{\rm th} = K_3 n^2(6 - 3\eta^2)\,. \tag{4.10}$$

4.3 Ideal-gas theory

We now develop the three-body cooling theory assuming ideal-gas thermodynamics, focussing on the roles of the saturation of the thermal component, and the three-body correlations. Here we assume that the only role of two-body interactions is to drive continuous thermalisation, keeping the system close to equilibrium at all times.

Under continuous equilibration, while the thermal component remains saturated, $N_{\rm th}$ is saturated at the critical value,

$$N_{\rm th} = N_{\rm c}(T) = V\zeta(\tfrac{3}{2})\left[\frac{m}{2\pi\hbar^2}\right]^{3/2}(k_{\rm B}T)^{3/2}\,, \tag{4.11}$$

and the energy, carried only by atoms in the thermal cloud, is given by

$$E_{\rm th} = \tfrac{3}{2}V\zeta(\tfrac{5}{2})\left[\frac{m}{2\pi\hbar^2}\right]^{3/2}(k_{\rm B}T)^{5/2}\,. \tag{4.12}$$

The rates of change of the two components of the gas, including the flow $\dot{N}_{\rm t}$ between them, are

$$\dot{N}_{\rm th} = -\Gamma_{\rm th} N_{\rm th} + \dot{N}_{\rm t}\,, \quad \text{and} \tag{4.13}$$

$$\dot{N}_0 = -\Gamma_0 N_0 - \dot{N}_{\rm t}\,, \tag{4.14}$$

and since only the direct loss of thermal atoms results in a change in the system energy, we also have

$$\dot{E}_{\rm th} = -(\Gamma_{\rm th} N_{\rm th})\left(\frac{E_{\rm th}}{N_{\rm th}}\right) = -\Gamma_{\rm th} E_{\rm th}\,. \tag{4.15}$$

Eqs. (4.11–4.15) together give

$$\Gamma_{\rm th} = -\tfrac{5}{3}\dot{N}_{\rm th}/N_{\rm th}\,, \quad \text{and} \quad \dot{N}_{\rm t} = -\tfrac{2}{3}\dot{N}_{\rm th} = +\tfrac{2}{5}\Gamma_{\rm th} N_{\rm th}\,, \tag{4.16}$$

i.e., for every 5 atoms lost from the thermal cloud, 2 are replaced from the condensate.

The fact that $E_{\rm th}$ is decreasing over time directly implies that T must also decrease. A more interesting question, however, is whether this decrease in temperature can also result in a decrease in the entropy per particle for the remaining atoms. The entropy per particle is

$$\begin{aligned} s &= \frac{1}{N}\int \mathrm{d}T\,\frac{1}{T}\frac{\partial E_{\rm th}}{\partial T} \\ &= \frac{5}{2}\frac{\zeta(\frac{5}{2})}{\zeta(\frac{3}{2})}\frac{N_{\rm th}}{N}k_{\rm B}\,, \end{aligned} \tag{4.17}$$

which is proportional to the thermal fraction $\bar{\eta} = 1-\eta = N_{\rm th}/N$. To see whether the gas purifies, we therefore calculate

$$\frac{\dot{\bar{\eta}}}{\bar{\eta}} = \frac{\dot{N}_{\rm th}}{N_{\rm th}} - \frac{\dot{N}}{N} = \Gamma(1-\mathcal{P})\,, \tag{4.18}$$

where we have introduced the purification coefficient

$$\mathcal{P} \equiv \frac{\dot{N}_{\rm th}/N_{\rm th}}{\dot{N}/N}\,, \quad \text{or equivalently} \quad \mathcal{P}-1 = \frac{\mathrm{d}[\ln(1-\eta)]}{\mathrm{d}[\ln(N)]}\,. \tag{4.19}$$

For $\mathcal{P} > 0$, the thermal atom number decreases, and so the gas cools. If also $\mathcal{P} > 1$, the entropy per particle will decrease, or equivalently the condensed fraction will increase. Using Eq. (4.16), this simplifies to

$$\mathcal{P} = \frac{3}{5}\frac{\Gamma_{\rm th}}{\Gamma}\,, \tag{4.20}$$

which we are now in a position to evaluate for appropriate choices of the loss rates $\Gamma_{0,\rm th}$.

The arguments presented thus far are specific to uniform traps, however they apply generally to any loss process that only differentiates between thermal and condensate atoms, but is not, e.g., selective between momentum classes within the thermal cloud[4]. Taking a constant one-body loss rate $\Gamma = \Gamma_{\rm th} = \Gamma_{\rm 1B}$, one obtains

$$\mathcal{P}_{\rm JT} = \tfrac{3}{5}\,; \tag{4.21}$$

this corresponds to the quantum Joule–Thomson effect [81, 82]. Substituting the three-body rates[5] from Eq. (4.10) instead, one obtains a coefficient that depends on the condensate fraction,

$$\mathcal{P}(\eta) = \frac{9}{5}\frac{2-\eta^2}{6-9\eta^2+4\eta^3}\,. \tag{4.22}$$

We plot $\mathcal{P}(\eta)$ in Fig. 4.4, and see that it monotonically grows from $3/5$ at $\eta = 0$ to $9/5$ at $\eta = 1$. One can understand these limits in terms of the dominant processes in Fig. 4.3. In the $\eta \to 0$ limit, processes *iii* and *iv* dominate, which have the same combinatorial prefactors (grey disk areas) and $\Gamma_0 \approx \Gamma_{\rm th} \approx \Gamma$, as for the Joule–Thomson cooling. In the $\eta \to 1$ limit, processes

[4] This applies also to decoherence-driven cooling observed in [100, 101].

[5] Using two-body loss from, e.g., spin-exchange collisions, yields $\mathcal{P} = 6/(10-5\eta^2)$.

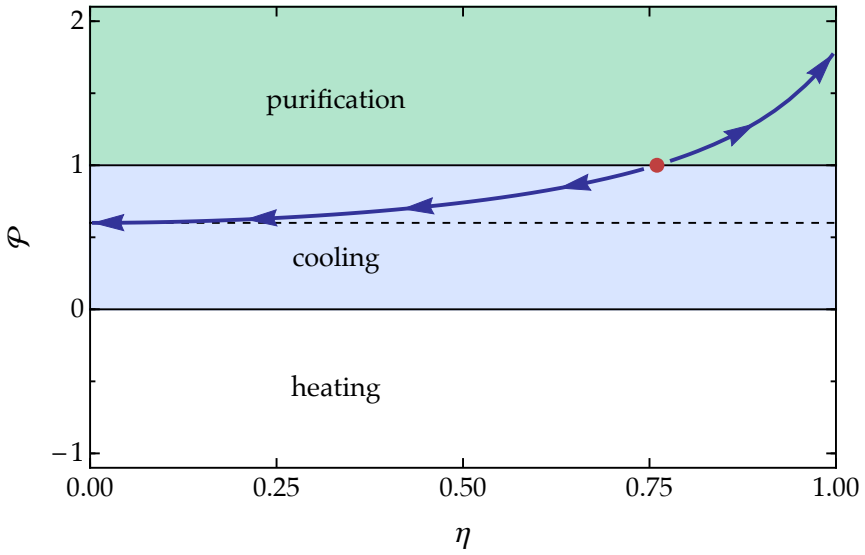

Figure 4.4 | **Ideal-gas theory of three-body cooling.** The purification coefficient $\mathcal{P}$ determines whether the gas purifies, or cools without purifying. Blue arrows show the direction of the evolution. For condensed fractions η above $\eta^* = 0.76$ (red point), $\mathcal{P} > 1$ and $\eta \to 1$. For $\eta < \eta^*$, $\mathcal{P} < 1$, and the condensate density decreases towards zero while the gas' temperature nevertheless decreases. The limit $\eta \to 0$ is formally equivalent to the one-body Joule–Thomson case, with $\mathcal{P} = 3/5$ (dashed line). Figure adapted from [17].

i and *ii* dominate, which have different combinatorial prefactors: now $\Gamma_{\text{th}} \approx 3\Gamma_0 \approx 3\Gamma$, and $\mathcal{P} \approx 9/5$.

The purification coefficient crosses the threshold for purification at $\mathcal{P} = 1$ for all condensed fractions above the critical value η^*, given by the roots of the cubic equation

$$5\eta^3 - 9\eta^2 + 3 = 0\,, \tag{4.23}$$

for which only $\eta^* \approx 0.7593$ falls within the domain of physical values $\eta \in [0, 1]$. Below this η^*, the condensed fraction falls to 0 in the long-time limit. Above it, $\eta \to 1$ and the cloud purifies.

Fig. 4.5 shows representative trajectories for the thermal fraction as a function of the fraction of remaining atoms. As seen in Eq. (4.19), $\mathcal{P} - 1$ sets the value of the slopes of these trajectories when plotted with log-log axes. The critical trajectory (red) maintains a constant $\eta = \eta^*$, separating the purifying (green) and cooling-only (blue) regions. Trajectories in the upper region (blue) show the condensate disappearing completely, i.e, $\eta \to 0$, with a finite fraction of atoms remaining. At this point, this gas is no longer saturated, and so our theory does not apply. One expects the temperature to continue to decrease beyond this point, but at a slower rate, with the three-body loss rate now independent of an atom's energy. The cooling then happens not due to bosonic bunching, but rather because at fixed E/N in a non-saturated Bose gas $\partial T/\partial\mu \geq 0$, and $\dot{\mu} \leq 0$ as the gas becomes less saturated [81, 82].

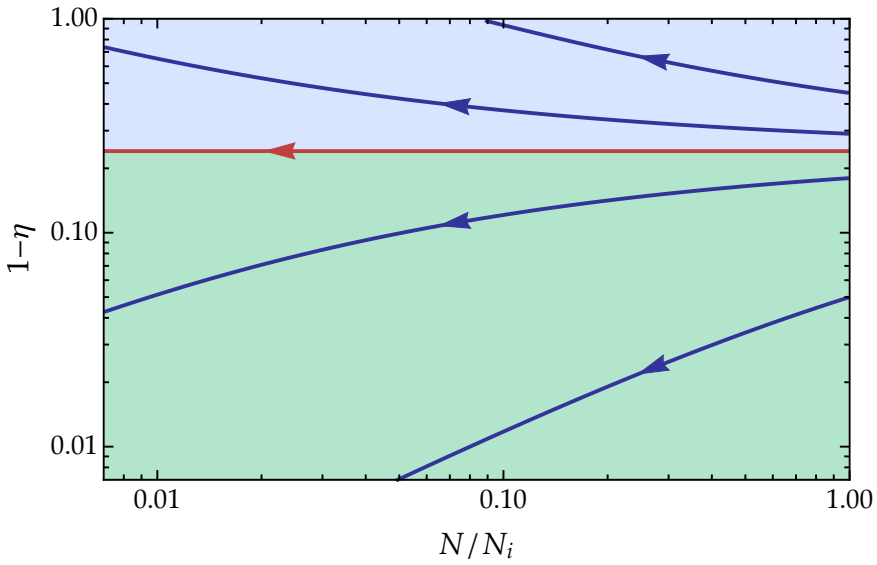

Figure 4.5 | **Evolution of thermal fraction under three-body loss.** Here we plot representative trajectories showing the change in thermal fraction, $1-\eta$, as atoms are lost from a cloud initially containing N_i atoms. Time runs from right to left in this plot (arrows). The red trajectory shows the critical $\eta^* \approx 0.76$ which remains constant under three-body loss. In the blue region, where $\eta < \eta^*$, the thermal fraction increases until the condensate vanishes completely. In the green region, where $\eta > \eta^*$, the condensed fraction increases over time to give a pure condensate as $N \to 0$. Figure adapted from [17].

4.4 Mean-field theory

In reality, of course, most ultracold Bose gases used in experiments do have interactions between particles; indeed they are necessary in order for the gas to be able to thermalise in the first place. We now include this interaction energy into our theory at the mean-field level, to quantify its impact on the cooling and purification dynamics. The ideal-gas effects should be dominant when the interaction energy is small compared to the thermal one. The interaction energy is given by

$$E_{\mathrm{int}} = \frac{g}{2V}(N_0^2 + 4N_0N_{\mathrm{th}} + 2N_{\mathrm{th}}^2)\,. \tag{4.24}$$

At small thermal fractions, the ratio of thermal to interaction energy is, to lowest order, then

$$\begin{aligned}\frac{E_{\mathrm{th}}}{E_{\mathrm{int}}} &= \frac{3}{2}\frac{\zeta(\frac{5}{2})}{[\zeta(\frac{3}{2})]^{5/3}}\frac{\bar{\eta}^{5/3}}{(na^3)^{1/3}} \\ &\approx 0.406 \cdot \frac{\bar{\eta}^{5/3}}{(na^3)^{1/3}}\,.\end{aligned} \tag{4.25}$$

The mean-field results are therefore expected to come into effect for values $(na^3)^{1/5} \approx \bar{\eta}$. We restrict ourselves to studying the regime $na^3 \lesssim 10^{-5}$, so that $g^{(3)}$ remains ideal-gas–like[6], and the saturation picture holds [39]. We also assume that the excitations are particle-like.

[6] At $na^3 = 10^{-5}$, $g^{(3)}$ for $\eta \approx 1$ has increased from its ideal-gas value by $\approx 11\,\%$ [97, 99].

The total energy is now the sum of Eqs. (4.12) and (4.24), which we write as

$$E = \left[\frac{g}{V}\left(\tfrac{1}{2}N_0 + N_{\text{th}}\right)\right] N_0 + \left[\frac{3}{2}\frac{\zeta(\frac{5}{2})}{\zeta(\frac{3}{2})}k_{\text{B}}T + \frac{g}{V}(N_0 + N_{\text{th}})\right] N_{\text{th}}\,, \tag{4.26}$$

and we interpret the terms in square brackets as the energy per condensate particle, ε_0 (left), and the energy per thermal particle, ε_{th} (right). For the system to remain in equilibrium as it evolves, the energy must satisfy both

$$\dot{E} = -\varepsilon_0\Gamma_0 N_0 - \varepsilon_{\text{th}}\Gamma_{\text{th}}N_{\text{th}}\,, \quad \text{and} \tag{4.27}$$

$$\dot{E} = \frac{\partial E}{\partial N_0}\left(-\Gamma_0 N_0 - \dot{N}_{\text{t}}\right) + \frac{\partial E}{\partial N_{\text{th}}}\left(-\Gamma_{\text{th}}N_{\text{th}} + \dot{N}_{\text{t}}\right)\,. \tag{4.28}$$

For the latter, one must be careful to first rewrite $T \propto N_{\text{th}}^{2/3}$ in Eq. (4.26). Solving using a similar procedure as in the previous section yields the mean-field solution for the purification coefficient,

$$\mathcal{P}_{\text{mf}} = \frac{9(2-\eta)^2 + b_1(\eta)(na^3)^{1/3}}{5(6-9\eta^2+4\eta^3) + b_2(\eta)(na^3)^{1/3}}\,, \quad \text{where} \tag{4.29a}$$

$$b_1(\eta) = \gamma(-12 + 12\eta + 12\eta^2 - 20\eta^3 + 7\eta^4)(1-\eta)^{-5/3}\,, \tag{4.29b}$$

$$b_2(\eta) = 2\gamma\eta(6 - 9\eta^2 + 4\eta^3)(1-\eta)^{-2/3}\,, \quad \text{and} \tag{4.29c}$$

$$\gamma = 2\frac{\zeta(\frac{3}{2})^{5/3}}{\zeta(\frac{5}{2})} \approx 7.39\,. \tag{4.29d}$$

We plot trajectories of the thermal fraction as a function of na^3 in Fig. 4.6. The red trajectory divides the plot into two separate basins of attraction; in the limit $na^3 \to 0$, it approaches the critical η^* from the ideal-gas theory (c.f. Fig. 4.5). Points below the red curve eventually lead to a pure condensate, whereas points above it eventually lead to a fully thermal cloud. As in Fig. 4.5, $\mathcal{P} - 1$ gives the slope of the trajectories when plotted on log-log axes. The background shading indicates whether the gas is instantaneously purifying (green, $\mathcal{P} > 1$), cooling without purifying (blue, $0 < \mathcal{P} < 1$), or heating ($\mathcal{P} < 0$).

At low thermal fractions, contours of constant $\mathcal{P}$ follow the scaling $\bar{\eta} \propto (na^3)^{1/5}$. Physically, these contours are a fixed ratio of thermal to interaction energy; mathematically they correspond to the factor $(1-\eta)^{-5/3}$ in the polynomial b_1 becoming large. Qualitatively, the cooling effect can then be thought of as a competition between cooling due to quantum statistics, and heating due to the repulsive interactions. The $\mathcal{P} = 0$ contour, which separates the heating and cooling regions of the phase diagram, corresponds to $\bar{\eta} \approx (na^3)^{1/5}$, for which the ratio of thermal to interaction energy is ≈ 0.4, as we showed in Eq. (4.25). We find that the purification is less robust when we account for the mean-field interaction energy, but the effect nevertheless persists up to interaction strengths $na^3 \approx 10^{-7}$. The dashed line in Fig. 4.6 corresponds to $gn = \frac{1}{2}k_{\text{B}}T$. Below it, a significant fraction of the excitations are phononic, rather than particle-like, and our theory does not apply. Cooling in the phononic regime has, however, been studied in [86, 87].

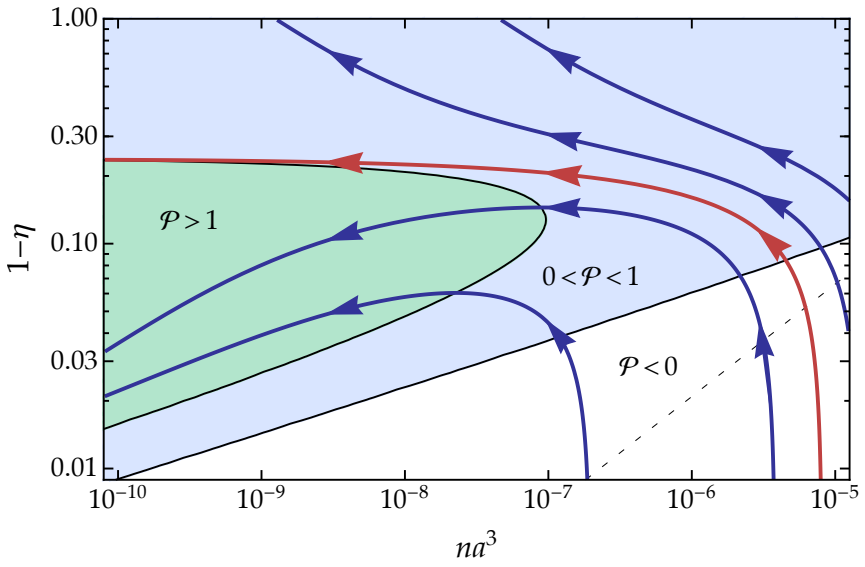

Figure 4.6 | **Three-body cooling in a weakly interacting Bose gas.** In the interacting theory, the purification coefficient $\mathcal{P}$ depends on both the condensed fraction η and the gas parameter na^3. The critical point from the ideal-gas theory is now a critical trajectory (red) separating the parameter space into two basins of attraction, ultimately leading to either purely thermal, or purely condensed clouds. The log derivative is given by $\mathcal{P}-1$, and the background shading indicates whether the gas instantaneously heats (white), cools (blue), or purifies (green). The dashed line corresponds to $gn = \frac{1}{2}k_{\mathrm{B}}T$, below which we expect our theory to break down due to the phononic, rather than particle-like, nature of excitations. Figure adapted from [17].

4.5 Experimental feasibility

Identifying a suitable platform for studying these dynamics experimentally requires careful consideration of several (coupled) parameters, including:

- K_3, the three-body loss coefficient,
- the mean free path between collisions, $\propto (na^2)^{-1}$,
- the two-body scattering rate, $\propto (na^2)/\sqrt{m}$, and
- the healing length, $\propto (na)^{-1/2}$.

The scalings of the mean free path, scattering rate, and healing length collectively favour high n, low a, and the use of an atom with small mass m. This could be achieved by working near a zero-crossing of a associated with a Feshbach resonance, where the K_3 coefficient is almost independent of a.

As an example, $K_3 \approx 10^{-29}\,\mathrm{cm}^6\,\mathrm{s}^{-1}$ has been measured near the zero-crossings of Feshbach resonances in both ^{7}Li [102] and ^{39}K [103]. Taking $a = 10\,a_0$, an initial $n = 10^{14}\,\mathrm{cm}^{-3}$, and $\eta = 0.9$, we calculate $na^3 = 1.5\times10^{-8}$, for which our theory predicts $\mathcal{P}_{\mathrm{mf}} > 1$. This combination gives $\Gamma_{3\mathrm{B}} \approx 0.1\,\mathrm{s}^{-1}$, which is sufficiently large to dominate over the one-body loss rate, which in many experiments $< 0.01\,\mathrm{s}^{-1}$. The mean free path $\ell = (8\pi na^2)^{-1} \approx 1\,\mathrm{mm}$, and the

healing length $\xi = 1/\sqrt{8\pi n_0 a} \approx 1\,\mu\text{m}$. This would mean that in a box trap of side length $L \gtrsim 10\,\mu\text{m}$, which is $\ll \ell$, secondary collisions of the loss products would be negligible, and since $L \gg \xi$, the gas would be homogenous. Ref. [104] argues that a suitable condition for ensuring continuous thermalisation is $\Gamma_2 > 3\dot{T}/T$, with $\Gamma_2 \approx 8\pi n a^2 \cdot \bar{\eta}\sqrt{8k_\text{B}T/(\pi m)}$. In our saturated homogeneous gas, $\dot{T}/T = \frac{2}{5}\Gamma_\text{th} = \frac{2}{3}\mathcal{P}\Gamma_\text{3B} \approx \Gamma_\text{3B}$. This would comfortably satisfy the continuous-thermalisation condition for ^{7}Li, and marginally in the case of ^{39}K. Our proposed initial n, while ambitious, is within an order of magnitude of densities currently realisable in box traps. The temperatures corresponding to these initial values of n and η, $\approx 200\,\text{nK}$ and $\approx 1\,\mu\text{K}$ for ^{39}K and ^{7}Li respectively, are also reasonably accessible. The thermal and condensed component densities could be determined by using momentum-resolved techniques, e.g., as outlined in appendix B.

4.6 Conclusion

We've developed a theory showing that under realistic experimental conditions, a partially condensed homogeneous Bose gas can purify under the action of three-body loss. The main cooling effect is a statistical one, relying only on the saturation of the gas, and is enhanced by the higher loss rate of thermal atoms relative to condensate ones due to bosonic bunching. Including mean-field effects gives a dynamical phase diagram which shows qualitative changes in the behaviour for small changes in the initial conditions. In the future, it would be interesting to investigate this effect in either a more strongly interacting gas, or to fully develop the theory for very low thermal fractions. This requires accounting for the phononic nature of interactions, and would connect our work with the analysis in Refs. [86, 87].

5 Critical dynamics of a Bose gas

As we discussed in chapter 2, at sufficiently high phase-space densities, the Bose gas undergoes a phase transition and a Bose–Einstein condensate forms. It is well established, both theoretically and experimentally, that spatial correlations within the (near-)equilibrium gas exhibit universality in the vicinity of this continuous second-order phase transition. In this chapter, we explore a natural extension of this paradigm in our study of the far-from-equilibrium dynamics of an isolated quench-cooled Bose gas as it undergoes Bose–Einstein condensation.

We will begin with a brief outline of the physics of critical dynamics in equilibrium systems near second-order phase transitions in section 5.1. We then turn to the analogous far-from-equilibrium dynamics, which we discuss in section 5.2 in the context of non-thermal fixed points. In section 5.3, we present our experimental observation of bidirectional dynamic scaling, a hallmark of the non-thermal–fixed–point paradigm, in an isolated 3D Bose gas far from equilibrium. Finally, in section 5.4 we connect our work to the foundational problem of the formation of a BEC by studying the properties of the (quasi)condensate that forms while the system is thermalising. The results presented in these latter two sections appear in [18].

5.1 Critical phenomena in near-equilibrium systems

One of the great successes of modern physics was the realisation that seemingly disparate physical systems are actually fundamentally alike. This has led to the classification of (near-)equilibrium systems into universality classes [105, 106] based on their behaviour near second-order phase transitions. The key to this classification is the universality seen in the spatial correlations of these systems as they approach the transitions. In this section, we evaluate the first-order spatial correlation function, $g^{(1)}$, for a homogeneous Bose gas. We will then briefly describe the key features of both the scaling hypothesis and a model for the dynamics of the correlations known as the Kibble–Zurek mechanism; these concepts are to be compared with their far-from-equilibrium counterparts in section 5.2. An in-depth theoretical treatment of the topics covered in this section can be found in several texts, e.g., [38, 106].

5.1.1 First-order correlation function in a homogeneous Bose gas

We consider a homogeneous Bose gas prepared in equilibrium with a temperature T that is initially above the critical temperature for condensation, T_c. We now begin to slowly decrease

T, e.g., via evaporative methods. Here it is important that the per-atom removal rate of high-energy atoms is slower than the typical equilibration timescale, so that the system remains close to equilibrium at all times.

Let us now evaluate the first-order correlation function (see section 2.9) and examine its properties as the gas approaches the transition temperature. At temperatures far above T_c, the Bose distribution $n_k(\mathbf{k})$ [Eq. (2.16)] is approximately gaussian, with width $\sigma = \sqrt{mk_BT/\hbar^2} = \sqrt{2\pi}\,\lambda_T^{-1}$. Since the correlation function is proportional to the Fourier transform of the momentum distribution [Eq. (2.66)], $g^{(1)}(r)$ is also gaussian in this regime, and shows short-range correlations up to the lengthscale $\lambda_T/\sqrt{2\pi}$. As the temperature begins to decrease, λ_T increases and correlations begin to spread throughout the system. Near T_c, the Bose distribution is approximately

$$n_k(\mathbf{k}) \approx \frac{V}{(2\pi)^3}\frac{k_BT}{\hbar^2k^2/(2m)-\mu}\,, \tag{5.1}$$

for $k\lambda_T \lesssim 1$ and $|\mu| \ll k_BT$ such that the correlation function is approximately [38,39]

$$g^{(1)}(r) \propto \frac{\exp(-r/\ell_c)}{r}\,, \tag{5.2}$$

for $r \gtrsim \lambda_T$, and the correlation length $\ell_c = \lambda_T\sqrt{k_BT/(4\pi|\mu|)}$. One sees that the correlations now extend far beyond λ_T. Moreover, for $|\mu| \ll k_BT_c$ and at fixed volume, $|\mu| \sim |T-T_c|^2$, and so we have

$$\ell_c \propto |T-T_c|^{-1}\,. \tag{5.3}$$

Close to the transition, we see that the gas now displays long-range, *scale-free* correlations, i.e., $g^{(1)} \propto 1/r$, since ℓ_c diverges near the critical point.

The algebraic divergence of ℓ_c near a second-order phase transition is a feature common to many different systems. The important physics is captured by the scaling of ℓ_c, which is in general $|T-T_c|^{-\nu}$, where ν is known as the static critical exponent. For the BEC transition in the ideal Bose gas, we identify $\nu = 1$. It can be shown that the introduction of weak interatomic interactions reduces the predicted correlation-length critical exponent to $\nu \simeq 0.67$ [107,108], which has also been verified experimentally [109,110].

5.1.2 The scaling hypothesis

The scaling hypothesis assumes that near the phase transition, the rapidly diverging ℓ_c is the only relevant length in the problem, and that it is therefore the natural unit for all quantities that have dimensions of length. Using a renormalisation-group approach [105,111], the correlations look self-similar under this prescription: near the transition, $g^{(1)}$ takes the form [38]

$$g^{(1)}(r) \to |r|^{-\Omega}C(r/\ell_c)\,, \tag{5.4}$$

where a universal exponent Ω and a universal function C are sufficient to fully characterise the correlations. In general, both Ω and C are insensitive to the microscopic details of a system, and depend instead only on macroscopic properties of the system such as the dimensionality, and the dispersion relation. Then, regardless of the microscopic details, systems which have the same universal function C and exponent Ω display identical behaviour near their transitions. This allows us to group them together into a broad universality class [105, 106] labelled by the shared universal properties $\{C, \Omega\}$. For example, the BEC transition in a three-dimensional weakly interacting gas (with $\nu \simeq 0.67$ as in the previous section) belongs to the same universality class as the three-dimensional XY model for magnets [107–110].

In the limit that $\ell_c \to \infty$ (or potentially also $\ell_c \to 0$), $g^{(1)}$ takes on a purely algebraic form, with no reference to a natural lengthscale. This completely scale-invariant scenario corresponds to a fixed point of the renormalisation-group flow.

5.1.3 Dynamics and the Kibble–Zurek mechanism

The scaling behaviour can be naturally extended to capture the dynamics of a system that is quenched across the phase transition. When T crosses T_c, a condensate begins to form and the condensing atoms must spontaneously adopt a phase; this breaks a 1D-unitary-group, or $U(1)$, symmetry. We must correspondingly keep track of the ensemble-averaged condensate wavefunction in order to account for the reduced symmetry. In a general system, a parameter that must be introduced like this is known as an *order parameter*. On the one hand, for a fully adiabatic quench, long-range correlations would ensure that the choice of the symmetry-breaking order parameter is the same for all points in the field at the moment the symmetry is broken. The Kibble–Zurek mechanism [112, 113], on the other hand, provides an elegant framework for understanding the dynamics as we begin to vary the system a little more quickly. A comprehensive review of theoretical and experimental work on the Kibble–Zurek mechanism is available in [114, 115]; here we merely outline the main features.

The key point to consider here is that it takes time for information to propagate within the system, and so spatial correlations cannot form instantaneously. We saw earlier in this section that the divergence of $\ell_c \propto |T - T_c|^{-\nu}$ is captured by the *static* critical exponent ν. The time τ needed to establish these correlations is characterised by a complementary exponent known as the *dynamical* critical exponent $z > 0$, as $\tau \propto \ell_c^z$. Now, if T is varied to cross T_c at a non-zero rate, there will be a point in time during the quench at which the system cannot establish the correlations sufficiently quickly to adiabatically follow. At this time, the system "freezes" into finite-size domains that each subsequently select independent values of the order parameter.

For a linear quench of T/T_c at a rate $1/\tau_Q$, the average domain size ℓ follows a universal scaling

$$\ell = \lambda_0(\tau_Q/\tau_0)^b \qquad \text{with} \qquad b = \nu/(1+\nu z)\,, \tag{5.5}$$

where λ_0 and τ_0 are microscopic length- and timescales characteristic of the specific system. The dynamic critical exponent for the weakly interacting homogeneous Bose gas, $b = 0.35(4)$, was measured in [116], and is consistent with the previously measured $\nu \simeq 0.67$ [107, 108] and the expected $z = 3/2$.

The formation of domains, and the corresponding boundaries between them, typically produces topological defects within the system (e.g, [12, 115, 117]). In the case of the Bose gas, windings of the complex phase at domain boundaries results in the production of vortices, or tangles of vortex lines, with an initial density that is determined by ℓ. The dynamics of these vortices are significant for the subsequent relaxation of the gas to equilibrium [118].

5.2 Universal dynamics in far-from-equilibrium systems

In the previous section, we considered a system undergoing a phase transition, and which remains close to its instantaneous equilibrium throughout the dynamics. In this section, we turn to the open question of the behaviour of systems that are far from equilibrium.

To begin, we will consider the system's instantaneous quantum state as a point in an abstract parameter space. The reader could imagine this point being described, e.g., by a coordinate vector comprising the values of the lowest-order correlation functions at a selection of positions in the gas. The time-dependent correlations in the gas then describe a path through the parameter space. Let us then consider how our system could proceed from some far-from-equilibrium initial condition to a corresponding thermal equilibrium. We sketch two possible scenarios in Fig. 5.1. Firstly, one might reasonably expect that if the state were close to a new equilibrium, the system would relax directly to it. Such thermal equilibria are the stable attractors of the parameter space; if the system is slightly displaced from one, it will spontaneously return back to that same equilibrium. A system initially prepared far away from equilibrium may, however, instead explore other regions of the parameter space as it relaxes. For example,

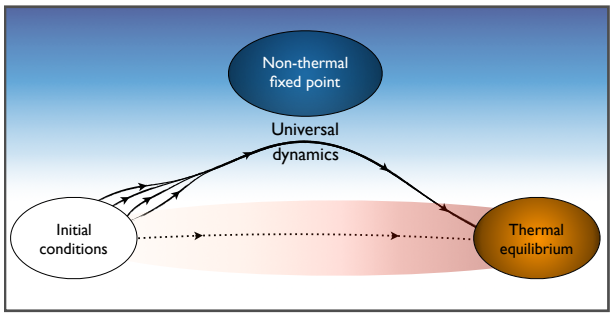

Figure 5.1 | **Pathways to equilibrium** for a system prepared in different non-equilibrium initial states. If the initial state is close to equilibrium, the system relaxes directly (dashed, red). If, instead, it is far from equilibrium, the system may pass by a non-thermal fixed point and display universal dynamics. Figure adapted from [119].

there may exist additional stationary points that do not possess the same stability features as thermal equilibria. Of particular interest for us are the possible saddle points, which act as attractors along some directions in the parameter space, but are instead unstable along other directions.

5.2.1 Non-thermal fixed points

Recent theoretical work [120–131] proposes that the non-equilibrium parameter space does indeed feature saddle points like those described above; they are referred to in the literature as non-thermal fixed points (NTFPs). These NTFPs are the far-from-equilibrium, dynamic analogue of the renormalisation-group fixed points introduced in section 5.1.2 [128]. NTFPs are believed to exhibit many features that are reminiscent of the critical points of near-equilibrium phase transitions: the dynamics in the vicinity of NTFPs are predicted to be critically slowed, insensitive to the details of the initial state preparation, and able to be described in terms of a universal dynamical scaling hypothesis. This may lead to a future system for the classification of systems into new, far-from-equilibrium universality classes. References [126, 128] provide a comprehensive overview of the theoretical work to date.

One particular scenario that has been the subject of extensive theoretical study in the context of NTFPs is the process of BEC formation in an isolated system following a rapid cooling quench. We consider here a Bose gas that is initially prepared in equilibrium at a temperature close to, but slightly above, the critical temperature for condensation. The cooling quench corresponds to the sudden removal of all particles with energy above some cutoff; in contrast to the near-equilibrium case, here the timescale for particle removal is much faster than any process that acts to restore the system to thermal equilibrium. Following such a quench, energy and particle conservation in the closed system imply that a bidirectional redistribution of particles will take place in momentum space, i.e., the majority of particles are transported toward lower momenta (infrared, IR) where a condensate forms, while a small number of particles carry the energy towards higher-momentum states (ultraviolet, UV).

The dynamical scaling hypothesis

NTFP theories predict that if the state resulting from the quench is sufficiently far from equilibrium, the system may approach an NTFP, where the dynamics are then universal and exhibit scaling of the correlation functions similar to Eq. (5.4). Unlike the purely spatial scaling seen near equilibrium critical points, however, in this case the scaling is spatiotemporal. Letting t denote the time since the quench, the momentum distribution is predicted to scale, within a

certain range of momenta, as

$$n_k(t, \mathbf{k}) = \tilde{t}^{\alpha}\, n_k(t_0, \tilde{t}^{\beta}\mathbf{k})\,. \tag{5.6}$$

Here we have introduced a reference time t_0, $\tilde{t} = t/t_0$, and α and β are the scaling exponents. We note that this scaling takes the same form as the Family–Vicsek scaling in classical surface growth [132, 133].

Eq. (5.6) is equivalent to a scaling of the correlation function, since the momentum distribution is its Fourier transform [Eq. (2.66)]. Under the dynamical scaling hypothesis, knowing α, β, and the momentum distribution at time t_0 is sufficient to fully characterise the dynamics. In direct analogy with the (static) scaling hypothesis from section 5.1.2, these three quantities are the labels of a non-equilibrium universality class that is associated with the NTFP.

Conservation laws

Global conservation laws, such as for the total atom number and energy, constrain the scaling exponents [126, 128]. That is to say, α and β are not independent of one another, but are instead related via the conserved quantities. For example, using Eq. (5.6), the total atom number in a d-dimensional system is given by

$$N(\tilde{t}) = \int \mathrm{d}^d\mathbf{k}\, \tilde{t}^{\alpha}\, n_k(t_0, \tilde{t}^{\beta}\mathbf{k}) \tag{5.7a}$$

$$= \tilde{t}^{\alpha-\beta d} \int \mathrm{d}^d\mathbf{k}'\, n_k(t_0, \mathbf{k}')\,, \tag{5.7b}$$

where we have substituted $\mathbf{k}' = \tilde{t}^{\beta}\mathbf{k}$. Since a conserved N cannot depend on $\tilde{t}$, a particle-conserving transport must satisfy $\alpha = d\beta$. A similar calculation shows that, for a system with quadratic (free-particle) dispersion, energy conservation demands $\alpha = (d+2)\beta$.

In the closed-system dynamics we are considering here, both number and energy are simultaneously conserved. At first glance, this seems to present a rather serious issue: the two constraints of these laws are only satisfied for $\alpha = \beta = 0$, for which by definition there are no dynamics whatsoever. The solution to this dilemma is to divide the dynamics into two separate momentum ranges, namely the IR and the UV. This *bidirectional* scaling is then characterised by two sets of scaling exponents, with distinct values for the particle-transport dynamics in the IR and for the energy-transport dynamics in the UV, i.e., we have a total of four distinct exponents: $(\alpha_{\mathrm{IR}}, \beta_{\mathrm{IR}}, \alpha_{\mathrm{UV}}, \beta_{\mathrm{UV}})$. Considering Eq. (5.6) in conjunction with the conservation-law constraints, one can see that both α and β are positive for flows into the IR, and both are negative for flows into the UV[1]. The n_k curves could then, separately in the IR and UV, be collapsed onto universal ones.

[1] References [134–136] describe an alternative accelerated-wavefront scaling hypothesis in which $\tilde{t} \propto (t_* - t)$, where t_* is the time at which the wavefront reaches either $k = 0$, or $k = \infty$. Under this prescription, positive (negative) scaling exponents correspond to flow into the UV (IR).

Connection to turbulence

The scaling behaviour associated with NTFPs is reminiscent of the self-similar turbulent cascades [134, 137–139], and the two are indeed closely related. We note, however, that turbulent cascades generally involve external driving and dissipation forces, and studies have traditionally focussed on the determination of the Kolmogorov–Zakharov exponents that characterise the power-law dependence of the steady-state momentum distribution on $|\mathbf{k}|$, i.e., $n_k \sim |\mathbf{k}|^{-\gamma}$. On the other hand, when studying quench-cooled gases in the context of NTFPs, the isolated system does not have external driving or dissipation forces, and the momentum distribution has not yet reached its steady state.

The NTFP dynamics following a vigorous cooling quench are associated with the gas entering an intermediate stage of strong turbulence [140, 141], where coherences between different k modes significantly influence the evolution. This regime is associated with the formation of coherent structures such as vortex tangles and loops [136, 142], and the system generally displays strong phase fluctuations. This is to be compared with the vortex nucleation associated with domain boundaries in our earlier discussion of the Kibble–Zurek mechanism. Analogously to the phase-fluctuating equilibrium regimes of low-dimensional Bose systems, this regime is often referred to as a nonequilibrium quasicondensate. A fully coherent BEC then forms as the quasicondensate relaxes.

Numerical and experimental evidence

Scaling of the form in Eq. (5.6) has been predicted to occur in diverse contexts including quantum magnets [129], the quark-gluon plasma [124, 125, 130], and ultracold atomic gases [124–127]. Numerical studies [122, 123, 143–145] of both single- and two-component Bose gases have provided significant evidence in support of these theories; however, until recently, experimental support has been limited. The authors of [119, 146] reported the first observation of NTFP-like self-similar scaling in the infrared dynamics of one-dimensional Bose gases. In [119], Prüfer et al. observed universal dynamics in the spin correlations of a quasi-1D spinor BEC of ^{87}Rb, finding scaling exponents $\alpha = 0.33(8)$ and $\beta = 0.54(6)$ in the IR. Erne et al. [146] reported their measurements of the momentum distribution of a harmonically confined gas of ^{87}Rb that was shock cooled from the 3D into the 1D regime. They observe scaling in the IR dynamics of the momentum distribution, with exponents $\alpha \approx \beta \approx 0.1$. Our experiments presented in section 5.3 reveal spatiotemporal scaling in both the IR and UV, studied in the textbook context of a homogeneous 3D Bose gas.

5.2.2 Bose condensation far from equilibrium

The strong-quench–cooling protocols we have been discussing have a great deal of overlap with a foundational problem in the context of ultracold atoms: the process of how a Bose–Einstein condensate forms. Obtaining a general understanding of this dynamical process, including in far-from-equilibrium scenarios, has proven challenging [134–136, 147–154], and several aspects of the problem still remain open [114, 141]. A particularly important question that has led to intense discussion in the literature is what determines the timescale for condensate formation in a closed system. Here, we consider two options, either of which could prove to be dominant, depending on the prevailing experimental conditions.

An early theoretical study [147] took an approach based on kinetic theory, and predicted that the equilibration of a Bose gas would take place on a timescale on the order of three to four kinetic collision times, $\tau_{\mathrm{kin}} = (n\sigma v_T)^{-1} \propto a^{-2}$, where the mean thermal velocity $v_T = \sqrt{3k_{\mathrm{B}}T/m}$ and a is the scattering length. It was later shown [134–136, 149, 150] that this kinetic-theory approach can also be used to describe the transport of particles in momentum space towards lower energies. This approach, however, is unable to describe the development of a macroscopic occupation of the zero-momentum (BEC) mode in the absence of seeding or similar modifications [141]. Including many-body corrections to the two-body scattering rates at low momenta [148] goes part of the way towards addressing this problem, however all of the studies mentioned here neglect the effects of coherence between momentum states.

Once phase correlations between low-energy modes become significant, it is more appropriate to describe the system in terms of an emergent classical field [155]. In practice, this means that the evolution can be described via a wavefunction obeying the GPE [Eq. (2.51)]. In this case, the dynamics take place on the coherent timescale $\tau_{\mathrm{coh}} = \hbar/\mu \propto a^{-1}$. This approach connects to the strong-turbulence picture described in the previous section: it captures the formation of an out-of-equilibrium quasicondensate initially riddled with coherent excitations such as vortex loops [136, 142] or domain walls [116], and the subsequent relaxation of the quasicondensate to equilibrium.

5.3 Bidirectional dynamic scaling

5.3.1 Experimental protocol

In this section, we describe our experimental protocol for studying the far-from-equilibrium dynamics of an isolated Bose gas. The basic idea is depicted in Fig. 5.2. We start with an equilibrium homogeneous gas of $N \approx 1.2 \times 10^5$ atoms, confined in our cylindrical box trap. We set the trap diameter to $D \approx 27\,\mu\mathrm{m}$, the length to $L \approx 46\,\mu\mathrm{m}$, and the depth is $U_{\mathrm{D}} \approx k_{\mathrm{B}} \times 1\,\mu\mathrm{K}$.

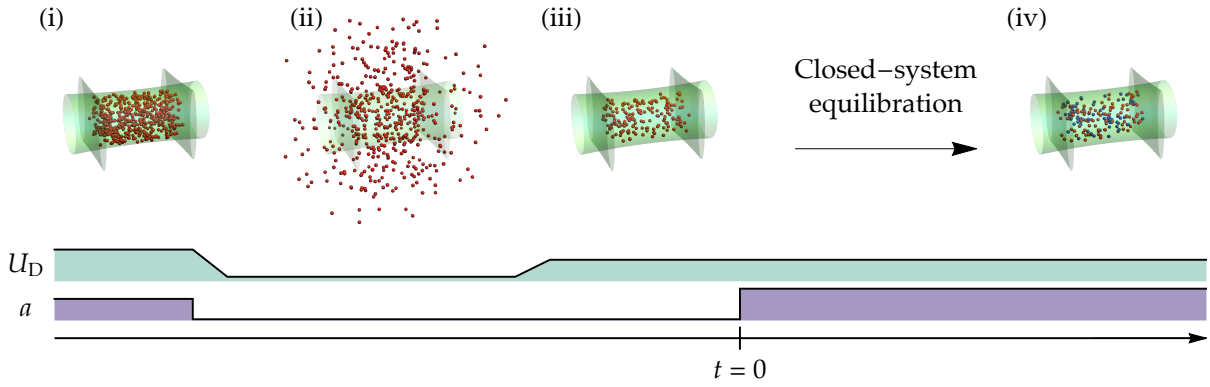

Figure 5.2 | Overview of experimental protocol. U_D denotes the depth of the optical box trap (green), and a is the s-wave scattering length. (i) We prepare a fully thermal cloud of $N \approx 1.2 \times 10^5$ atoms in equilibrium at $T \approx 130\,\mathrm{nK}$. (ii) We set $a \to 0$ using the Feshbach resonance, lower U_D, and allow high-energy atoms to escape the trap. The remaining atoms cannot thermalise with one another while $a = 0$. (iii) U_D is raised again to close the system, and the dynamics are then initiated, defining our time origin, $t = 0$, by tuning a to a positive value. (iv) Equilibrium state with both thermal (red) and condensed (blue) components. Figure adapted from [18].

The gas is prepared at a scattering length $a = 200\,a_0$, and the initial temperature $T \approx 130\,\mathrm{nK}$ is just above the condensation temperature T_c, such that no condensate is present.

We create a far-from-equilibrium initial condition by realising a quench of the form described in section 5.2.1. Our quench removes 77 % of the atoms and 97.5 % of the total energy E, so the energy per particle decreases by an order of magnitude; in equilibrium, the gas would then be (partially) condensed. We exploit the tuneability of the scattering length in order to completely separate this quench (in time) from the subsequent equilibration. First, we switch off the interactions by tuning $a \to 0$, and then lower U_D to $k_B \times 30\,\mathrm{nK}$ over 10 ms. A subsequent 2-s wait time at both $a = 0$ and this low U_D allows high-energy atoms, which have $\hbar^2 k^2/(2m) \gtrsim U_D$, to escape[2] without the remaining ones thermalising, and results in a far-from-equilibrium n_k. We then close the system by raising U_D, and start the clock for thermalisation by tuning a to some non-zero value; in the experiments described in this chapter, we use $100\,a_0 \leq a \leq 800\,a_0$.

Measuring the momentum distribution

To probe the state of the gas after a variable relaxation time t, we turn off both the trap and the interactions, allow the cloud to expand for a time of flight t_{ToF}, and then take an absorption image of the expanded cloud. We emphasise that we turn off interactions before expanding the cloud so that the expansion is ballistic, i.e., kinetic-energy dominated. The density distribution of atoms in these images therefore corresponds to the gas' momentum distribution, convolved

[2] The 2-s wait time allows atoms to leave both the trap and the experimental field of view.

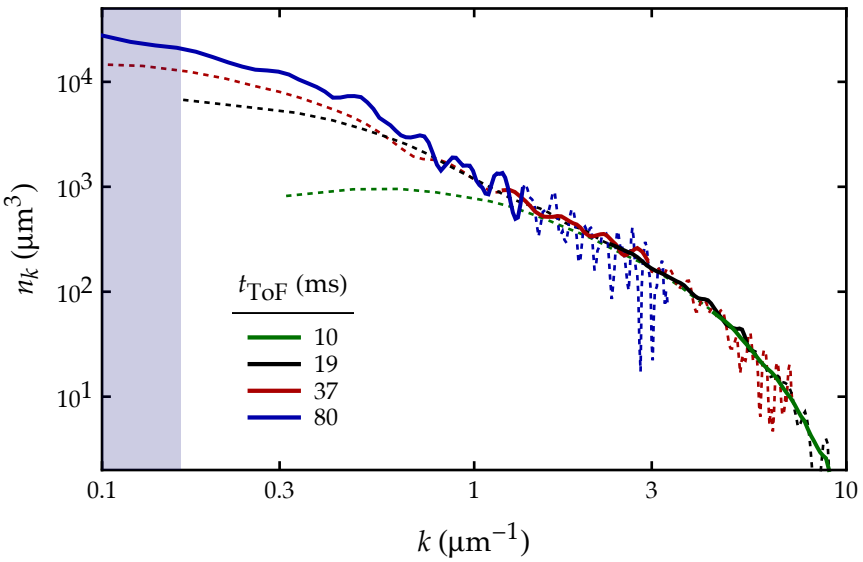

Figure 5.3 | **Measuring the momentum distribution.** These data correspond to the pre-quench thermal distribution, with $T \approx 130\,\mathrm{nK}$ and $N \approx 1.2 \times 10^5$. The distribution is inferred from images taken after a period t_{ToF} of ballistic expansion in time of flight; the 3D n_k is reconstructed from its 2D counterpart using the inverse-Abel transform. To determine n_k faithfully over a wide range of k, and with minimal noise, we combine data that use different times of flight. Dashed lines show the full distributions for single times of flight, plotted on log-log axes. We retain the data in the region where different-t_{ToF} curves are both empirically consistent with one another (solid lines), and still have reasonable signal-to-noise ratio. This corresponds to real-space distances on the image between 3 and 10 box diameters from the centre of the trap; we retain data to lower k for our longest $t_{\mathrm{ToF}} = 80\,\mathrm{ms}$. For this t_{ToF}, the shaded region indicates momenta for which $2\hbar k t_{\mathrm{ToF}}/m < L$ and finite-size effects dominate.

with the in-situ coordinate-space density, and finally integrated once along the line of sight; in this case, our imaging axis coincides with the cylinder's axis of symmetry, and the distributions are azimuthally symmetric.

In Fig. 5.3 we present an example distribution extracted from the images, plotted on log-log axes. We infer the momentum distribution from the images by assuming the mapping $\hbar k_{2\mathrm{D}} = mr/t_{\mathrm{ToF}}$, where r is the distance on the image to the cylinder's axis. This mapping accurately describes the true momentum distribution provided that $2\hbar k_{2\mathrm{D}} t_{\mathrm{ToF}}/m \gg \{D, L\}$, i.e., the distance travelled by the atoms during the expansion is large relative to the trap dimensions. We construct the radial momentum distribution by averaging the images azimuthally, then reconstruct the 3D n_k using the inverse-Abel transform[3] [Appendix C]. Finally, we combine data taken with various t_{ToF} in the range [10 ms, 80 ms]; the longest t_{ToF} allows us to access smaller k without finite-size effects dominating, while shorter ones give better signal-to-noise at large k. The shaded region in Fig. 5.3 indicates the finite-size–contaminated region for our longest t_{ToF}. Using this method, we measure reliable n_k values that vary over 5 orders of magnitude.

[3] This assumes spherical symmetry, and in the data presented in this chapter we treat n_k as dependent only on $k = |\mathbf{k}|$.

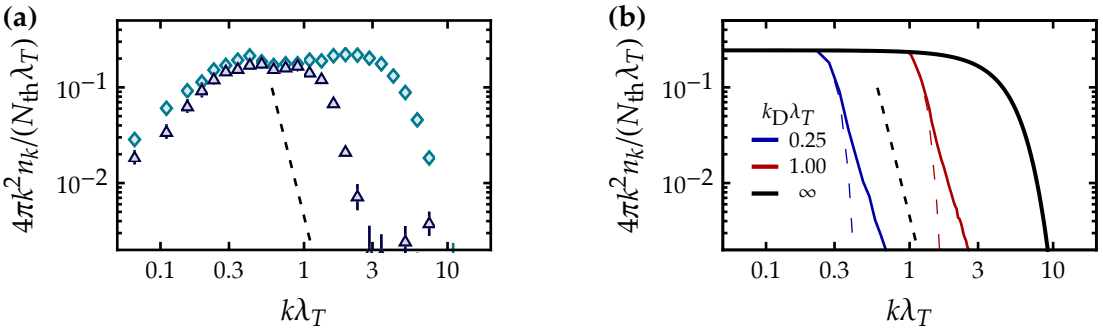

Figure 5.4 | **Momentum distribution after the quench.** In both panels, the dotted black line corresponds to $n_k \propto k^{-8}$. **(a)** Experimental spectral particle densities on log-log axes for the initial thermal cloud (cyan) and far-from-equilibrium cloud (dark blue) produced by the cooling quench. The lower values of $4\pi k^2 n_k$ for $k \lesssim 0.2\,\mu\text{m}^{-1}$ are due to the pre-quench cloud temperature being slightly above T_c. For comparison with the simulated data, experimental distributions are scaled by the number of atoms in the original thermal cloud, $N_{\rm th} = 1.2 \times 10^5$, and $\lambda_T = 0.78\,\mu\text{m}$. **(b)** Monte–Carlo simulations for the momentum distribution after the quench. Solid lines show the expectation for a cylindrical trap [as in **(a)**], whereas the dashed lines show the steeper cut expected for a cubic geometry.

Characterising the post-quench distribution

In Fig. 5.4(a), we plot the momentum distribution that results from the cooling quench. Here we use the spectral population density $\mathcal{N}_k = 4\pi k^2 n_k$ to better highlight the k-range from which the quench has removed atoms. One sees that momenta $k \lesssim 2\,\mu\text{m}^{-1}$ (corresponding to our $U_{\rm D} = k_{\rm B} \times 30\,\text{nK}$) remain relatively unchanged as a result of the quench, whereas the higher-momentum atoms have been removed. This quench does not produce a perfectly sharp cut in k, but rather one sees that the distribution falls off as approximately $n_k \sim k^{-8}$ for $k \gtrsim 2\,\mu\text{m}^{-1}$. This is because $U_{\rm D}$ determines the maximum value of only the components of an atom's momentum perpendicular to each of the trap walls, and not its total momentum, so in the absence of collisions some atoms with energy exceeding $U_{\rm D}$ remain in the trap.

Fig. 5.4(b) shows the expected distributions based on a model of non-interacting classical particles in a cylindrical box. These curves are obtained using Monte–Carlo sampling within the joint phase space of position and momentum. The momentum k is sampled from the Bose distribution, and its orientation is specified in spherical coordinates by the polar angle θ and azimuthal angle φ_k. The distance r of the particle from the axis and its azimuthal angle φ_r are also randomly assigned. This gives components of the momentum along the cylinder's axis of symmetry and in the perpendicular plane of $k_z = k\cos\theta$ and $k_\perp = k\sin\theta$ respectively. Considering the in-plane

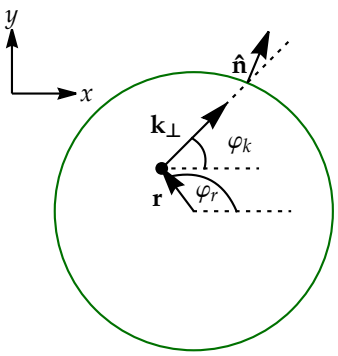

Figure 5.5 | **Classical particle in a cylindrical box trap.**

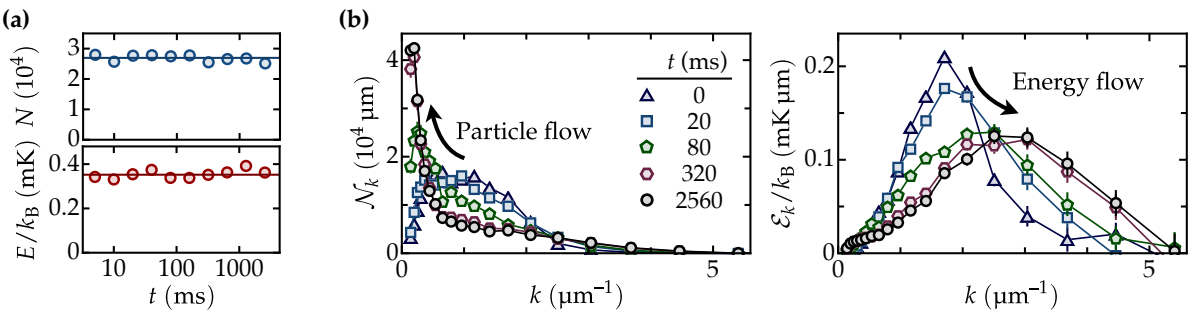

Figure 5.6 | **Bidirectional thermalisation in an isolated gas.** These data are for thermalisation using $a = 300\,a_0$. **(a)** The total atom number N and energy E are conserved during the dynamics. **(b)** Evolution of the spectral distributions of particles, $\mathcal{N}_k$, and energy, $\mathcal{E}_k$, showing net particle flow into the infrared and energy flow into the ultraviolet. Figure adapted from [18].

geometry shown in Fig. 5.5, one finds that at point where the particle reaches the trap wall, the component of its momentum perpendicular to the trap wall is given by

$$k_p = \mathbf{k}_\perp \cdot \hat{\mathbf{n}} = k \sin\theta \sqrt{1 - (2r/D)^2 \sin^2(\varphi_k - \varphi_r)}\,. \tag{5.8}$$

The quench therefore corresponds to retaining particles that satisfy both $\hbar^2 k_z^2/(2m) < U_D$, and $\hbar^2 k_p^2/(2m) < U_D$.

We note that in principle, an atom located at $r = D/2$ would always be retained in the quench if its momentum is tangential to the surface, regardless of the magnitude of k. This results in a small, but non-zero, population of very-high–k atoms being retained in the quench. In contrast, in a cubic geometry, the maximum total momentum is set by the condition $3\hbar^2 k^2/(2m) < U_D$, where the factor of three arises from the projections onto each of the Cartesian axes. Our quench protocol would therefore give a sharper cut for a cubic geometry.

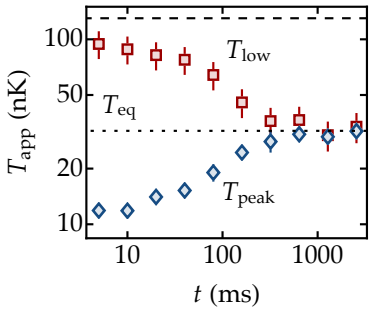

Figure 5.7 | **Apparent temperatures** independently calculated from the low-k occupation (T_{low}, red) and position of the peak of the spectral energy density (T_{peak}, blue). These converge to the expected equilibrium temperature, T_{eq}, for a saturated gas with the given energy. The pre-quench $T \approx 130$ nK (dashed). Figure adapted from [18].

5.3.2 Dynamics of the distribution

Having created a far-from-equilibrium distribution, we now turn to the dynamics as the gas thermalises. We confirm that our system is a closed one: as shown in Fig. 5.6(a), during thermalisation (at $300\,a_0$) the total N and E remain constant. In Fig. 5.6(b) we plot both the spectral population density $\mathcal{N}_k = 4\pi k^2 n_k$ (left) and the spectral energy density $\mathcal{E}_k = \mathcal{N}_k \hbar^2 k^2/(2m)$ (right); here the conserved N and E, respectively, correspond to the areas under the curves. As indicated by the arrows, we observe bidirectional dynamics in

momentum space [134]: while the majority of atoms flow to the IR, where the condensate emerges, the energy, carried by a small fraction of atoms, flows to the UV.

Apparent temperatures

This bidirectional nature is further highlighted by comparing properties of the $\mathcal{N}_k$ and $\mathcal{E}_k$ distributions with the values they would have if the cloud were in equilibrium. In Fig. 5.7 we plot two different apparent temperatures, T_{low} and T_{peak}, that are both deduced from the distributions shown in Fig. 5.6(b) by (incorrectly) assuming equilibrium, and compare them with the temperature T_{eq} that a cloud with the same N and E would have in equilibrium.

The first apparent temperature, T_{low}, is determined from the low-k region of the population density $\mathcal{N}_k$. We consider momenta k satisfying $\sqrt{2m|\mu|/\hbar^2} \ll k \ll \sqrt{2mk_{\mathrm{B}}T/\hbar^2}$, where in equilibrium $\mathcal{N}_k$ can be approximated as

$$\mathcal{N}_k \approx \frac{Vk_{\mathrm{B}}m}{\pi^2\hbar^2} T \left[1 - \frac{2m\mu}{\hbar^2 k^2}\right]^{-1} . \tag{5.9}$$

We then define T_{low} as the saturated-gas limit ($\mu \to 0$) of the previous expression,

$$k_{\mathrm{B}}T_{\mathrm{low}} = \frac{\pi^2\hbar^2}{Vm}\mathcal{N}_k \,, \tag{5.10}$$

where we now take our experimental *non*-equilibrium $\mathcal{N}_k$ in the region of the low-k plateau, but exclude $k \lesssim 0.5\,\mu\mathrm{m}^{-1}$, where the quasicondensate emerges [see, e.g., the 2560-ms data in Fig. 5.6(b)]. The extracted T_{low} is insensitive to small changes in this threshold k value.

The second apparent temperature is related to the momentum $k_{\mathrm{peak}} = \mathrm{argmax}_k[\mathcal{E}_k]$ at which the energy density is maximal. Setting $\mathrm{d}\mathcal{E}_k/\mathrm{d}k = 0$, one finds

$$\begin{aligned} k_{\mathrm{peak}} &= \frac{2\sqrt{k_{\mathrm{B}}Tm}}{\hbar}\sqrt{1 + \tfrac{1}{2}W_0(-2e^{-2})} \\ &\approx 0.893\frac{2\sqrt{k_{\mathrm{B}}Tm}}{\hbar} \,, \end{aligned} \tag{5.11}$$

where $W_0(x)$ is the principal branch[4] of the Lambert W function [156, 157], i.e., the values $w > -1$ satisfying $we^w = x$. The resulting factor of ≈ 0.893 is an effect of the Bose statistics: the higher occupancies of low-k modes shift the peak to lower k relative to the classical result. We define the 'peak' temperature as

$$k_{\mathrm{B}}T_{\mathrm{peak}} \approx 0.314 \cdot \frac{\hbar^2 k_{\mathrm{peak}}^2}{m} \,. \tag{5.12}$$

[4] The alternative branch W_{-1} contains the trivial solution $W_{-1}(-2e^{-2}) = -2$, corresponding to the minimum of the spectral energy density at $k = 0$.

The temperature that the gas would have in equilibrium, T_{eq}, is determined from its energy[5],

$$T_{\mathrm{eq}} = \frac{1}{k_{\mathrm{B}}} \left(\frac{2E}{3\zeta(\frac{5}{2})V} \right)^{2/5} \left(\frac{2\pi\hbar^2}{m} \right)^{3/5} . \tag{5.13}$$

We see in Fig. 5.7 that $T_{\mathrm{peak}} \propto k_{\mathrm{peak}}^2$ is initially far below the equilibrium temperature, $T_{\mathrm{eq}} \approx 32\,\mathrm{nK}$. On the other hand, the low-k T_{low} is initially far above T_{eq} (and close to the pre-quench temperature). The two apparent temperatures thus evolve in opposite directions, and we find that they converge to T_{eq} on similar timescales.

5.3.3 Self-similar scaling

In the previous section, we saw the first signs that our experiments generate a bidirectional flow in momentum space while the gas is thermalising. A more challenging question to address, however, is whether the n_k curves measured at different t can be collapsed onto a single universal function using the scaling form in Eq. (5.6). This poses a particular challenge because the distributions are being scaled along both the k and n_k axes, and we do not *a priori* know the form of the universal function onto which we are collapsing the data. In this section, we first describe our optimisation procedure for determining the scaling parameters, before presenting our experimental results.

Optimisation procedure

Since we do not know the form of the universal function in advance, we have identified an optimisation procedure that does not require this knowledge. The optimum values of the scaling exponents α and β can be determined using an approach based on the F–statistic. This requires splitting the total variance in a set of data containing multiple subgroups into two components: the variation *between* the groups, and the variation *within* the groups. We first briefly review the F–statistic, before describing the specific approach we have taken for our experimental data.

F–statistic

We consider a general variable from which K samples of possibly variable size have been taken. We denote the variable Y_{ij}, with the index $i \in [1, K]$ corresponding to the sample, and index $j \in [1, N_i]$ corresponding to one of N_i measurements within sample i. The total number of measurements across all samples is $N = \sum_i N_i$. We define the in-sample and across-sample

[5] Here we assume that the equilibrium gas will be partially condensed; in the absence of a condensed component, one would also need to know N.

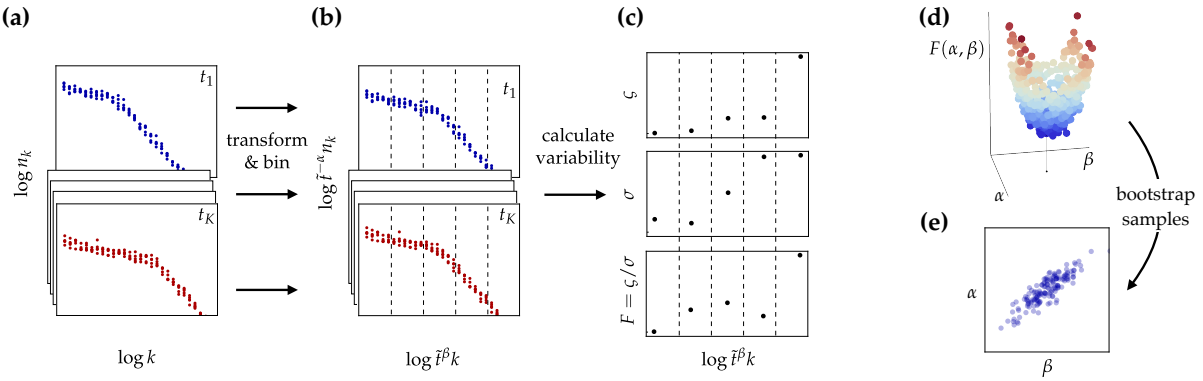

Figure 5.8 | **Scaling analysis. (a)** We start with a set of distributions $n_k(t)$ for several times t. **(b)** Test exponents α and β are chosen, and the data are rescaled and binned. **(c)** The F–statistic is determined within each bin from the variances ς and σ. **(d)** The F–statistic, summed over bins, forms a single point on the surface $F(\alpha, \beta)$. The (α, β) coordinates that minimise this surface constitute a single estimate of the optimum parameter values. **(e)** To determine the uncertainties in α and β, the whole procedure **(a-d)** is repeated for several bootstrap samples of the original data.

means as

$$\bar{Y}_i = \frac{1}{N_i} \sum_{j=1}^{N_i} Y_{ij}\,, \quad \text{and} \quad \bar{Y} = \frac{1}{N} \sum_{i=1}^{K} \sum_{j=1}^{N_i} Y_{ij} \tag{5.14}$$

respectively. The sum of squared differences of all data points from $\bar{Y}$ can then be decomposed[6] as

$$\sum_{i=1}^{K} \sum_{j=1}^{N_i} (Y_{ij} - \bar{Y})^2 = \sum_{i=1}^{K} \sum_{j=1}^{N_i} \left[(Y_{ij} - \bar{Y}_i)^2 + (\bar{Y}_i - \bar{Y})^2 \right] . \tag{5.15}$$

The first of these terms corresponds to the within-group variability, and the latter corresponds to the between-group variability. We define the corresponding mean sums of squares,

$$\sigma = \frac{1}{N-K} \sum_{i=1}^{K} \sum_{j=1}^{N_i} (Y_{ij} - \bar{Y}_i) \quad \text{and} \quad \varsigma = \frac{1}{K-1} \sum_{i=1}^{K} N_i (\bar{Y}_i - \bar{Y})^2 . \tag{5.16}$$

The ratio of these two is the F–statistic, $F = \varsigma/\sigma$, which measures the variance between the sample means relative to the mean variance within each sample. For gaussian uncertainties, this ratio is distributed according to the Fisher–Snedecor F–distribution, with degrees of freedom $(K-1,\, N-K)$ (see, e.g., [158]).

Application to momentum distributions

We use the F–statistic as a basis for constructing the cost function we need to minimise in order to identify the optimum α and β. The procedure is shown schematically in Fig. 5.8.

[6] The cross-term vanishes, as $\sum_j (Y_{ij} - \bar{Y}_i) = N_i(\bar{Y}_i - \bar{Y}_i) = 0$.

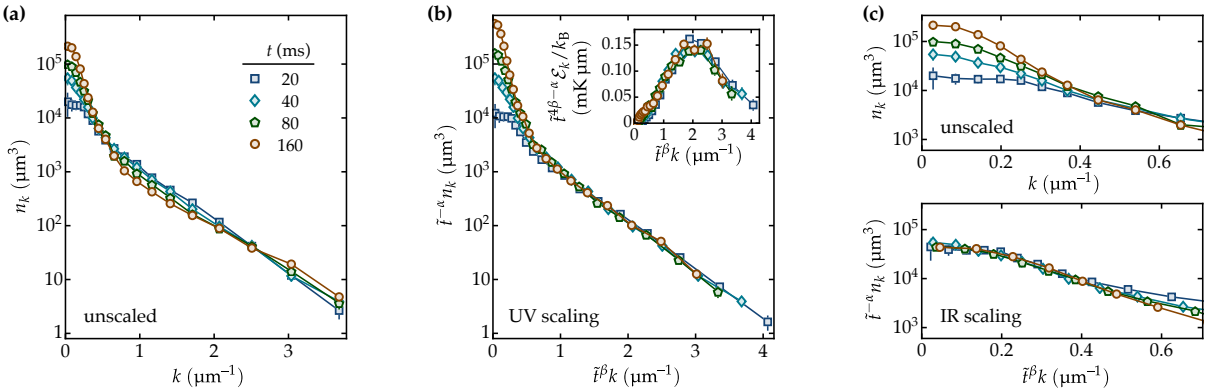

Figure 5.9 | **Self-similar scaling dynamics.** These data were taken with $a = 300\,a_0$ during the thermalisation dynamics. For scaling according to Eq. (5.6) we have taken $t_0 = 40\,\mathrm{ms}$. **(a)** Unscaled distributions n_k. **(b)** Ultraviolet scaling. Exponents $\alpha = -0.70(7)$ and $\beta = -0.14(2)$ collapse the curves at scaled momenta $\tilde{t}^{\beta}k \gtrsim 1\,\mu\mathrm{m}^{-1}$. The inset shows the same data converted to energy densities in order to better highlight differences. **(c)** Infrared scaling. Top: a zoom in of the unscaled data for low k. Bottom: exponents $\alpha = 1.15(8)$ and $\beta = 0.34(5)$ collapse the curves for $\tilde{t}^{\beta}k \lesssim 0.5\,\mu\mathrm{m}^{-1}$. Figure adapted from [18].

Our starting point in Fig. 5.8(a) is a set of momentum distributions for different hold times t, extracted as described in section 5.3.1. We then select exponents α and β, transform the momentum distributions according to Eq. (5.6), and allocate the data into bins along the now-scaled $\tilde{t}^{\beta}k$-axis, as in Fig. 5.8(b). We then calculate $F = \varsigma/\sigma$ within each $\tilde{t}^{\beta}k$-bin, treating different-t data as the different statistical groups [Fig. 5.8(c)]. Our cost function for the $\{\alpha, \beta\}$ exponents is then the sum of the the F–statistics over all bins. We repeat this for many $\{\alpha, \beta\}$, mapping out the surface $F(\alpha, \beta)$ as shown in Fig. 5.8(d), and find the α and β that minimise it. In order to estimate the uncertainty in our extracted scaling exponents, we perform the above analysis 80 times on bootstrap samples from the full dataset [Fig. 5.8(e)]; this means we take randomly-sampled subsets of our data, and from each subset determine a pair of exponents (α_i, β_i). The final values of α and β and their uncertainties are then the mean and standard deviation of the set of bootstrap-sampling results, and we have verified that the final results are independent of choices such as the size of k bins, or the bootstrap-sample size.

Experimental results

We now apply the scaling procedure from the previous section to our experimentally determined $n_k(k, t)$. For $a = 300\,a_0$ (as in Fig. 5.6), we observe dynamic scaling for $t \in [20\,\mathrm{ms}, 160\,\mathrm{ms}]$. In Fig. 5.9(a) we show the unscaled $n_k(t)$ curves. For the scaled ones in Fig. 5.9(b,c) we have arbitrarily set the reference time $t_0 = 40\,\mathrm{ms}$.

For initial non-equilibrium distributions like ours, knowledge of N and E is enough to determine what the equilibrium distribution must be. Moreover if we know, as we do in this case, that N and E are such that the equilibrium cloud will be (partially) condensed, the thermal,

higher-k part of the distribution is determined by E alone. It is therefore natural to assume that the system energy will determine a natural momentum scale separating the infrared and ultraviolet dynamics. Here the relevant scales are the inverse thermal wavelength $\lambda_T^{-1} \approx 0.6\,\mu\mathrm{m}^{-1}$, and the inverse healing length $k_\xi = \sqrt{8\pi na} \approx 0.7\,\mu\mathrm{m}^{-1}$; we have evaluated the former at $T = T_{\mathrm{eq}} = 32\,\mathrm{nK}$.

In Fig. 5.9(b) we see UV scaling in a broad momentum range $\tilde{t}^\beta k \gtrsim 1\,\mu\mathrm{m}^{-1}$, with $\alpha = -0.70(7)$ and $\beta = -0.14(2)$. In the inset we show the scaled $\mathcal{E}_k$ curves, which better highlight variations in the UV and can be directly compared with the unscaled curves in Fig. 5.6(b). The ratio of the scaling exponents, $\alpha/\beta \approx 5$, is consistent with energy-conserving transport in a three-dimensional system with quadratic dispersion. In Fig. 5.9(c) we focus on the complementary IR range of k, and show both unscaled (top) and scaled (bottom) distributions. Here we observe collapse for $\tilde{t}^\beta k \lesssim 0.5\,\mu\mathrm{m}^{-1}$, with $\alpha = 1.15(8)$ and $\beta = 0.34(5)$, and their ratio $\alpha/\beta \approx 3$ is consistent with particle-conserving transport.

We find that the underlying probability distribution for the extracted exponents shows a strong correlation between the extracted exponents. We plot a representative probability distribution in Fig. 5.10, which we have obtained for both our IR and UV exponents by calculating the covariance in the bootstrap-sampled distribution of (α, β) derived from the data shown in Fig. 5.9.

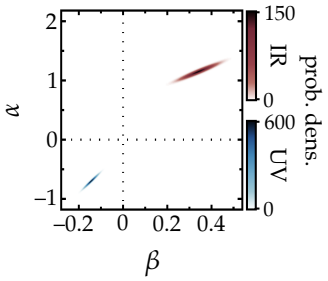

Figure 5.10 | Probability densities for the extracted exponents. Here one directly sees the correlation between α and β. Figure adapted from [18].

Structure function of the distribution

As we noted earlier, a complete characterisation of the scaling dynamics requires specification of both the scaling exponents α and β, as well as the corresponding structure function that describes the shape of the distribution. Whilst the collapsed data in Fig. 5.9 constitute a definition of this structure function in their own right, the existing theoretical work typically parameterises the function in terms of a power-law–crossover ansatz, of the form

$$f(\tilde{t}^\beta k) = 2A \left[\left(\frac{\tilde{t}^\beta k}{k_c} \right)^{\kappa_1} + \left(\frac{\tilde{t}^\beta k}{k_c} \right)^{\kappa_2} \right]^{-1} . \tag{5.17}$$

Here the two universal exponents $\kappa_1 < \kappa_2$ describe the low- and high-k power-law asymptotes respectively, and the values k_c and A identify the non-universal crossover scales [126, 159].

We fit the collapsed data from Fig. 5.9 using Eq. (5.17) and plot the fitted curves in blue on log-log axes in Fig. 5.11. For UV fits, we use data for which $\tilde{t}^\beta k \geq 1\,\mu\mathrm{m}^{-1}$, and for the IR, we use data with $\tilde{t}^\beta k \leq 0.5\,\mu\mathrm{m}^{-1}$. The panel insets show the residuals as an indication of goodness-of-fit; for this we use the relative deviations of the data from the fitted function, i.e.,

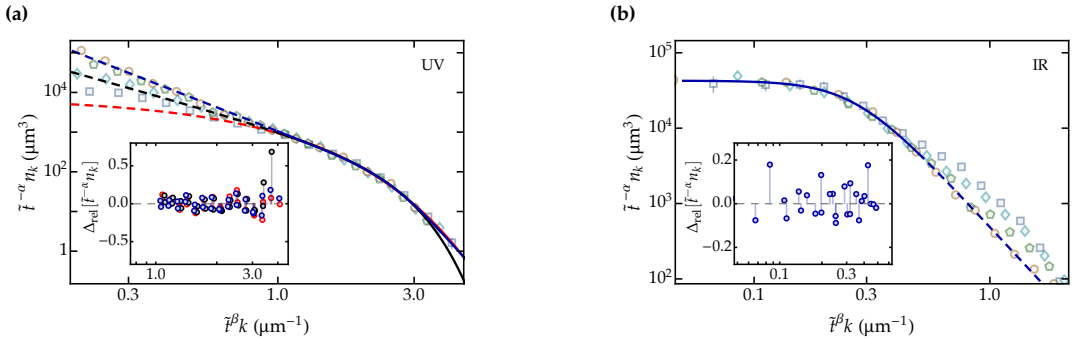

Figure 5.11 | **Parameterisations of the structure function.** Data shown are identical to Fig. 5.9(b,c), but here we use log-log axes. Insets of each panel show the relative residuals Δ_{rel}, defined as in Eq. (5.18). Solid curves indicate the domain of $\tilde{t}^{\beta}k$ used for fitting. **(a)** UV scaling region forms: power-law crossover (blue), exponential (red), and Bose distribution (black). **(b)** IR scaling using power-law crossover. Fitting forms and parameters for each of the curves are given in Table 5.1.

we plot

$$\Delta_{\mathrm{rel}}[\tilde{t}^{-\alpha} n_k] = \frac{\tilde{t}^{-\alpha} n_k - f(\tilde{t}^{\beta} k)}{f(\tilde{t}^{\beta} k)} \,. \tag{5.18}$$

We note that Eq. (5.17) is not the only choice for the functional form, but rather it is simply taken as a theoretically convenient one. In Fig. 5.11(a) we show the results of exponential [c.f. Fig. 5.9(b)] and Bose-distribution fits to our UV data, which both also capture the data well. All of the parameterisations are summarised in Table 5.1. The exponential model is reminiscent of a thermal distribution of phononic excitations; we note, however, that the inverse healing length $k_\xi = \sqrt{8\pi a n} \approx 0.7\,\mu\mathrm{m}^{-1}$, with n the coordinate-space density, would suggest that a phononic description is not suitable for our UV k range. The parameters we obtained for the Bose fit are not compatible with equilibrium values (c.f. section 2.3.1); however, interestingly, one sees that the UV k range of the distribution takes on the approximate *shape* of a Bose distribution long before the system reaches equilibrium.

Table 5.1 | **Fitting parameters for the curves shown in Fig. 5.11.** Stated uncertainties are standard errors on the mean.

Form	A (μm^3)	k_{c} (μm^{-1})	κ_1	κ_2
$2A[1 + (\tilde{t}^{\beta}k/k_{\mathrm{c}})^{\kappa_2}]^{-1}$ [IR]	$21(1) \times 10^3$	0.27(1)	–	3.4(2)
$2A[(\tilde{t}^{\beta}k/k_{\mathrm{c}})^{\kappa_1} + (\tilde{t}^{\beta}k/k_{\mathrm{c}})^{\kappa_2}]^{-1}$ [UV]	37(8)	2.6(1)	2.8(2)	8.3(6)
$A\exp(-\tilde{t}^{\beta}k/k_{\mathrm{c}})$	$7.4(3) \times 10^3$	0.483(5)	–	–
$A\{\exp[(\tilde{t}^{\beta}k/k_{\mathrm{c}})^2] - 1\}^{-1}$	$4.6(2) \times 10^2$	1.60(2)	–	–

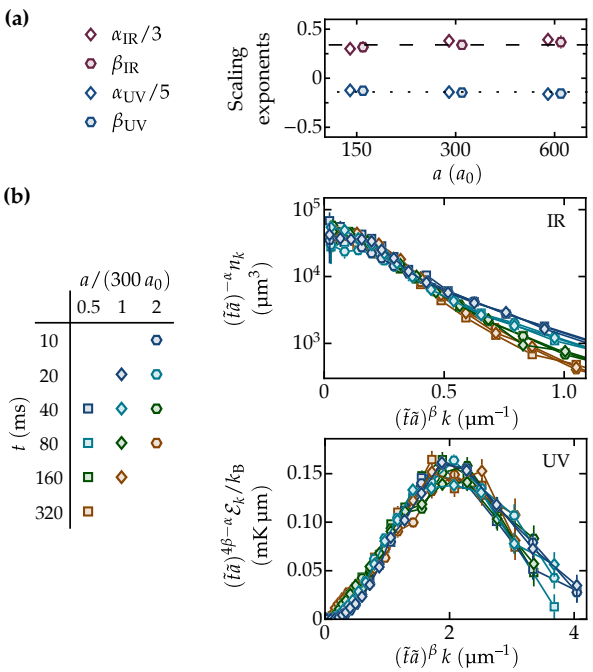

Figure 5.12 | **Universality for different interaction strengths. (a)** Scaling exponents are insensitive to the value of a during thermalisation; points for α and β are offset horizontally for clarity. The dashed and dotted lines show our a-averaged values $\beta_{IR} = 0.34$ and $\beta_{UV} = -0.14$ respectively. **(b)** Generalising $t \to t\tilde{a}$ in Eq. (5.6) collapses all curves taken in the interval $t\tilde{a} \in [20\,\text{ms}, 160\,\text{ms}]$; here $\tilde{a} \equiv a/(300\,a_0)$. Figure adapted from [18].

5.3.4 Universality for different interaction strengths

Having observed bidirectional scaling for a fixed interaction strength, i.e. for $a = 300\,a_0$, we now explore the generalisation of the dynamics to different interaction strengths. We repeat analogous experiments with $a = 150\,a_0$ and $600\,a_0$ during thermalisation at $t > 0$; the results are shown in Fig. 5.12. We find that our results for these new values of a remain essentially the same as our 300-a_0 ones if we rescale the thermalisation clock by $t \to t\tilde{a}$, where $\tilde{a} = a/(300\,a_0)$; $t_0 = 40\,\text{ms}$ throughout. For all a, we observe scaling dynamics in the interaction-normalised interval $t\tilde{a} \in [20\,\text{ms}, 160\,\text{ms}]$, and find that the measured scaling exponents are insensitive to a; our findings are summarised in Fig. 5.12(a). Combining all our data gives a-averaged values of $\alpha_{IR} = 1.08(9)$, $\beta_{IR} = 0.34(4)$, $\alpha_{UV} = -0.67(6)$, and $\beta_{UV} = -0.14(2)$.

In Fig. 5.12(b) we show that, both in the IR and in the UV, generalising $t \to t\tilde{a}$ in Eq. (5.6) collapses all our different-a curves taken within the scaling $t\tilde{a}$-interval[7]; here we use our a-averaged scaling exponents, and for visual clarity in the UV we show scaled $\mathcal{E}_k$ curves rather than n_k itself. We see here that, in addition to the insensitivity of the exponents α and β to a, there are also no significant changes in the underlying structure function, for either the IR or UV dynamics. Indeed, fixed-$t\tilde{a}$ curves coincide with one another even *outside* the scaling

[7] We have also considered a more general interaction-scaling $t \propto a^{-p}$ and optimised the collapse of the curves in Fig. 5.12(b) with respect to p; this gave $p_{IR} = 0.9(1)$ and $p_{UV} = 1.1(1)$.

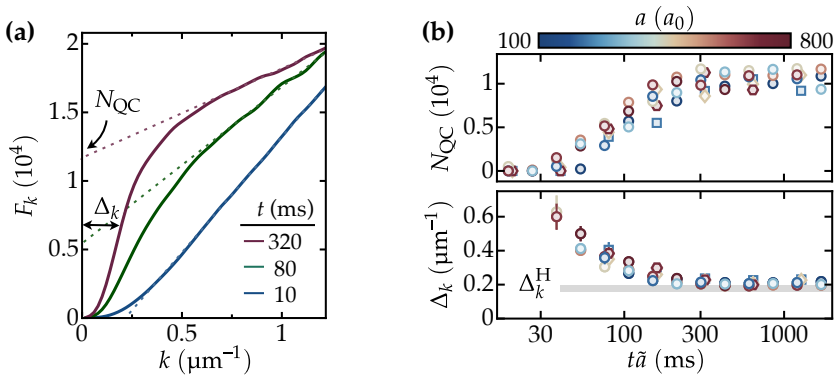

Figure 5.13 | **Quasi-condensation and phase ordering. (a)** We extract the quasi-condensate atom number, N_{QC}, and momentum-space width, Δ_k, from the cumulative particle distribution F_k; here $a = 300\,a_0$. **(b)** Evolution of N_{QC} and Δ_k for various interaction strengths is given by universal curves when plotting against the interaction-scaled time, $t\tilde{a}$. At long times Δ_k approaches the Heisenberg limit (grey bar), corresponding to a fully coherent condensate. Figure adapted from [18].

region, e.g., in the IR data of Fig. 5.12(b) for $(\tilde{t}\tilde{a})^\beta k \gtrsim 0.5\,\mu\text{m}^{-1}$.

This also addresses the fundamental question of time- and energy scales that we introduced in section 5.2.2. Our data show that, for our experimental parameters, the characteristic timescales are set by the inverse interaction energy, rather than the inverse two-body scattering rate, $\propto 1/a^2$. Defining the characteristic time set by the inverse interaction energy, $\tau = \hbar/(gn)$, where $g = 4\pi\hbar^2 a/m$ and n is the coordinate-space particle density, the scaling interval $t\tilde{a} \in [20\,\text{ms}, 160\,\text{ms}]$ for all a corresponds to $t \in [8.5\,\tau, 68\,\tau]$.

5.4 Condensate growth

We now turn to the properties of the condensate that emerges during thermalisation. We shall focus here on the evolution of two main quantities: the number of atoms in the condensate, and its characteristic momentum width. The IR scaling in Figs. 5.9 and 5.12 implies that the characteristic momentum width of the condensate, Δ_k, is reducing. This is not consistent with the growth of a BEC that is fully coherent from the moment it first exists; in this scenario, the condensate would have a fixed Heisenberg-limited width Δ_k^H set by the system size [160], with $\Delta_k^H \to 0$ in the thermodynamic limit. Instead, the reducing Δ_k is consistent with the out-of-equilibrium quasicondensate (QC) picture we introduced in section 5.2.2, which has $\Delta_k > \Delta_k^H$, and only with full phase ordering do we expect $\Delta_k \to \Delta_k^H$. Generally speaking, Δ_k^{-1} is an alternative representation for the coordinate-space coherence length.

We quantify changes in the quasicondensate properties following the methods in [136]. We define the QC atom number, N_{QC}, and width, Δ_k, as illustrated in Fig. 5.13(a), via the cumula-

tive atom distribution,

$$F_k(k) = \int_0^k \mathrm{d}k' \, \mathcal{N}_k(k') \,. \tag{5.19}$$

In the thermodynamic limit, for an ideal equilibrium gas of (large) volume V and with N_0 condensed atoms, $F_k = N_0 + cTk$ for $k \to 0$, where $c = Vmk_\mathrm{B}/(\pi^2\hbar^2)$. The low-$k$ contribution of the saturated thermal gas to F_k is linear in k, since $\mathcal{N}_k$ is independent of k in the classical-field regime [Eq. (5.9)]. The infinite-system-size case has the BEC localised in $k = 0$, whereas in a finite-size and/or nonequilibrium gas, the (quasi-)condensate contribution to F_k is spread over $\sim \Delta_k$. In this latter case, however, one can still see a low-k shoulder in F_k and the same linear regime beginning at slightly larger k [around $1\,\mu\mathrm{m}^{-1}$ in Fig. 5.13(a)]; here, the slope corresponds to our earlier definition of T_low [Eq. (5.10)]. We linearly fit the data for $k > 0.8\,\mu\mathrm{m}^{-1}$ (dotted lines) and define N_QC by the intercept of this fit (where this is positive; negative intercepts mean $N_\mathrm{QC} = 0$). Finally, we define Δ_k as the k range that contains an atom number of $N_\mathrm{QC}/2$.

In Fig. 5.13(b) we show the evolution of N_QC and Δ_k, and how, at times beyond the scaling interval $t\tilde{a} \in [20\,\mathrm{ms}, 160\,\mathrm{ms}]$, they approach their equilibrium values. We include additional data taken for various $a \in [100\,a_0, 800\,a_0]$, which, as we would expect from Fig. 5.12, all fall onto universal curves when plotted against the interaction-scale time, $t\tilde{a}$. Since our pre-quench gas is close to condensation, the QC emerges soon after the start of thermalisation, but initially Δ_k is notably above the Heisenberg limit, suggesting a high density of excitations. At long times, the condensed fraction N_QC/N approaches $40(5)\,\%$, consistent with the equilibrium temperature [Eq. (5.13)] calculated from the total energy E shown in Fig. 5.6(b), while Δ_k approaches the Heisenberg limit, corresponding to a fully coherent BEC.

5.4.1 Determining the Heisenberg width

We obtain the theoretical prediction for the Heisenberg width, Δ_k^H, by numerically finding the ground state of the Gross–Pitaevskii equation (see appendix A). For these calculations, we model the trap as a hard-wall cylinder with a simulated trap depth much greater than the chemical potential of the condensate, and take the condensate atom number to be 10^4 atoms. Our simulations use a spatial grid of 256^3 points, spanning a domain of $(150\,\mu\mathrm{m})^3$. Representative F_k curves obtained in this manner are shown in Fig. 5.14. To ensure a fair comparison between our experimental data and the theoretical Δ_k^H, we also simulate our experimental imaging process by integrating the 3D distribution along the imaging direction, and then performing the inverse-Abel transform (red curves). This ensures that the slight asymmetry between the cylinder's axial and radial directions is accounted for. We find a theoretical Heisenberg width of $\Delta_k^\mathrm{H} = 0.18(2)\,\mu\mathrm{m}^{-1}$ (red curves). Our stated uncertainty accounts for both the weak dependence on a, and the somewhat larger uncertainties in D and L. The simulated Δ_k^H values, as

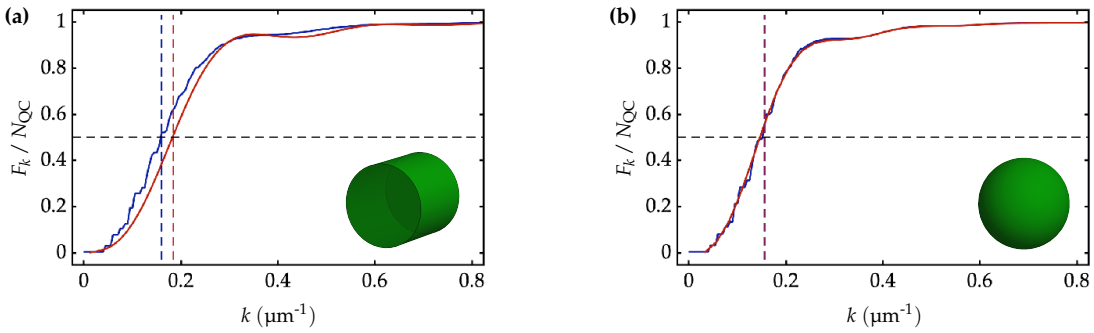

Figure 5.14 | **Determining Heisenberg widths using GPE simulations.** The data in both panels are for simulated data using 10^4 atoms and $a = 100\,a_0$. Blue curves show the F_k curves extracted from the full 3D distribution. Red curves show the F_k obtained by first integrating along the imaging direction, and then performing the inverse-Abel transform. Dashed lines indicate $F_k/N_{QC} = 0.5$ (grey), and the extracted Δ_k values (red, blue). **(a)** Cylindrical box. **(b)** Spherical box of equal volume.

well as our long-thermalisation-time Δ_k data in Fig. 5.13, are consistent with $0.21(2)\,\mu\text{m}^{-1}$ that we experimentally observe for a slowly prepared equilibrium condensate of 10^4 atoms.

One sees in Fig. 5.14(a) that the line-of-sight integration and inverse-Abel transform do slightly increase our calculated Δ_k^{H} above the value $\approx 0.16\,\mu\text{m}^{-1}$ that we find if we use the fully 3D distribution instead. We verify that this effect is due to the cylindrical geometry by performing the same simulations using a spherical box of equal volume [Fig. 5.14(b)]; here, as expected, we see no difference in the F_k extracted from fully 3D distributions, or using the inverse-Abel transform. We highlight that the theoretical Δ_k^{H} for the spherical box, $\Delta_k^{\text{H}} = 0.15(2)\,\mu\text{m}^{-1}$, is only slightly smaller than the cylindrical case.

5.5 Conclusion

The experiments presented in this chapter provide a comprehensive picture of the universal bidirectional dynamic scaling in an isolated quantum gas, quasi-condensation, and phase ordering. We have measured the scaling exponents α and β for both the particle-conserving dynamics in the infrared, and the energy-conserving dynamics in the ultraviolet. In both cases our measured ratios, α/β, are consistent with our expectations based on fundamental conservation laws. Our experiments provide benchmarks for the values of the individual exponents, which remain the subject of extensive theoretical work. For the UV dynamics, our $\beta_{\text{UV}} = -0.14(2)$ is close to the prediction for weak-wave turbulence [137, 161], $\beta_{\text{UV}} = -1/6$. NTFP theories [124–128] generally predict $\beta_{\text{IR}} = 1/2$ for the IR dynamics, but recent work [127, 128] also suggests the possibility of $\beta_{\text{IR}} = 1/3$; this latter result is closer to our observed $\beta_{\text{IR}} = 0.34(6)$. In the future, it would be interesting to perform similar quench experiments starting far above T_c, since the dynamics on the way to (quasi-)condensation and following its onset are expected

to be different [141]. Experiments in the (quasi-)2D regime would also be invaluable; here, one could directly image the vortices that are expected to form as a result of the cooling quench, and study their role in the NTFP dynamics. It may also be interesting to perform a complementary study by directly probing the first-order correlation function $g^{(1)}(r)$ using Bragg-based techniques (e.g. [116, 162]).

6 Bose gases and the unitary regime

We have seen in the previous chapters that the Bose gas is a versatile platform that is well suited for studying out-of-equilibrium phenomena in weakly and moderately interacting systems. Thus far, we have focussed on parameter regimes in which the scattering length a is positive and finite. In this chapter we turn instead to the resonant regime where $|a| \to \infty$, known as unitarity, or the unitary regime[1]. Here, interactions are as strong as allowed by quantum mechanics, and one expects the gas to exhibit strong spatial correlations.

We begin in section 6.1 with a general introduction to the unitary regime. Next, we turn in section 6.2 to the details of our experiment, focussing in particular on the quench protocol we use in order to access the regime. Finally, we present the results of our studies of homogeneous Bose gases quenched into the unitary regime, separating the results according to the initial condition in which the gas is prepared. Initially degenerate gases are discussed in section 6.3, and initially thermal gases in section 6.4. The main results of this chapter appear in [15, 16] and additional detail is available in [11]; the latter sections of this chapter closely follow the discussions presented therein.

6.1 The unitary regime

The unitary regime has been a very fruitful area of study in the context of Fermi gases [164–166]. Perhaps the most famous example is the crossover between Bardeen–Cooper–Schrieffer superconductivity and the Bose–Einstein condensation of diatomic molecules [167–172]. While the unitary Bose gas promises its own equally intriguing prospects, including novel forms of superfluidity [173–175] and universal behaviour dependent only on the gas density [176, 177], the unitary Bose gas remains less explored than its Fermi counterpart. The discrepancy in the depth of study between the unitary Fermi and unitary Bose gas owes itself in part to Pauli exclusion. Whereas Fermi systems typically have limited densities, Bose gases, especially degenerate ones, typically feature very high densities. As a consequence strongly interacting Bose gases are plagued by enhanced density-dependent heating and atom loss. The unitary Bose gas is therefore an inherently dynamical and non-equilibrium problem, with complex interplay between the coherent and dissipative dynamics. In spite of these challenges, theoret-

[1] Following, e.g., [4, 163] we write $|a| \to \infty$; the rates of physical processes that would normally depend on a do *not*, however, show the same divergence, but rather saturate as other lengthscales become relevant.

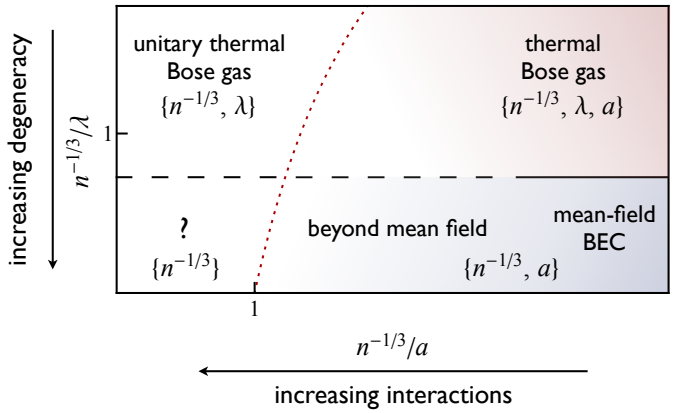

Figure 6.1 | **Sketch of the equilibrium phase diagram of an interacting Bose gas.** By varying the thermal wavelength $\lambda \propto 1/\sqrt{T}$ via the gas temperature T, and the interaction strength via the scattering length a, one can systematically eliminate lengthscales. In the bottom-left corner, we identify a region in parameter space within which we expect to observe universal dynamics that depend solely on the interparticle spacing, $n^{-1/3}$. Figure reproduced from [11].

ical [175, 178–204] and recently also experimental [57, 205–211] studies are making progress in what promises to remain an exciting research avenue into the future.

Let us consider the cartoon sketch of the equilibrium phase diagram of an interacting Bose gas shown in Fig. 6.1, where we denote the gas density n. At the top right, we have a weakly interacting thermal gas, which has three relevant lengthscales[2]: the interparticle spacing $n^{-1/3}$, thermal wavelength $\lambda \propto 1/\sqrt{T}$, and the s-wave scattering length a. Cooling the gas such that the temperature $T \to 0$, takes us into the mean-field BEC region, where the condensate dynamics are described with a macroscopic wavefunction obeying the Gross–Pitaevskii equation; in this $T \to 0$ limit, λ is completely eliminated from the problem, leaving only $\{n^{-1/3}, a\}$. In order to access the strongly interacting regions on the left hand side of the figure, we can exploit the magnetic Feshbach resonance (see section 3.3.1) to increase the scattering length $a \to \infty$ and thereby (also) eliminate a.

At the top left of the figure, we have the unitary thermal Bose gas. Here, there are two lengthscales in the problem, namely $n^{-1/3}$ and λ. Fortunately, in many cases, the n and T dynamics are coupled, so that universal behaviour is possible. For example, experimental studies using harmonically trapped thermal gases [206, 207, 209] have confirmed universality in the loss dynamics. We will return to the coupled dynamics of n and λ in greater detail alongside our experimental results in section 6.4.

In the lower left of Fig. 6.1, we identify a region in which the interparticle spacing is the sole remaining lengthscale. The corresponding natural momentum, energy, and time scales, known

[2] In principle, the trap extent is also relevant for finite-size systems. In this chapter, both the radius and length of our cylindrical trap are much greater than the (up to) three remaining lengthscales, i.e. effectively infinite.

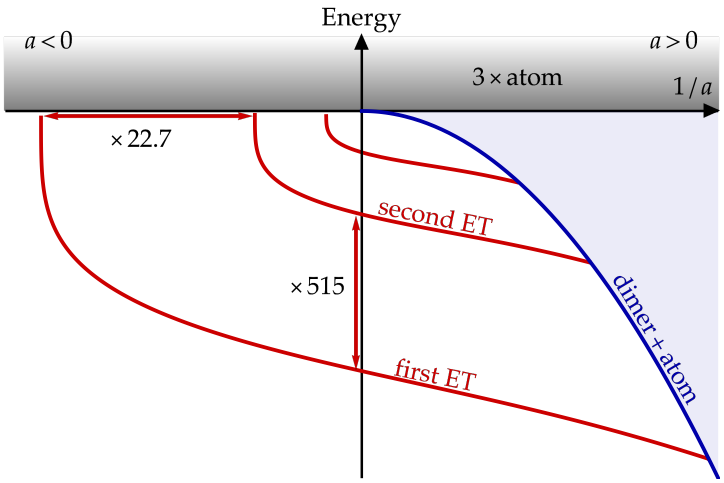

Figure 6.2 | Cartoon sketch of the binding energies of Feshbach dimers and Efimov trimers. Here we sketch the binding energies against the inverse two-body scattering length, $1/a$. In addition to the Feshbach dimers, which have binding energies $\propto 1/a^2$ (blue), there also exists an infinite series of weakly bound Efimov trimer (ET) states; we sketch the energies of only the three most tightly bound trimers (red curves). Shading indicates the continuum regions for three atoms (grey) and for an atom plus a dimer (blue). Curves are not shown to scale; in reality, the sizes of successive Efimov trimers differ by a factor of 22.7, and the energies are spaced by a factor of $22.7^2 \approx 515$. Figure adapted from [163].

as Fermi scales, are then given by

$$\hbar k_n = \hbar(6\pi^2 n)^{1/3}, \quad E_n = \frac{\hbar^2 k_n^2}{2m}, \quad \text{and} \quad t_n = \frac{\hbar}{E_n}; \tag{6.1}$$

these definitions apply equally to both Fermi and Bose gases.

The single-scale nature in this parameter region implies that the system's dynamics will be universal. For Bose gases this universality can, however, be violated due to a quantum few-body effect known as the Efimov effect [34, 35, 57, 163, 210, 212–217]. Efimov physics, first studied in the context of nuclear physics, predicts the existence of an infinite series of three-body states that cannot be constructed using only two- and one-body states, i.e., these Efimov trimers can exist even in the absence of two-body bound states.

Fig. 6.2 gives an overview of the energies of both Feshbach dimers and Efimov trimers (e.g., [163]). The Feshbach dimers we have discussed already in section 2.5; the key features to remember are that the dimer size is given by a, and close to the resonance (i.e., $1/a \to 0$) its binding energy is $E_\mathrm{b} \approx \hbar^2/(ma^2)$. We also make special note of two main features of the Efimov-state series. Firstly, the trimer states form an infinite geometric series: successive trimer states differ in size by a factor of 22.7, and the corresponding binding energies along the $1/a \to 0$ axis differ by a factor of $22.7^2 \approx 515$. Secondly, whereas the binding energy of the Feshbach dimers tends to zero in the limit $1/a \to 0$, the trimer states persist with finite binding energies at the resonance and indeed also across it, into the negative-a region; as a result, the sizes of the trimer states introduce additional lengthscales that are believed to influence the otherwise

universal dynamics at unitarity [175, 191, 196, 214].

Even in the absence of Efimov effects, however, there remain many questions about the unitary regime. It is, for instance, not clear *a priori* whether coherent or dissipative dynamics are expected to dominate; this in turn raises the question of whether the gas has well-defined equilibrium properties in this regime. It is perhaps natural to expect the unitary Bose gas to have a ground state with energy of order E_n. This is indeed in line with theoretical estimates [181, 183, 184, 193, 218] that predict a ground-state energy in the range $[0.39\,E_n,\ 1.75\,E_n]$. An early experimental step into the unitary regime [205] corroborates this picture, with the authors having obtained a lower bound for this same energy of $0.44(8)\,E_n$.

Rather than focussing on equilibrium properties, however, more recent experiments have turned towards extracting useful information about the regime using a non-equilibrium approach. Makotyn et al. spearheaded this shift [208], using rapid interaction-strength quenches to take a degenerate gas into the unitary regime. Their experiments showed that, during a variable evolution time at unitarity, the momentum of the gas evolves to a quasi-steady-state distribution, suggesting that the momentum-redistribution processes take place on a shorter timescale than the dissipative ones. Although there has been experimental evidence of novel three-body correlations [57] and Efimov trimers [210], all measured degenerate-unitary-gas dynamics [206–210] have been consistent with the universality hypothesis, under which t_n is the only characteristic timescale.

All previous experiments on the unitary Bose gas have been performed with harmonically trapped gases, and their interpretation relies on knowledge of the inhomogeneous density profiles. While this density profile is known for the weakly interacting pre-quench gas, the density-dependent loss and strong interactions at unitarity complicate the subsequent evolution. In our experiments, we have a uniform density and so the Fermi scales in Eq. (6.1) are *global* properties in our system[3], which can be derived from the total atom number N and trapping volume V. Moreover, one expects the density to *remain* uniform even as atoms are lost from the trap; we can therefore study the evolution of the cloud as it dynamically decays and heats, and we are not constrained to studying the dynamics only immediately after the quench.

6.1.1 Atom-loss scaling laws

A central component of the experimental results we discuss in the coming sections is the rate at which atoms are lost from the gas while it is in the unitary regime. In this section, we present theoretical predictions of the relevant atom-loss scaling laws. For the densities and interaction

[3] Due to edge effects near the trap walls, the density is never perfectly uniform through the box; however, we assess that for more than 80 % of the atoms the local E_n is within 10 % of the trap average value.

strengths relevant in this chapter, three-body recombination is the dominant loss process[4]. As we have seen in chapter 4, the per-particle three-body loss rate is written

$$\frac{\dot{N}}{N} = -g^{(3)} L_3 \langle n^2 \rangle \,. \tag{6.2}$$

where $g^{(3)}$ is the zero-distance three-body correlation function, L_3 is the three-body–loss coefficient, and $\langle n^2 \rangle$ denotes the trap-averaged squared density. A thermal Bose gas has $g^{(3)} = 3!$, and an ideal-gas condensate has $g^{(3)} = 1$. For moderately strongly interacting gases, one must include the beyond-mean-field LHY corrections [219,220] to $g^{(3)}$ for the condensate,

$$g^{(3)} \approx 1 + \frac{64}{\sqrt{\pi}} \sqrt{n a^3} \,; \tag{6.3}$$

this correction arises due to the depletion of the condensate. For degenerate gases away from unitarity[5], and neglecting the log-periodic Efimov features, $L_3 \propto \hbar a^4 / m$ [85,221]; we shall deal with unitarity-limited L_3 values separately below. The homogeneous density in our experiments allows us to simplify Eq. (6.2) by writing $\langle n^2 \rangle = N^2/V^2$. Allowing for the possible (indirect) dependence of L_3 on N, we can then re-express Eq. (6.2) in terms of N rather than $\langle n^2 \rangle$, and also integrate to obtain the solution to the differential equation,

$$\frac{\dot{N}}{N} = -c_0 N^\gamma \,, \quad \text{and} \tag{6.4a}$$

$$N(t) = \left[c_0 \gamma t + N_0^{-\gamma} \right]^{-1/\gamma} \tag{6.4b}$$

for an appropriate choice of constant c_0 and exponent γ.

Thermal unitary regime

As the result of an interaction-strength quench into the unitary regime, a diverges and is eliminated from the problem; physical quantities that normally depend on a in non-unitary gases must then be given in terms of other lengthscales in the infinite-a limit. In the case of a thermal unitary gas, the diverging a is replaced by the thermal wavelength λ. We then have $L_3 \propto \hbar \lambda^4 / m \propto 1/T^2$, and so $\dot{N}/N \propto -N^2/T^2$ in our constant-volume homogeneous gas. A more precise quantitative treatment yields

$$L_3 = \zeta_3 \frac{3\sqrt{3}\hbar}{2m} \lambda^4 = \zeta_3 \frac{6\sqrt{3}\pi^2\hbar^5}{m^3 (k_\mathrm{B} T)^2} \,, \qquad \text{and} \tag{6.5a}$$

$$\frac{\dot{N}}{N} = -\zeta_3 \frac{36\sqrt{3}\pi^2\hbar^5}{m^3 k_\mathrm{B}^2 V^2} \frac{N^2}{T^2} \tag{6.5b}$$

[4] Our one-body lifetime that arises due to collisions with the background gas is $> 100\,\mathrm{s}$, and there are no two-body collisions in the hyperfine ground state; the unitary-gas experiments described in this thesis involve hold times at unitarity of $\leq 2\,\mathrm{ms}$.

[5] We assume that a is nevertheless large compared to the van der Waal's radius for ^{39}K, $\approx 60\, a_0$.

in the absence of the theoretically expected weak modulation[6] log-periodic in T; here $\zeta_3 = (1 - \exp[-4\eta^*])$ is a non-universal prefactor arising from Efimov physics [206, 207, 209, 223–225]. Specifically, this prefactor accounts for the fraction $\exp(-4\eta^*)$ of three-body collisions that produce an Efimov trimer, rather than resulting in atom loss; the Efimov width parameter η^* links the trimer energy E_T with its lifetime $\hbar/(\eta^* E_\mathrm{T})$. Loss rates consistent with Eq. (6.5a) have been measured using thermal unitary gases in harmonic traps [206, 207, 209].

As we alluded to earlier, the N and T dynamics of the thermal unitary Bose gas are coupled. We therefore seek to replace the explicit $1/T^2$ dependence of Eq. (6.5b) with an equivalent N dependence. Whereas three-body loss can cause cooling in weakly interacting homogeneous gases (see chapter 4), in a thermal unitary gas it results in strong heating. Here, the unitarity-limited scattering cross-section $\sigma = 8\pi/(k^2 + a^{-2}) \approx 8\pi/k^2$ leads to faster loss rates for atoms with lower relative momenta [206, 209]. We quantify the heating effect following [206, 209], by noting that conservation of energy during a loss event requires

$$\alpha N k_\mathrm{B} T = \alpha(N + \mathrm{d}N) k_\mathrm{B}(T + \mathrm{d}T) - (\alpha - \delta_3) k_\mathrm{B} T \mathrm{d}N\,. \tag{6.6}$$

The left hand side of Eq. (6.6) is the total thermal energy before a collision, with $\alpha = E/(k_\mathrm{B}T) = 3/2$ for phase-space densities $n\lambda^3 \ll 1$. The first term on the right hand side corresponds to the post-recombination energy of atoms that remain trapped, while the second term corresponds to the atoms that are lost. Here $\delta_3 = 2/3$ corresponds to the k-averaged excess energy per particle that remains in the trap following a three-body loss event. We simplify Eq. (6.6) to read

$$\frac{\mathrm{d}T}{T} = -\frac{\delta_3}{\alpha}\frac{\mathrm{d}N}{N} = -\frac{4}{9}\frac{\mathrm{d}N}{N}\,, \tag{6.7}$$

and therefore $T \propto N^{-4/9}$. Combining this result with Eq. (6.5b) and comparing with Eq. (6.4), we have $\dot{N}/N \propto N^{-26/9}$, and we identify the loss rate power-law scaling exponent $\gamma = 26/9$ for the thermal unitary Bose gas.

Degenerate unitary regime

Within the scope of the universality hypothesis [177], the Fermi scales introduced in Eq. (6.1) are the only length-, time-, and energy scales in the degenerate unitary regime. Since the loss rate is a reciprocal time, it then follows on dimensional grounds that we must have

$$\frac{\dot{N}}{N} = -\frac{A}{t_n}\,, \tag{6.8}$$

for some dimensionless constant A; in other words, $\dot{N}/N \propto n^{2/3}$, and so $\gamma = 2/3$. We note that this argument does not rely on the atom loss being due to three-body recombination, but rather

[6] Such a modulation has not been experimentally resolved in bosonic gases. Indeed, this would be a rather challenging pursuit: for identical bosons the relative oscillation amplitude $\approx 0.022 e^{-2\eta^*}$ (a few percent for typical η^*) is weak, and the log-T period of $e^{4\pi/s_0} \approx 3 \times 10^5$ ($s_0 = 1.00624$) leads to extremely slow variation with T [209,222].

applies equally to all higher-order loss processes[7]. This degenerate-gas loss-rate scaling has been experimentally observed [210] for densities spanning more than two orders of magnitude, using the initial loss rates of a harmonically trapped gas of ^{85}Rb quenched to unitarity. There, the authors found $A \approx 0.18$. As was the case in the thermal unitary regime, however, we do expect some deviations from universal behaviour; the constant A in general depends on non-universal Efimov physics via ζ_3, and we also expect log-periodic modulation of the loss rate[8] as a function of n [198, 226].

6.2 Experimental quench protocol

In this section, we describe our experimental protocol for quenching a Bose gas into the unitary regime. We have used quenches in our experiments because, for the range of parameters we are able to explore, the per-particle loss rate exceeds the rate of two-body collisions that drive thermalisation [11]; this precludes preparation of an equilibrium unitary state. For the experiments described in this chapter, we have used the same trapping parameters throughout: the cylindrical box potential has an aspect ratio $2R/L \approx 0.63$ and our data are consistent with a constant trapping volume $V \approx 3 \times 10^{-14}\,\mathrm{m}^3$. We note that variations in the ratio of the typical energy scale of the gas ($k_\mathrm{B}T$ for thermal gases, and $\mu \propto Na$ for weakly interacting condensates) to the trap depth lead to small, yet measurable changes in the effective volume. We account for these changes by measuring a nominal volume[9] for a fixed ratio of gas energy to trap depth, and correct the remaining data assuming a power-law potential $\sim r^{15(4)}$ (see section 3.1.2).

We illustrate our quench protocol for an initially degenerate gas in Fig. 6.3. We begin our experiments by preparing an equilibrium gas in the weakly interacting regime, with $n_0 a^3 < 10^{-3}$. For our degenerate-gas experiments, we prepare the gas in a trap of depth $U_0 \approx k_\mathrm{B} \times 50\,\mathrm{nK}$ and use initial atom numbers in the range $1 \times 10^4 \leq N_0 \leq 22 \times 10^4$, with corresponding initial densities $0.4\,\mu\mathrm{m}^{-3} \leq n_0 \leq 5.2\,\mu\mathrm{m}^{-3}$ and initial Fermi times $150\,\mu\mathrm{s} \geq t_{n_0} \geq 27\,\mu\mathrm{s}$.

In order to access the unitary regime, we exploit the Feshbach resonance of the ^{39}K hyperfine ground state centred at $B_\infty = 402.70(3)\,\mathrm{G}$. The range of fields near B_∞ for which $n_0 a^3 > 1$ for our full range of n_0 is[10] $\delta B \sim 60\,\mathrm{mG}$. We enter the unitary regime by rapidly quenching the magnetic field to B_∞ using the auxiliary coils described in section 3.3.1. Our field quenches correspond to a change in magnetic field of up to $\Delta B \approx 3.6\,\mathrm{G} \approx 60\,\delta B$ within $2\,\mu\mathrm{s} \ll t_{n_0}$, setting

[7] See [11] for an explicit consideration of the general i-body loss rates.

[8] The period of the oscillation corresponds to a change in density of a factor of $\exp(3\pi/s_0) \approx 10^4$, where $s_0 = 1.00624$ for identical bosons. The ^{85}Rb data from [210, 226] show a suppression at the predicted position of the minimum, however systematic uncertainties in the mean density render the results therein inconclusive.

[9] Details of both the volume extraction and power-law characterisation of our potential can be found in [10, 11].

[10] We note that the magnetic-field gradient we use to cancel out the gravitational force on the atoms gives a variation of $\approx 25\,\mathrm{mG}$ across the cloud.

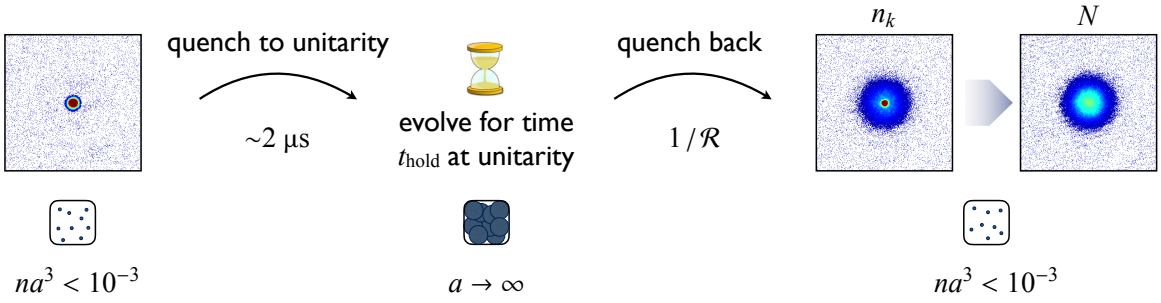

Figure 6.3 | **Quench protocol.** We prepare a quasi-pure BEC in the weakly interacting regime, with $na^3 < 10^{-3}$. The gas undergoes a rapid ($\approx 2\,\mu$s) interaction-strength quench into the unitary regime, where it is allowed to evolve for a time t_{hold}. We then reduce the interaction strength using a variable ramp-out rate $\mathcal{R} = -\mathrm{d}B/\mathrm{d}t$. To determine the post-quench momentum distribution n_k, we then reduce $a \to 0$ and allow the cloud to expand ballistically. To measure the atom number N, we instead expand the cloud with $a_{\mathrm{ToF}} \approx 10^3\, a_0$. Figure reproduced from [11].

a lower limit on our pre- and post-quench scattering length of $390\, a_0$. We raise the trap depth to $U_{\mathrm{h}} \approx k_{\mathrm{B}} \times 2\,\mu$K concurrently with the magnetic-field quench in order to avoid evaporative effects while the gas is held at unitarity[11] for a time t_{hold}. We then ramp the magnetic field away from unitarity, before imaging the atoms after an additional $(8-32)$ ms of expansion in time of flight (ToF).

We ramp the B field away from resonance by disconnecting the auxiliary coils from their power supply. The coils, in conjunction with external resistors, form an LR circuit, and so the B field decays exponentially (see section 3.3.1). Since our final magnetic field is always more than $10\,\delta B$ away from B_∞, the changing B field is well approximated as a linear ramp in and near the unitary regime. The initial ramp-out rate is given by $\mathcal{R} = -\mathrm{d}B/\mathrm{d}t = \Delta B/\tau_{\mathrm{Q}}$, where τ_{Q} is the exponential time constant of the magnetic-field ramp, which we can vary between 1 μs and 10 μs.

Changing the ramp-out speed affects the interpretation of our subsequent measurements of the atom number N and momentum distribution n_k, since the ramp out can result in a mixture of atoms and (Feshbach and/or Efimov) molecules [210,227–229], and our imaging only detects the free atoms. An infinitely fast ramp out should correspond to a projective measurement onto free-atom states, independent of the many-body state of the gas at unitarity. A slow ramp out, in contrast, allows molecules to form, and we detect fewer atoms using our imaging protocol. The differences in the observed atom numbers for different ramp speeds provide a measure of the correlations in the gas.

To faithfully determine both n_k and N for the initially degenerate gas, we use two slightly different approaches. For the former, we tune $a \to 0$ and release the cloud in ToF expansion.

[11] In separate studies at finite a (i.e., without quenching to unitarity), we find that the trap-depth quench induces dynamics at timescales $> 100\,\mu$s that lead to an overall energy increase $\lesssim 10\,\%$ of the unitarity-induced energy.

Provided the ToF is sufficiently long, our absorption images can be mapped directly to the post-quench line-of-sight–integrated momentum distribution (see section 5.3.1), from which we can reconstruct the three-dimensional n_k. For short t_{hold}, the gas still closely resembles its pre-quench quasi-purely condensed state, with a high density of atoms at low k. The low-k region of the images is therefore too optically dense to permit an accurate determination of N. To measure N we therefore repeat the quench experiment, but introduce a 40-ms wait time at $\approx 200\,a_0$ following the quench to allow the gas to rethermalise[12] and spread the BEC to larger momenta. We also use an increased scattering length of $a_{\mathrm{ToF}} \approx 10^3\,a_0$ during ToF to aid the expansion[13].

Our thermal gas measurements follow a similar protocol to that shown in Fig. 6.3, with several simplifications. Here we use a constant trap depth of $U_0 = U_{\mathrm{h}} \approx k_{\mathrm{B}} \times 3\,\mu\mathrm{K}$. The absence of a high particle densities concentrated at low k (otherwise originating from the pre-quench BEC) also negates the need to measure n_k and N using separate protocols; here the n_k measurements faithfully give both N and the energy per particle E.

6.3 Degenerate Bose gases quenched to unitarity

We begin by exploring the effect of the ramp-out rate in Fig. 6.4, in order to disentangle the unitary-loss dynamics from the molecule formation that takes place as the gas leaves the unitary regime. We differentiate between the total number of atoms N, and the observed number N_{obs}, the latter of which does not contain the atoms that have formed molecules [210], which we do not detect with our imaging. The open symbols in Fig. 6.4(b) show N_{obs} as a function of the inverse ramp-out rate $1/\mathcal{R}$, for a gas with $N_0 = 98 \times 10^3$ at a fixed $t_{\mathrm{hold}} = 80\,\mu\mathrm{s}$. We have varied $1/\mathcal{R}$ by changing both $1.8\,\mathrm{G} \leq \Delta B \leq 3.6\,\mathrm{G}$ and $1\,\mu\mathrm{s} \leq \tau_{\mathrm{Q}} \leq 10\,\mu\mathrm{s}$. We fit the data with an exponential, the characteristic form of a Landau–Zener process [227, 229], and extract an exponential constant $2.2\,\mu\mathrm{s\,G^{-1}}$. By extrapolating $1/\mathcal{R} \to 0$, we assess that our technically limited fastest ramp-out speed, $1/\mathcal{R} = 0.3\,\mu\mathrm{s\,G^{-1}}$, yields the true N to within $\lesssim 10\,\%$, and we have verified this for our full range of N_0 at several t_{hold}. We confirm that the reduction in N_{obs} occurs due to molecule formation by applying an additional 8-µs pulse (following the ramp out after t_{hold}) to break up any molecules that have formed[14]. This causes most of the missing atoms to reappear [solid squares in Fig. 6.4(b)].

In Fig. 6.4(c) we show the evolution of N_{obs} as a function of t_{hold} for both our fastest ramp-

[12] During this 40 ms window, the system is essentially closed. Varying U_{h} by $\pm 20\,\%$ does not change N_{obs} beyond its error bar, and measurements both with and without this wait time also give equal N_{obs} when there is no BEC present.

[13] We have verified that this does not introduce additional unwanted three-body loss during the expansion.

[14] As in [230], our N_{obs} shows an oscillation as a function of the time spent at low a; we optimise this time to recover the maximum number of atoms.

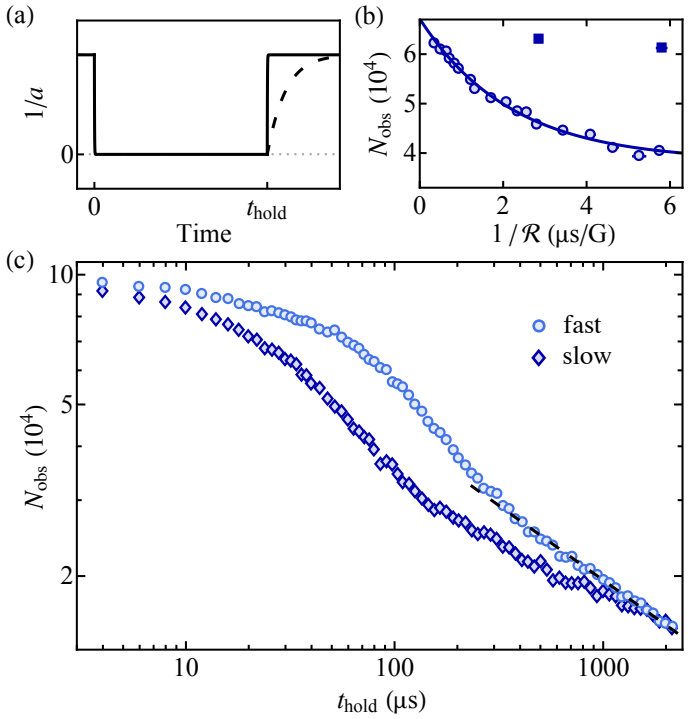

Figure 6.4 | **Atom-loss and correlation dynamics. (a)** Quench protocol. A quasi-pure BEC is quenched to unitarity where it is held for a time t_{hold}, before it is ramped back to the weakly interacting regime with a variable ramp-out rate $\mathcal{R} = -\mathrm{d}B/\mathrm{d}t$ (solid vs. dashed curves). **(b)** The observed atom number N_{obs} as a function of the inverse ramp-out rate, for $N_0 = 98 \times 10^3$ and $t_{\mathrm{hold}} = 80\,\mu\mathrm{s}$. An exponential fit to the data (solid line) gives a decay constant of $2.2\,\mu\mathrm{s\,G}^{-1}$. A second, short magnetic-field pulse to resonance dissociates molecules formed during the ramp out (solid squares). **(c)** The evolution of N_{obs} as a function of t_{hold} for our fastest ramp out ($0.3\,\mu\mathrm{s\,G}^{-1}$, circles) and a much slower one ($5.8\,\mu\mathrm{s\,G}^{-1}$, diamonds). The difference between the curves reveals the correlation dynamics in the unitary gas. The long-time power-law behaviour of $N_{\mathrm{obs}} \propto t_{\mathrm{hold}}^{-9/26}$ (dashed black line) corresponds to the loss expected for a *thermal* unitary Bose gas. Figure reproduced from [11,15].

out speed, and a much slower $1/\mathcal{R} = 5.8\,\mu\mathrm{s\,G}^{-1}$. We see that the curves coincide at both short and long t_{hold}: this reflects the fact that at early times, the correlations that lead to the creation of an atom-molecule mixture have not yet built up within the gas, and at long times these correlations break down again. Indeed, the long-time power-law behaviour of the fast-ramp data is consistent with the $N_{\mathrm{obs}} \propto t_{\mathrm{hold}}^{-9/26}$ expectation for a *thermal* rather than degenerate unitary gas.

Turning our attention to the kinetic energy of the gas, we show representative absorption images for several t_{hold} in Fig. 6.5(a). Initially, there is a dramatic increase in the population of high-k momentum states. At much later times, the central low-k population disappears, indicating that the sample heats and eventually becomes thermal. In Fig. 6.5(b) we show the evolution of the per-particle kinetic energy, shown here on log-log axes. We see a monotonic increase in E with time, and the long-time behaviour agrees with the thermal-gas energy scaling, $E \propto t_{\mathrm{hold}}^{2/13}$. This scaling comes from the temperature dependence in Eq. (6.7), assuming that

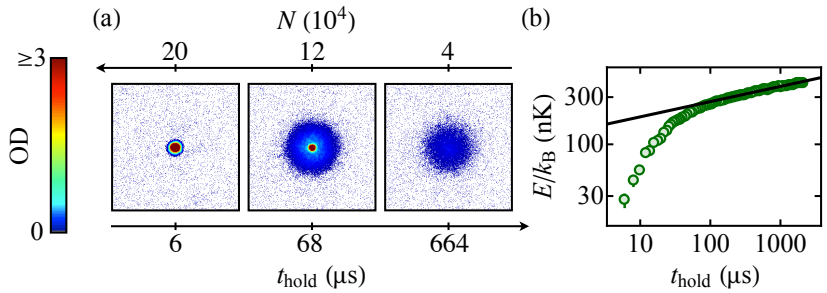

Figure 6.5 | **Growth of the kinetic energy in a Bose gas at unitarity.** The gas is initially degenerate and consists of $N_0 = 214 \times 10^3$ atoms. **(a)** Absorption images taken along the cylinder axis for various t_{hold} and after 12 ms of ToF expansion. **(b)** Kinetic energy per particle, E, as a function of t_{hold}. The per-particle interaction energy after the ramp out is $< k_{\mathrm{B}} \times 20\,\mathrm{nK}$. The solid line shows the expected $t_{\mathrm{hold}}^{2/13}$ power-law prediction for a thermal gas, where $E \propto T$. Figure reproduced from [15].

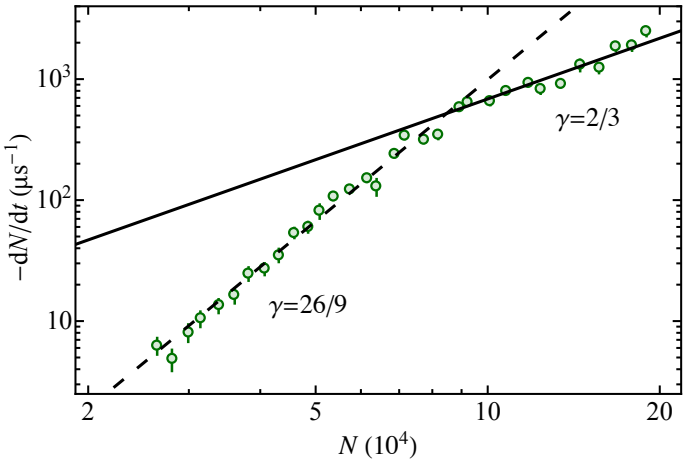

Figure 6.6 | **Atom-loss scaling laws.** We numerically differentiate our $N(t_{\mathrm{hold}})$ to obtain the instantaneous loss rate, plotted here as a function of atom number on log-log axes. Note that on this plot, t_{hold} increases as one moves to the left along the N axis. For these data, $N_0 = 214 \times 10^3$. The early-time dynamics clearly show the expected degenerate-gas $\gamma = 2/3$ scaling, while at later times there is a sharp crossover to the thermal-gas $\gamma = 26/9$ behaviour. Figure reproduced from [15].

$E \propto T$.

6.3.1 Universal loss dynamics

We shall now focus on the universal aspects of the atom-loss dynamics of the initially degenerate gas; we will return to the correlation dynamics in section 6.3.3. Here we use data taken with our fastest ramp-out speed, such that $N_{\mathrm{obs}} \approx N$. Since we would like to compare our data directly with Eq. (6.4), we numerically differentiate[15] our atom-loss curves, $N(t_{\mathrm{hold}})$, to obtain the instantaneous loss rate as a function of N. Fig. 6.6 shows a log-log plot of the extracted $\dot{N}$ versus N for $N_0 = 214 \times 10^3$; here t_{hold} increases as one moves to the left along the horizontal axis.

[15] Writing our $N(t_{\mathrm{hold}})$ as a set of time-ordered points $\{(t_i, N_i) : i = 1, 2, \dots\}$, we compute the derivatives by selecting the i^{th} and $(i+\delta i)^{\mathrm{th}}$ points. Then, we take the instantaneous loss rate at $N = \frac{1}{2}(N_i + N_{i+\delta i})$ to be $\mathrm{d}N/\mathrm{d}t = (N_{i+\delta i} - N_i)/(t_{i+\delta i} - t_i)$; typically we use $\delta i = 3$.

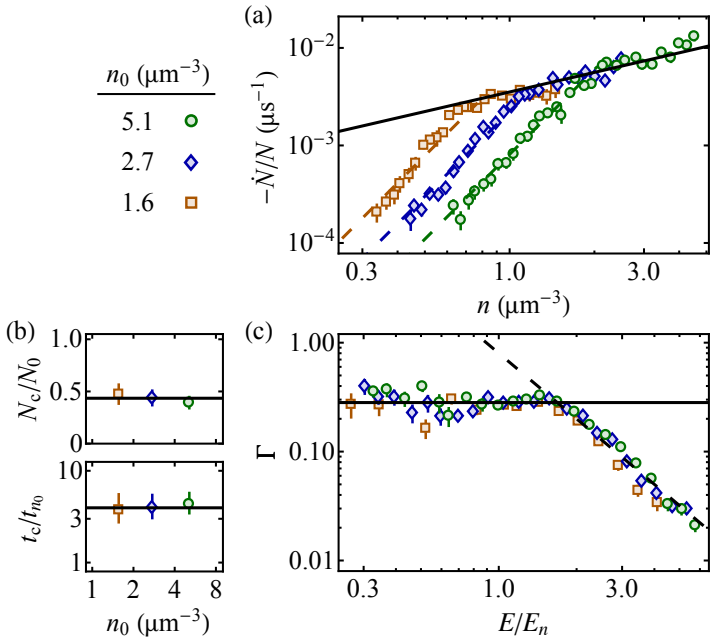

Figure 6.7 | **Universal crossover from a degenerate to a thermal unitary gas. (a)** The same $\gamma = 2/3$ law, $\dot{N}/N = -0.28/t_n$ (solid line) describes degenerate gases with different initial densities n_0. Dashed lines show the (separate) $\gamma = 26/9$ thermal unitary scaling laws for each n_0. **(b)** The crossover between degenerate- and thermal-gas behaviour occurs at the same N/N_0 and $t_{\mathrm{hold}}/t_{n_0}$ for all n_0; solid lines show the n_0-averaged values $N_c/N_0 = 0.43(4)$ and $t_c/t_{n_0} = 4.0(4)$. **(c)** Plotting the dimensionless loss rate Γ [Eq. (6.9)] against E/E_n against the collapses all our data onto a single universal curve with the crossover at $E_c/E_n = 1.7(2)$. The solid line is $\Gamma = 0.28$, and the dashed one shows the expected $\Gamma \propto (E_n/E)^2$. Figure reproduced from [11].

The large-N data (corresponding to small t_{hold}) clearly show the degenerate-gas $\gamma = 2/3$ behaviour, and as N decreases, we see a surprisingly sharp crossover to the thermal-gas $\gamma = 26/9$ power law.

In Fig. 6.7(a) we plot similar data for loss curves taken with different N_0, in order to explore the universal features of the crossover between the degenerate- and thermal-gas behaviour[16]. We see that these data follow the same pattern as in Fig. 6.6, and indeed all the degenerate-gas data lie along the same $\gamma = 2/3$ line. Writing $\dot{N}/N = -A/t_n$ as in Eq. (6.8), we obtain a value $A = 0.28(3)$; we assess that this could overestimate A by up to 0.04 due to the $< 10\,\%$ difference between N_{obs} and the actual N. For comparison, we extract a slightly lower value $A \approx 0.18$ using the ^{85}Rb data [210], which is consistent [182] with reported Efimov width parameters: for the $|1, 1\rangle$ state of ^{39}K that we use here, $\eta^* = 0.09(4)$ [207], and for the $|2, -2\rangle$ state of ^{85}Rb, $\eta^* \approx 0.057(2)$ [231].

We now turn our attention to the later-time thermal-gas behaviour of the three different-N_0 curves in Fig. 6.7(a). For all N_0, the data agree with (separate) $\gamma = 26/9$ power laws. We identify the point at which the behaviour crosses over between the degenerate- and thermal-

[16] Here we take into account slight variations in the trap volume that were not included in [15], plotting against n rather than N in Fig. 6.7(a,b).

gas cases; this always occurs at the same fraction of N_0, and at the same t_{hold} expressed in units of the initial-density Fermi time t_{n_0} [see Fig. 6.7(b)]. The combined data give $N_{\mathrm{c}} = 0.43(4)\,N_0$ and $t_{\mathrm{c}} = 4.0(3)\,t_{n_0}$.

In Fig. 6.7 we connect our measured atom-loss rates with the per-particle kinetic energy of the gas. We define the dimensionless per-particle loss rate

$$\Gamma = -t_n \dot{N}/N\,, \tag{6.9}$$

which corresponds to $\Gamma = A$ for the degenerate regime, and in the thermal regime $\Gamma \propto N^{4/3}/T^2 \propto (E_n/E)^2$ [c.f. Eq. (6.7), with $E \propto T$].

Fig. 6.7(c) shows Γ plotted against (E/E_n), with all our data collapsing onto a single universal curve that has the crossover at $E_{\mathrm{c}}/E_n = 1.7(2)$. For comparison, in an ideal Bose gas this energy corresponds to the rather high temperature $T \approx 3T_{\mathrm{c}}$, where T_{c} is the BEC critical temperature. In the unitary gas, on the other hand, we expect E/E_n to be of order unity even in the $T \to 0$ limit [178, 183–185]. These measurements do not distinguish between the correlation- and heating-related contributions [178, 188, 191, 192, 208] to the initial growth of E/E_n; for insight into this, we need to take a momentum-resolved approach.

6.3.2 Momentum-resolved dynamics

Now that we have an understanding of the N and E scaling laws, we next isolate the effects of the lossless post-quench dynamics by using measurements of the momentum distribution, n_k. Our protocol mirrors that in the previous section [see Fig. 6.8(a)], and we once again use our fastest ramp-out speed to minimise the conversion of atoms into molecules. We infer n_k using the same procedure as in section 5.3.1: we take line-of-sight–integrated absorption images along the axis of the cylindrical trap after expanding the cloud, average azimuthally, and use the inverse-Abel to recover the three-dimensional n_k. Our data have ≈ 20 experimental repetitions, over which we also average. Finally, we normalise n_k such that $\int \mathrm{d}k\, 4\pi k^2 n_k = 1$. The finite times of flight we use here mean that our n_k are not quantitatively reliable for $k \lesssim 2\,\mu\mathrm{m}^{-1}$.

We show our extracted n_k for several t_{hold} in Fig. 6.8(b). These curves all correspond to a fixed initial density of $n_0 = 5.1\,\mu\mathrm{m}^{-3}$. Fig. 6.8(c) highlights the main features of our experimental observations; each curve here corresponds to the evolution of the momentum density at a fixed momentum $\hbar k$. We identify three separate stages: a rapid initial growth, followed by a quasi-steady-state (dashed lines), and finally long-time heating. Interestingly, although the timescales of these processes are all $\sim t_{n_0}$, they are clearly k-dependent; this feature is common to $k/k_{n_0} \gtrsim 0.8$. For each k in this range, we identify the occupation at the plateau $\overline{n_k}$. We then use sigmoid fits to the (log-)data (solid lines) to extract the half-way rise time τ, defined by $n_k(k, \tau(k)) = \frac{1}{2}\overline{n_k}(k)$.

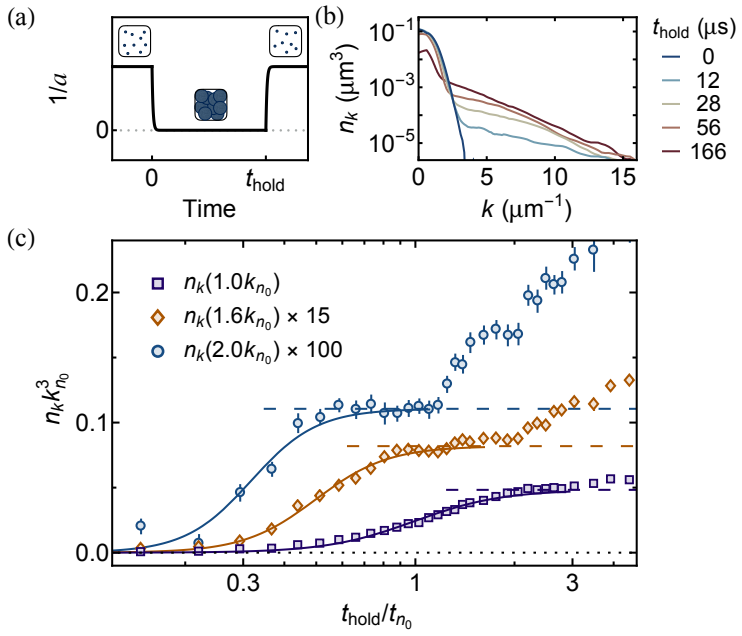

Figure 6.8 | **Momentum-resolved dynamics of a degenerate Bose gas quenched to unitarity. (a)** Quench protocol. Our fastest ramp-out speed ($1/\mathcal{R} = 0.3\,\mu\mathrm{s\,G^{-1}}$) ensures minimal conversion of atoms into molecules. **(b)** Momentum distribution n_k for different hold times t_{hold} spent in the unitary regime. The initial gas density is $n_0 = 5.1\,\mu\mathrm{m}^{-3}$, which sets the corresponding Fermi momentum $k_{n_0} = 6.7\,\mu\mathrm{m}^{-1}$ and Fermi time $t_{n_0} = 27\,\mu\mathrm{s}$. **(c)** Populations of individual k states as a function of t_{hold}. These show an initial period of rapid growth, followed by saturation at (quasi-)steady-state values (dashed lines), and heating at later times. We extract the initial-growth half-way times using sigmoid fits (solid lines). Figure reproduced from [16].

We emphasise the k dependence of the timescales: the $1.0\,k_{n_0}$ data reach their plateau region only after the $2.0\,k_{n_0}$ data have already begun to show the late-time heating. This illustrates why a quantitative separation of the lossless and recombination dynamics has been historically elusive. Here, instead, we separately extract $\overline{n_k}$ for different k in order to piece together the function $\overline{n_k}(k)$. This does not represent the physical distribution of momenta within the gas at any specific t_{hold}, but rather allows us to infer what the steady-state distribution would be in the absence of atom loss and heating. We assume that at early times (of order t_{n_0}) the non-zero k states are fed primarily from the BEC.

We plot the extracted $\tau(k)$ and $\overline{n_k}(k)$ for three different n_0 in Fig. 6.9, where all quantities have been rendered dimensionless using the Fermi scales. Within our experimental errors, all our data fall onto universal curves. Our data (within the experimentally accessible range of momenta) are consistent with the scaling $\tau/t_{n_0} \propto k_{n_0}/k$ at low k and $\tau/t_{n_0} \propto (k_{n_0}/k)^2$ at high k, scalings which have been predicted for the emergence of a prethermal steady state [181, 182, 186, 192, 232]. This picture has Bogoliubov-like excitations at short times after the quench: phonon-like excitations at low k and free-particle–like excitations at high k (c.f. section 2.8). For this prethermal case, the mean-field energy of the weakly interacting theory is replaced by

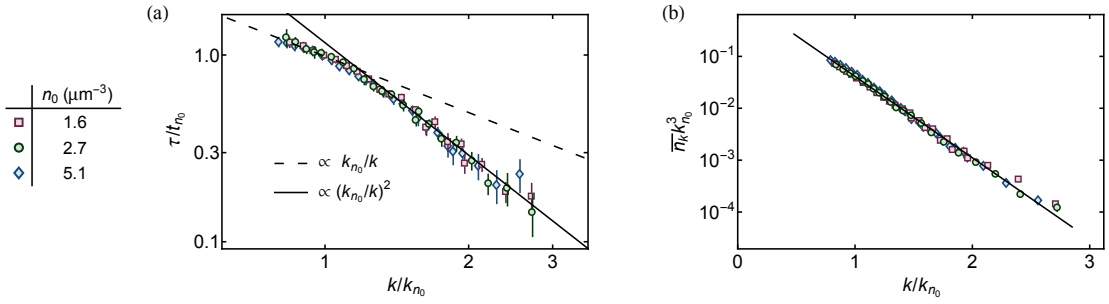

Figure 6.9 | Universal post-quench dynamics and steady-state momentum distribution in the degenerate Bose gas. We plot **(a)** the half-way rise time $\tau(k)$, and **(b)** the inferred steady-state $\overline{n_k}(k)$, for three different n_0. Using the Fermi scales to express all quantities in dimensionless form collapses all our data onto universal curves. The solid line in **(b)** corresponds to $\overline{n_k}k_{n_0}^3 = 1.53\exp(-3.62\,k/k_{n_0})$. Figure reproduced from [16].

an energy of order E_{n_0}, the speed of sound is of order $\hbar k_{n_0}/m$, and the crossover between the different k regimes happens at $k \sim k_{n_0}$. Finally, $\tau(k)$ is related to the dephasing time, given approximately by the inverse excitation energy.

Turning now to $\overline{n_k}$, we see that over three orders of magnitude our data are well captured by an exponential, $\overline{n_k}k_{n_0}^3 = A\exp(-Bk/k_{n_0})$, and we extract the fit parameters $A = 1.53(3)$ and $B = 3.62(2)$. At face value, this previously unanticipated form implies a finite condensed fraction of $\eta = 1 - \int \mathrm{d}k\, 4\pi k^2 \overline{n_k} = 19(4)\,\%$. Our data do not feature the asymptotic $n_k \sim 1/k^4$ form expected at high k [233], but this does not affect our qualitative conclusion; η would change by less than 3 % if n_k were to change to this slower-decaying form beyond our experimental k range. Our estimate of η is close to predictions for the prethermal state [181, 182, 186, 192, 232], and we see qualitative similarities between our $\overline{n_k}$ and the theoretical calculations for $k \lesssim k_n$. Emerging theoretical work [234] suggests that non-integrable three-particle processes may lead to the exponential form we observe for $k \gtrsim k_n$, rather than the previously held expectation of $1/k^4$.

6.3.3 Correlation dynamics

Let us now shift our focus to the dynamics of correlations at unitarity. We probe the correlations indirectly: we define ΔN to be the reduction in N_{obs} due to a slow ramp out (i.e., converting some atoms to molecules), relative to our fastest $1/\mathcal{R} = 0.3\,\mu\mathrm{s\,G^{-1}}$, and study its dynamics as a function of t_{hold}. These $\Delta N(t_{\mathrm{hold}})$ are shown in Fig. 6.10(a) for three different N_0, using the same (slow) ramp out speed $1/\mathcal{R} = 5.8\,\mu\mathrm{s\,G^{-1}}$. We rescale these same data in Fig. 6.10(b), plotting the fractional $\Delta N/N$ against the dimensionless[17] $t_{\mathrm{hold}}/t_{n_0}$; we also include an additional data series with a different $\mathcal{R}$. This aligns all our data horizontally, and apart from their heights

[17] We use the Fermi scales for the *initial* density when normalising our data, since the relevance of t_n is not *a priori* clear once the clouds have significant thermal character.

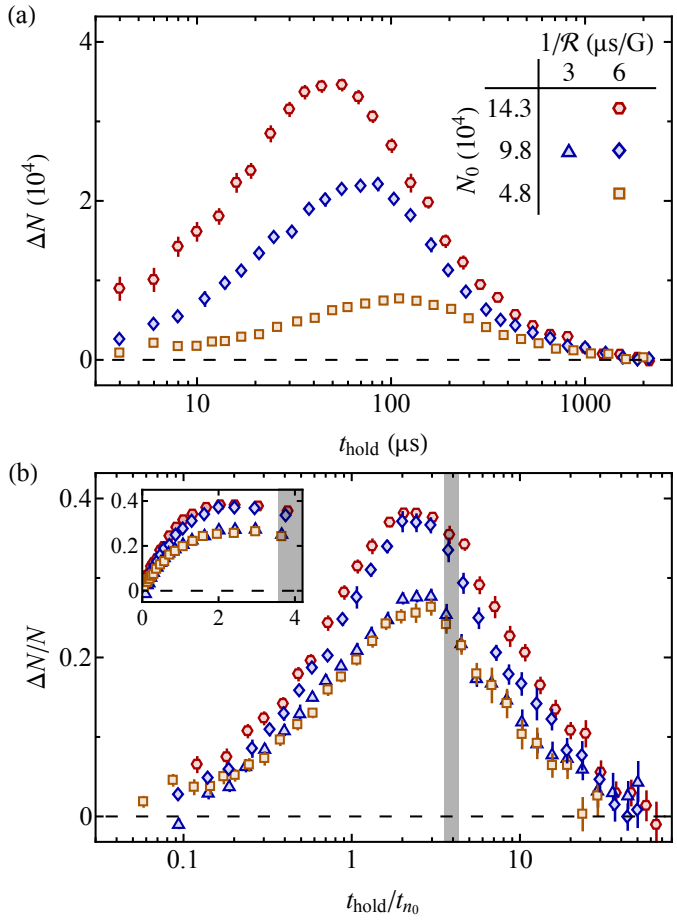

Figure 6.10 | **Correlation dynamics of a degenerate Bose gas quenched to unitarity.** We probe the correlations indirectly by measuring ΔN, which is a measure of the number of molecules created during the ramp out from unitarity. **(a)** We plot $\Delta N(t_{\mathrm{hold}})$ for different N_0, but the same slow ramp-out speed $1/\mathcal{R} = 5.8\,\mu\mathrm{s\,G}^{-1}$; the legend applies to both panels. **(b)** Plotting $\Delta N/N$ against the dimensionless $t_{\mathrm{hold}}/t_{n_0}$ shows the universal nature of the correlation dynamics. The grey shaded region corresponds to the crossover time $t_c/t_{n_0} = 4.0(4)$. We highlight the quasi-equilibrium reached for $t_{\mathrm{hold}} < t_c$ in the inset by replotting the data with a linear horizontal scale. Figure reproduced from [15].

all the curves look essentially the same, confirming that the initial gas density universally determines the correlation dynamics.

The non-monotonic shape of the $\Delta N(t_{\mathrm{hold}})$ curves can be qualitatively understood by considering two competing effects. Firstly, it takes time $(\sim t_{n_0})$ for correlations to develop after the interaction quench. Then, at long times, the correlations are lost again as the gas heats and the phase-space density decreases (see also [229,235]).

We note that Fig. 6.10(b) uses a log scale for the $t_{\mathrm{hold}}/t_{n_0}$ axis. In the inset, we plot these same data using a linear horizontal axis instead, in order to emphasise that the fractional $\Delta N/N$ becomes essentially flat well before the crossover time $t_c/t_{n_0} = 4.0(4)$. This implies that the system reaches a quasi-equilibrium while it remains degenerate; in our homogeneous system this implies a *global* (quasi)equilibrium (c.f. [208]).

Non-trivial dependence of the peak height $\Delta N/N$ could be a sign of Efimov trimer produc-

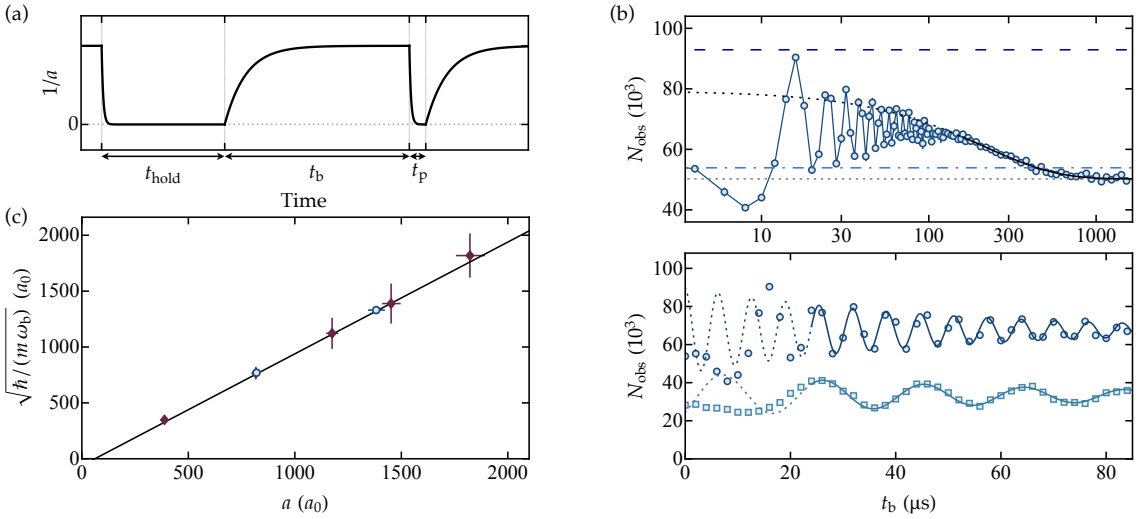

Figure 6.11 | **Double-quench method for measuring the Feshbach-dimer binding energies. (a)** Quench protocol (following [230]), showing an initial period t_{hold} during which correlations build, followed by a period of evolution at finite a, t_{b}, and a second, short pulse to unitarity of length $t_{\mathrm{p}} = 8\,\mu\mathrm{s}$. **(b)** *Upper*: Observed atom number N_{obs} as a function of t_{b}, showing oscillations due to the energy difference between the atomic and Feshbach-dimer states. We show for comparison the total measured atom number at $t_{\mathrm{b}} = 0$ using fast (dashed line) and slow (dash-dotted line) ramps out, as well as the $t_{\mathrm{b}} \to \infty$ limit (dotted line) of an exponential fit to the long-t_{b} data (solid line). These data have $N_0 = 144 \times 10^3$, $a = 820\,a_0$ between the pulses, and $t_{\mathrm{hold}} = 60\,\mu\mathrm{s}$. *Lower*: A zoom in on the early-time dynamics, showing the damped sinusoidal fits to the data, which we use to extract the oscillation frequency ω_{b}. The light-blue squares show similar data, but with $a = 1380\,a_0$, $N_0 = 50 \times 10^3$, and $t_{\mathrm{hold}} = 64\,\mu\mathrm{s}$. **(c)** The extracted values of ω_{b} are consistent with the theoretically-expected $\propto 1/(a - \bar{a})^2$ dependence of the dimer binding energy (solid line). We show additional frequency measurements (red points) obtained using an rf-association technique [239]. Figure courtesy C. Eigen.

tion, and a corresponding breakdown of universality. Based on observations with ^{85}Rb [210], we believe it is likely that our post-quench gas contains Efimov trimers in the first excited state, in addition to Feshbach dimers. The $\approx 1\,\mu\mathrm{m}$ on-resonance size of this state could set a scale separating "small" densities from "large" ones [35, 236–238]. In general, a quantitative understanding of the correlation dynamics remains an interesting open problem for future work.

6.3.4 Binding energy of Feshbach dimers

We now take a brief aside to discuss the energies of Feshbach dimers, following the approach in [230]. In Fig. 6.11(a) we show our double-quench protocol. Here, rather than probing the unitary regime itself, we are simply using it as a tool to develop correlations in the gas over a period t_{hold}, which subsequently result in the formation of molecules during a slow ramp back out of the unitary regime. We allow the atom-molecule mixture to evolve for time t_{b} at finite a, before applying a second, short interaction-strength pulse of duration t_{p} back into the unitary regime. We then image the cloud as in the previous sections of this chapter and measure N_{obs}.

We plot N_{obs} against the between-pulse time t_{b} in the upper panel of Fig. 6.11(b). Here we have used a scattering length $a = 820\,a_0$ between the unitary pulses; the gas has $N_0 = 144 \times 10^3$, $t_{\mathrm{hold}} = 60\,\mu\mathrm{s}$, and $t_{\mathrm{p}} = 8\,\mu\mathrm{s}$. The data show a clear oscillation, which corresponds to the energy difference between the atomic and Feshbach-dimer states, that decays over $\approx 100\,\mu\mathrm{s}$ (note the log scale on the horizontal axis). The horizontal lines mark various limits for N_{obs}. The uppermost, dashed line corresponds to N (i.e., using a fast ramp out) with $t_{\mathrm{b}} = 0$, where we effectively have a single quench of length $t_{\mathrm{hold}} + t_{\mathrm{p}} = 68\,\mu\mathrm{s}$. The dash-dotted line corresponds to N_{obs} (i.e., using a slow ramp out) for the same $t_{\mathrm{b}} = 0$. The dotted (horizontal) line corresponds to the $t_{\mathrm{b}} \to \infty$ limit of an exponential fit to the long-t_{b} data (solid black line); this differs from the dash-dotted slow-ramp data by $< 10\,\%$, and for lower-N data these two agree perfectly.

In the lower panel of Fig. 6.11(b) we replot the early-time data on a linear time axis (dark-blue circles) and also show similar data (light-blue squares) with $a = 1380\,a_0$, $N_0 = 50 \times 10^3$, $t_{\mathrm{hold}} = 64\,\mu\mathrm{s}$, and $t_{\mathrm{p}} = 8\,\mu\mathrm{s}$. We fit these data with a damped sinusoidal oscillation $\propto \exp(-t_{\mathrm{b}}/\tau)\sin(\omega_{\mathrm{b}} t_{\mathrm{b}} + \varphi)$ (solid lines) to extract the oscillation frequency ω_{b}, neglecting the early times (dashed lines) for which the B field has not yet reached its steady-state value.

In section 2.5 we gave the dimer binding energy as $\hbar\omega_{\mathrm{b}} = \hbar^2/(m[a - \bar{a}]^2)$. Rearranging, we have

$$\sqrt{\frac{\hbar}{m\omega_{\mathrm{b}}}} = a - \bar{a}\,, \tag{6.10}$$

such that plotting $\sqrt{\hbar/(m\omega_{\mathrm{b}})}$ against a should give a straight line. Fig. 6.11(c) shows exactly this plot using the frequencies from Fig. 6.11(b), along with similar frequency data we have obtained using rf association (e.g., [239], red diamonds). Both methods give frequencies consistent with the theoretical prediction using the value $\bar{a} \approx 61.2\,a_0$ corresponding to our internal state.

6.4 Thermal Bose gases quenched to unitarity

In this section we turn from degenerate gases to thermal ones. Here we benefit from the simplification that, although both the lossless and recombination dynamics are slowed down compared to the degenerate gas, the three-body recombination is slowed down more [179,206,207], leading to a better separation of the two timescales. For instance, we can now identify an intermediate plateau region in the evolution of the per-particle kinetic energy, $E(t_{\mathrm{hold}})$, shown in Fig. 6.12(a), separating the rapid initial growth for $t_{\mathrm{hold}} \lesssim 100\,\mu\mathrm{s}$ from the later-time heating; the later-time dynamics match the recombination-heating theory [206] (see section 6.1.1). The shape of the $E(t_{\mathrm{hold}})$ curve now directly displays the two-stage dynamics that only became

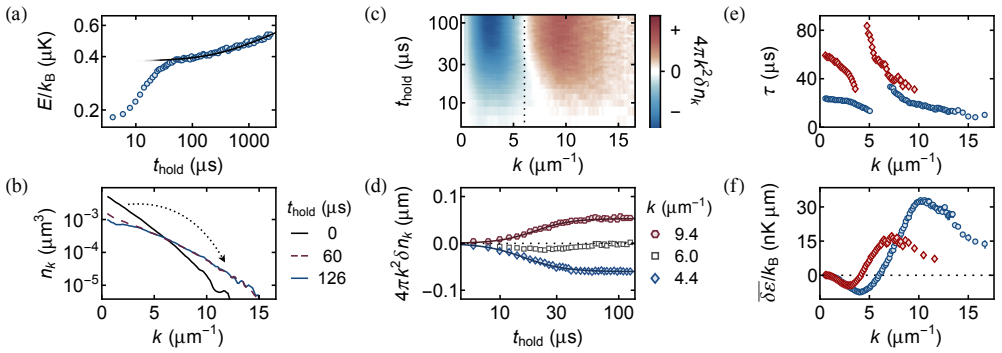

Figure 6.12 | Dynamics of a thermal Bose gas quenched to unitarity. The initial gas density and temperature in **(a)-(d)** are $n = 5.6\,\mu\text{m}^{-3}$ and $T = 150\,\text{nK}$. **(a)** The rapid initial growth ($t_{\text{hold}} \lesssim 100\,\mu\text{s}$) of the per-particle kinetic energy E is separated from the heating stage at $t_{\text{hold}} \gg 100\,\mu\text{s}$. The solid line is the prediction for recombination heating. **(b)** Momentum distribution n_k for selected hold times at unitarity. The distribution reaches a quasi-steady state in the first $\approx 60\,\mu\text{s}$; we measure an almost identical distribution at $t_{\text{hold}} = 126\,\mu\text{s}$. **(c)** Changes in population, $4\pi k^2\delta n_k$, as a function of k and t_{hold}. The population remains essentially constant for $k_0 = 6.0\,\mu\text{m}^{-1}$. **(d)** Fixed-$k$ cuts through the plot in **(c)**. Solid lines are sigmoid fits for extracting the half-way rise times $\tau(k)$. **(e, f)** Extracted τ and change in the spectral energy density, $\overline{\delta\varepsilon}(k) \propto k^4\overline{\delta n_k}$ (between the pre-quench and steady states). The blue data have $n_0 = 5.6\,\mu\text{m}^{-3}$ and $T = 150\,\text{nK}$; the additional red data have $n_0 = 1.3\,\mu\text{m}^{-3}$ and $T = 70\,\text{nK}$. Figure reproduced from [16].

apparent for the degenerate-gas case after resolving the dynamics in k (e.g., Fig. 6.8).

We focus now on the early-time dynamics, for $t_{\text{hold}} \lesssim 100\,\mu\text{s}$. As seen in Fig. 6.12(b), this suffices to extract the intermediate steady-state properties across our whole k range, since n_k is almost identical for $t_{\text{hold}} = 60\,\mu\text{s}$ and $t_{\text{hold}} = 126\,\mu\text{s}$. In the degenerate-gas case, we made the assumption that the macroscopically occupied BEC acts as the primary source of particles for the growth of all other k modes. Now considering the thermal gas, even before the quench to unitarity, there is a significant population in k states up to the thermal-wavelength scale, i.e., n_k is substantial for all $k \lesssim 1/\lambda$. We therefore look at the redistribution of particles in k space in terms of the change $\delta n_k(k)$ with respect to $t_{\text{hold}} = 0$ and the corresponding change $\delta\varepsilon$ in the spectral energy density, $\varepsilon = \hbar^2/(2m) \times 4\pi k^4 n_k$.

We plot the time-resolved population changes, $4\pi k^2\delta n_k$, as a function of k and t_{hold} in Fig. 6.12(c). One sees that there is a special momentum k_0 for which the population does not change appreciably for $t_{\text{hold}} \lesssim 100\,\mu\text{s}$, and which divides the k domain into regions with decreasing (blue) and increasing (red) populations. Fig. 6.12(d) shows vertical cuts through the data from Fig. 6.12(c), for $k = k_0$, and a representative k value from each of the depletion and growth regions. We fit sigmoids to these data for all k where we can clearly identify that the population either grows or declines, and use the fits to extract half-way rise times $\tau(k)$ and the steady-state $\overline{\delta\varepsilon}(k)$. Near k_0, where $4\pi k^2\delta n_k$ is small for all t_{hold}, we cannot assign a corresponding τ.

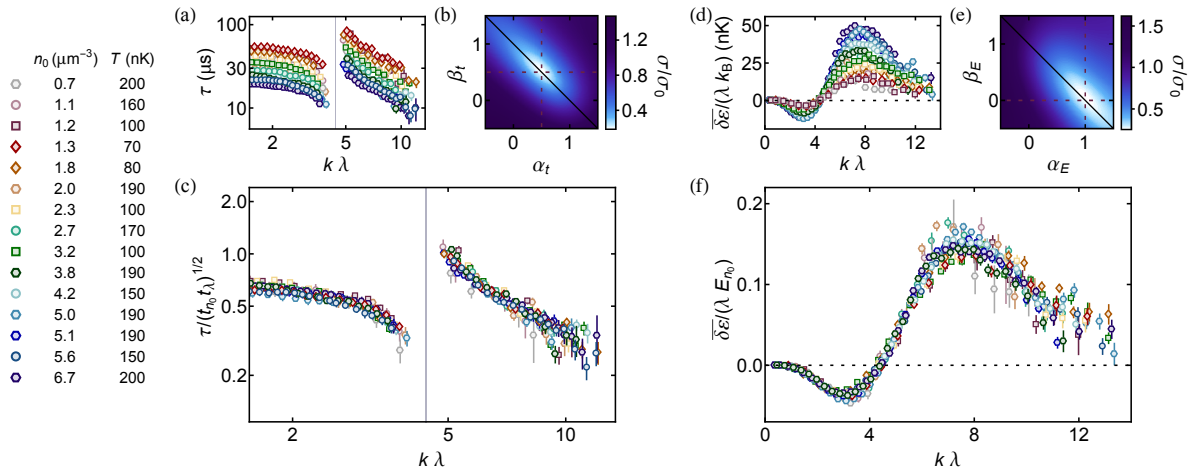

Figure 6.13 | **Universal functions for the thermal Bose gas quenched to unitarity. (a, d)** Plotting τ and $\overline{\delta\varepsilon}$ as functions of $k\lambda$ horizontally aligns our data for 15 different combinations of n_0 and T. **(b, e)** Assuming the scaling forms $t_s \sim t_{n_0}^{\alpha_t}$ and $E_s \sim E_{n_0}^{\alpha_E}(k_B T)^{\beta_E}$ for the characteristic time and energy scales respectively, we optimise the exponents to best collapse our data. We find $\alpha_t \approx \beta_t \approx \frac{1}{2}$, and $\alpha_E \approx 1$ and $\beta_E \approx 0$. **(c, f)** The dimensionless $\tau/\sqrt{t_{n_0} t_\lambda}$ and $\overline{\delta\varepsilon}/(\lambda E_{n_0})$ are universal functions of $k\lambda$ to within the experimental scatter. Figure reproduced from [16].

We plot the extracted $\tau(k)$ and $\overline{\delta\varepsilon}(k)$ in Fig. 6.12(e, f), for two different combinations of n and T. The $\overline{\delta\varepsilon}(k)$ curve conveys both the redistribution of particles from $k < k_0$ (where $\overline{\delta\varepsilon} < 0$) to $k > k_0$ ($\overline{\delta\varepsilon} > 0$), as well as the total per-particle energy $\overline{\Delta E}$ deposited during the $t_{\text{hold}} \lesssim 100\,\mu\text{s}$ dynamics, given by the area under the curve $\overline{\Delta E} = \int \mathrm{d}k\, \overline{\delta\varepsilon}$.

6.4.1 Universal laws for the redistribution of momenta

We now empirically investigate whether the $\tau(k)$ and $\overline{\delta\varepsilon}(k)$ curves can be scaled to give universal dimensionless functions. We find that the natural scale for k is independent of n_0, and given simply by $1/\lambda$ [11], where we evaluate λ for the pre-quench T. In Fig. 6.13(a, d) we plot τ and $\overline{\delta\varepsilon}/\lambda$ against $k\lambda$, for 15 different combinations of n_0 and T; we include the additional factor of $1/\lambda$ when plotting $\overline{\delta\varepsilon}$ in order to preserve the integral $\overline{\Delta E}$. We see horizontal alignment of the curves in both cases, and identify the dimensionless $k_0\lambda = 4.40(2)$.

It remains to determine whether these curves can be collapsed vertically; since they are in general dependent on both n_0 and T, we have two possible timescales, and two possible energy scales to consider in the process. We introduce a general scaling time $t_s(n_0, T)$ and energy $E_s(n_0, T)$, and assume scaling forms $t_s \propto t_{n_0}^{\alpha_t} t_\lambda^{\beta_t}$ and $E_s \propto E_{n_0}^{\alpha_E}(k_B T)^{\beta_E}$, with $t_\lambda = \hbar/(k_B T)$. To determine the $\alpha_{\{t,E\}}$ and $\beta_{\{t,E\}}$ that best collapse the data, we evaluate the standard deviation across all 15 combinations of n and T at fixed $k\lambda$, and integrate over our full $k\lambda$ range to give the figure of merit σ. We normalise σ by its value in the absence of any scaling, which we denote σ_0. Our analysis treats $\alpha_{\{t,E\}}$ and $\beta_{\{t,E\}}$ as independent, however on dimensional grounds we expect $\alpha_t + \beta_t = \alpha_E + \beta_E = 1$.

Fig. 6.13(b, e) shows the results of our analysis. For the t_s scaling, we find that $\alpha_t \approx \beta_t \approx \frac{1}{2}$ corresponds to the minimum of σ, suggesting that $t_s = \sqrt{t_{n_0} t_\lambda}$. For the E_s scaling, we find $\alpha_E \approx 1$ and $\beta_E \approx 0$ minimises δ, corresponding to $E_s = E_{n_0}$. Fig. 6.13(c, f) shows the data from Fig. 6.13(a, d) scaled according to these results, and we see that these time- and energy scales do indeed collapse our data onto universal dynamic and thermodynamic functions.

We interpret the t_s scaling as follows. Since the particles do not overlap in a thermal gas, in order to feel the unitary interactions following the quench, they must first meet. The characteristic time until this meeting takes place is given by the ratio of the interparticle spacing $n_0^{-1/3}$ to the characteristic thermal velocity $\hbar/(m\lambda)$, such that $t_s \propto n_0^{-1/3}\lambda \propto \sqrt{t_{n_0} t_\lambda}$, in agreement with our empirical result.

The E_s scaling is rather unexpected: it implies that although $\overline{\delta\varepsilon}(k)$ depends on both n_0 and T, its integral is no longer T-dependent. The lack of T dependence suggests that the thermal-gas $\overline{\Delta E}/E_{n_0}$ should be equal to the degenerate-gas $\overline{E}/E_{n_0}$ (c.f. section 6.3.2). From the data in Fig. 6.13(f) we estimate $\overline{\Delta E}/E_{n_0} = 0.7(1)$, bearing in mind that we do not observe the very-high-k tails (for $k\lambda \gtrsim 12$) of the distribution. The exponential form of $\overline{n_k} k_{n_0}^3$ in Fig. 6.9(b) gives a consistent $\overline{E}/E_{n_0} = 0.74(4)$.

6.5 Conclusion

We have presented here comprehensive studies of a Bose gas quenched to unitarity. Using both thermal and degenerate gases, we have characterised the particle-loss, energy, and correlation dynamics in the gas. For the degenerate gas in particular, by examining the dynamics in a momentum-resolved fashion we were able to separate the lossless dynamics from the dissipative ones. This allowed us to identify a steady-state distribution that has a condensed fraction $\approx 20\,\%$. For the thermal gas, we identified universal functions for the dynamics and thermodynamics of the gas. Our experiments provide quantitative benchmarks and raise new questions for the theory of unitary Bose gases.

In the future, it would be interesting to explore the composition of the atom-molecule mixtures that we form, including both dimer and Efimov trimer states, as well as the dependence of the composition on the initial gas density. This may provide deeper insight into the elusive Efimov trimers, for which theorists have predicted the exciting possibility of a novel molecular superfluid state [175].

7 Outlook

In the previous three chapters, we discussed a number of interesting aspects of the out-of-equilibrium homogeneous Bose gas. In doing so we have spanned the range of repulsive interactions, moving progressively further away from the relative comfort of the weakly interacting, equilibrium Bose gas. Our three-body-recombination cooling study in chapter 4 assumed that displacements from equilibrium were infinitesimal, and we showed that the effect is expected in the weakly interacting limit, with $na^3 \lesssim 10^{-7}$. Our study of bidirectional dynamic scaling in chapter 5 saw us increase the gas parameter into the range $1.5 \times 10^{-7} \lesssim na^3 \lesssim 8 \times 10^{-5}$, and explicitly required that we prepare the gas in a far-from-equilibrium initial condition; here we could nevertheless readily calculate what the corresponding new equilibrium would be. Finally, our experiments on the unitary Bose gas took us into the unfamiliar and exotic strongly interacting regime with $na^3 \gtrsim 1$.

We now take a step back, and outline a few possible future research avenues that share similar themes with the projects we have discussed in this thesis.

Interaction shift of the critical temperature. At weak-to-moderate interaction strengths in a homogeneous Bose gas, condensation is believed to occur at a lower phase-space density than the ideal-gas critical value of 2.612 [39]. Mean-field theory offers a qualitative explanation for this: since there is no exchange interaction for Bose-condensed atoms, an atom can lower its interaction energy by leaving the thermal fraction of the cloud in favour of the condensate. Mean-field theory is, however, unable to make quantitative predictions for the corresponding shift in the critical temperature in a homogeneous gas, since it incorrectly predicts that the BEC transition will be first order. After several decades of debate [240–243], a general consensus has been reached that the beyond-mean-field T_c shift at constant density n is given by

$$\frac{\Delta T_c}{T_c^0} \approx 1.8 \frac{a}{\lambda} . \tag{7.1}$$

Whilst a beyond-mean-field contribution has been seen indirectly in harmonically trapped Bose gases [244], our experimental platform is a promising setting for observing this shift directly. We note, however, that any residual curvature of the trapping potential produces a shift of opposite sign. It is therefore possible that our $\sim r^{15}$ potential will not suffice for measuring shifts of typically only a few percent. To that end, we are considering the installation of a digital micromirror device to (partially) replace our phase spatial light modulator. This has potential

for both the improved trap-wall resolution needed for precision T_c-shift measurements, but also offers the exciting possibility for moveable trap walls (at up to $\approx$ kHz frequencies).

Molecular spectroscopy and Efimov physics. We are exploring spectroscopic techniques (e.g. [230, 239]) for probing molecules and/or creating them using rf association from the continuum. We hope to use these techniques to study Efimov trimers. In the context of the unitarity experiments we presented in this thesis, we would like to have more technical flexibility and control over the B-field ramps that we use to enter and leave the unitary regime. We have plans to develop control electronics that directly feed back on the current flowing through the fast auxiliary coils. Here the main challenge is timescales, since we require $\approx 1\,\mathrm{MHz}$ bandwidth for the feedback circuitry. Ideally, these driving electronics could serve to create both top-hat pulses in the magnetic field, as well as a relatively flat-response amplifier for sinusoidal signals from DC through $\approx 1\,\mathrm{MHz}$. In addition, we would like to develop a method for directly imaging any molecules that we create; this is in contrast to the methods we have described in this thesis, where we detect the molecules' absence.

Dimensionality. The quasi-2D ^{39}K experiment in our research group also offers some exciting prospects with connections to the work we have discussed in this thesis. In terms of non-thermal fixed points, experiments in 2D have access to the defects (i.e. vortices) that are formed in a strong cooling quench, which would offer a fresh perspective on the physics. Not only would experiments with a 2D gas bridge the gap between our 3D experiments and the 1D gases [119, 146], but the shift from the second-order BEC transition to the infinite-order Berezinskii–Kosterlitz–Thouless transition could have an interesting effect on the non-thermal–fixed–point dynamics.

Appendix A

GPU-based GPE integrator

Both the dynamics of a condensate [22], as well as other highly occupied momentum states [155], can be described using the Gross–Pitaevskii equation (GPE):

$$i\hbar\frac{\partial\psi}{\partial t} = \underbrace{-\frac{\hbar^2}{2m}\nabla^2}_{\hat{H}_{\text{kin}}}\psi + V\psi + \frac{4\pi\hbar^2 a}{m}|\psi|^2\psi\,. \tag{A.1}$$

Here we outline a method for integrating this equation efficiently for three-dimensional problems.

Implementation

We discretise ψ on a three-dimensional grid of typically 128^3 points, with single-precision floating-point values for each of the real and imaginary parts of ψ at each point. Starting from a known state $\psi(\mathbf{r}, t)$, it is our goal to determine $\psi(\mathbf{r}, t+\Delta t) = \psi(\mathbf{r}, t) + \Delta\psi(\mathbf{r}, t)$. We evaluate the increment $\Delta\psi(t)$ using a Runge–Kutta (RK) method [245]. Specifically, we use the so-called "classic" or fourth-order RK method, which boasts single-step errors $\sim \Delta t^5$, and a total accumulated error $\sim \Delta t^4$. The method may be summarised as follows. Denoting $\psi'(t,\,\psi) = \partial\psi/\partial t$ from Eq. (A.1), one can define four successive approximations to the rate of change of ψ within the time interval from t to $t+\Delta t$, namely:

$$K_1 = \psi'(t, \psi)\,, \tag{A.2a}$$

$$K_2 = \psi'(t + \tfrac{1}{2}\Delta t, \psi + \tfrac{1}{2}\Delta t K_1)\,, \tag{A.2b}$$

$$K_3 = \psi'(t + \tfrac{1}{2}\Delta t, \psi + \tfrac{1}{2}\Delta t K_2)\,, \quad \text{and} \tag{A.2c}$$

$$K_4 = \psi'(t + \Delta_t, \psi + \Delta t K_3)\,. \tag{A.2d}$$

Here, each of the K_i, as for ψ itself, are functions of $(\mathbf{r},\,t)$. Finally, we set

$$\psi(\mathbf{r},\,t+\Delta t) = \psi(\mathbf{r},\,t) + \tfrac{1}{6}(K_1 + 2K_2 + 2K_3 + K_4)\,. \tag{A.3}$$

We note that the kinetic-energy term $\hat{H}_{\text{kin}}$ of Eq. (A.1) is diagonal in the momentum basis, but the remaining potential and interaction terms are diagonal in the position basis. It is therefore computationally advantageous to evaluate them separately in their natural bases by

transforming ψ between the position and momentum bases with a Fourier transform. We must perform one forward- and one inverse-Fourier transform for each of the K_i. The eight total transforms are the most computationally expensive part of evaluating the increment Δt, but these operations are also highly parallelisable. We therefore perform the full evolution on a graphics processor (GPU), which is by design better suited to parallelisable problems than the central processing unit. Optimised libraries for evaluating Fourier transforms with NVIDIA GPUs are available in the NVIDIA CUDA toolkits.

Our GPE-integration code is available at https://github.com/jakeglidden/gpu_gpe.git.

Imaginary-time evolution

If we choose to integrate Eq. (A.1) with an imaginary timestep $\Delta t \to i\Delta t$, it then describes the decay of ψ. In imaginary-time evolution, excitations decay at a rate proportional to their energy, and so ψ asymptotically approaches the system ground state, although the wavefunction amplitude also decreases as the time advances further along the imaginary axis. Renormalising ψ after each timestep prevents the wavefunction tending to zero, allowing us to extract the ground-state wavefunction.

Appendix B

Bragg techniques

Here we provide additional information about possible applications of the Bragg spectroscopy available on our experiment (see section 3.3.3). We first highlight techniques that have been used in the research group previously, and are potentially relevant for future extensions of the work in this thesis, before outlining our own idea for a Bragg thermometer.

Measurement of the correlation function. Bragg techniques can be used to measure the first-order correlation function $g^{(1)}(r)$, as was done in [116], inspired in turn by [162]. The supplementary information accompanying [116] explains the method in detail. The basic idea is to use a short Bragg pulse to create a small "copy" of the cloud that moves along the Bragg axis. The short pulse length ensures a broad frequency span, so that all k modes of the gas are effectively on resonance. We then wait for a short time t, while the moving "copy" cloud shifts by a distance $x = \hbar q t/m$, where q is the momentum imparted by the Bragg pulse. A second Bragg pulse is then applied, which causes the "main" and "copy" clouds to interfere with one another. Finally, the Bragg-diffracted atoms are allowed to fully separate from the main cloud.

The fraction of diffracted atoms is then

$$\frac{N_r}{N} = \frac{1}{2}\left[1 + \left(1 - \frac{x}{L}\right) g^{(1)}(x)\right] \sin^2\theta\,, \tag{B.1}$$

where L is the trap length along the Bragg axis, and θ is the area of each Bragg pulse (in the sense that $\theta = \pi$ corresponds to a complete transfer of atoms from the stationary "main cloud" into the moving "copy"). This result assumes that the separation $x < L$.

Resolving the condensed and thermal components. Our box-trap experiment features a homogeneous gas density, and excellent overlap between the thermal and Bose-condensed components. A small drawback, however, is that the momentum distribution of a saturated thermal cloud (i.e. exactly at $T = T_c$) has the form

$$n_k = \frac{V}{(2\pi)^3} \frac{1}{\exp[\hbar^2 k^2/(2mk_B T)] - 1} \tag{B.2}$$

$$\underset{k\to 0}{\approx} \frac{V}{(2\pi)^3} \frac{2mk_B T}{\hbar^2 k^2}\,, \tag{B.3}$$

which diverges as k^{-2} for $k \to 0$. Unfortunately, this is exactly the k-region where a BEC forms,

and so it can be difficult to resolve the two gas components in momentum space (a peak on top of another peak).

Ref. [246] offers a possible solution: again the paper's accompanying supplementary information is very useful. To separate the condensed and thermal components, the authors switch off the interactions between atoms, then apply a resonant Bragg pulse. The effective momentum width of the Bragg pulse (set by the intensity of the light) is chosen to coincide with the momentum width of the condensed component. Then, for a pulse of area $\theta = \pi$, they find that the majority ($\gtrsim 95\,\%$) of the condensed component is diffracted and begins to move along the Bragg axis. A measurement can then be performed once the two components have separated.

Bragg thermometry. Here we apply an approach similar to above, but we will be addressing a slightly different question. We consider a partially condensed 3D homogeneous Bose gas, and we focus on its momentum distribution along the x axis, i.e., after having integrated over the y and z directions. The Bose-condensed and thermal components of the gas have unity-normalised momentum distributions

$$n_{\mathrm{BEC}}(k_x) = \frac{1}{2\pi}\left[\frac{\sin(k_x L/2)}{(k_x L/2)}\right]^2, \quad \text{and} \tag{B.4}$$

$$n_{\mathrm{th}}(k_x) = \frac{-\lambda}{2\pi\zeta(\frac{3}{2})}\log\left[1-\exp\left(\frac{(\lambda k_x)^2}{4\pi}\right)\right] \tag{B.5}$$

respectively, assuming a fully Thomas–Fermi density distribution for the condensate. Here L is the trap length, λ is the thermal wavelength, and $\zeta(\frac{3}{2}) \approx 2.612$ is a value of the Riemann zeta function. Assuming a thermal fraction $\overline{\eta}$ with arbitrary (but known) dependence on the temperature T, the combined density distribution is then

$$n_{\mathrm{tot}}(k_x) = \overline{\eta}\, n_{\mathrm{th}}(k_x) + (1-\overline{\eta})\, n_{\mathrm{BEC}}(k_x)\,. \tag{B.6}$$

During a Bragg pulse, atoms undergo Rabi oscillations between two different k states. In section 3.3.2 we derived the corresponding probability that an atom would be transferred during the pulse,

$$P_0 = \frac{\Omega^2}{\Omega^2+\delta^2}\sin^2\left(\sqrt{\Omega^2+\delta^2}\,\tau/2\right), \tag{B.7}$$

where Ω is the Rabi frequency (set by the beam power) and δ is the detuning from resonance. Assuming the Bragg beams are tuned to resonance for the $k = 0$ mode and impart a momentum q, we can express δ in terms of k_x using the Doppler term from Eq. (3.7), $\delta = \hbar k_x q/m$. The transferred fraction is then

$$\frac{N_r}{N} = \int \mathrm{d}k_x\, n_{\mathrm{tot}}(k_x)\cdot\frac{\Omega^2}{\Omega^2+(\hbar k_x q/m)^2}\sin^2\left(\sqrt{\Omega^2+(\hbar k_x q/m)^2}\,\tau/2\right). \tag{B.8}$$

Since, after integrating, the right hand side is effectively only a function of the temperature T for fixed box- and Bragg parameters, the transferred fraction constitutes a measurement of the temperature of the gas.

Appendix C

Inverse-Abel transform

We use the inverse-Abel transform to reconstruct the three-dimensional momentum distribution n_k from the two-dimensional profiles $n_k^{(2D)}$ obtained from our absorption images. Our 2D profiles are the integral of the three-dimensional distribution along the line of sight. If the 3D distribution is isotropic, the 2D one can be written in the form

$$n_k^{(2D)}(k) = \int_{-\infty}^{\infty} \mathrm{d}k'\, n_k([k^2 + k'^2]^{1/2}) = 2\int_k^{\infty} \mathrm{d}k'\, \frac{k'\, n_k(k')}{\sqrt{k'^2 - k^2}}\,. \tag{C.1}$$

The inverse-Abel transform inverts this integral, to give

$$n_k(k) = -\frac{1}{\pi}\int_k^{\infty} \frac{\mathrm{d}}{\mathrm{d}k'}\left[n_k^{(2D)}(k')\right] \frac{\mathrm{d}k'}{\sqrt{k'^2 - k^2}}\,. \tag{C.2}$$

Formally, this requires that the 3D distribution n_k falls to zero faster than $1/k$.

It is useful to consider the following special case: where $n_k^{(2D)}(k)$ is a power law for all k above some threshold k_0, i.e. $n_k^{(2D)}(k > k_0) \sim k^{-\gamma}$, the inverse-Abel transform yields $n_k(k > k_0) \sim k^{-(\gamma+1)}$. Note that this result is not strictly true if the power law does not extend to $k \to \infty$.

Since our $n_k^{(2D)}$ is discretised, with $k'_i \in \{k'_1, k'_2, ..., k'_{m-1}, k'_m\}$, we implement the integral as a sum, and differentiate $n_k^{(2D)}$ using finite differences. We also separate out the first term in the sum (at $k' = k$) and analytically approximate its contribution avoid divergent behaviour in the presence of statistical noise.

References

[1] M. H. Anderson, J. R. Ensher, M. R. Matthews, C. E. Wieman, and E. A. Cornell. *Observation of Bose–Einstein Condensation in a Dilute Atomic Vapor*. Science **269**, 198 (1995).

[2] K. B. Davis, M. O. Mewes, M. R. Andrews, N. J. van Druten, D. S. Durfee, D. M. Kurn, and W. Ketterle. *Bose–Einstein Condensation in a Gas of Sodium Atoms*. Phys. Rev. Lett. **75**, 3969 (1995).

[3] B. DeMarco and D. S. Jin. *Onset of Fermi Degeneracy in a Trapped Atomic Gas*. Science **285**, 1703 (1999).

[4] C. Chin, R. Grimm, P. Julienne, and E. Tiesinga. *Feshbach resonances in ultracold gases*. Rev. Mod. Phys. **82**, 1225 (2010).

[5] I. Bloch, J. Dalibard, and W. Zwerger. *Many-body physics with ultracold gases*. Rev. Mod. Phys. **80**, 885 (2008).

[6] J. Dalibard, F. Gerbier, G. Juzeliūnas, and P. Öhberg. *Colloquium: Artificial gauge potentials for neutral atoms*. Rev. Mod. Phys. **83**, 1523 (2011).

[7] D. M. Stamper-Kurn and M. Ueda. *Spinor Bose gases: Symmetries, magnetism, and quantum dynamics*. Rev. Mod. Phys. **85**, 1191 (2013).

[8] T. Langen, R. Geiger, and J. Schmiedmayer. *Ultracold Atoms Out of Equilibrium*. Annu. Rev. Condens. Matter Phys. **6**, 201 (2015).

[9] A. L. Gaunt, T. F. Schmidutz, I. Gotlibovych, R. P. Smith, and Z. Hadzibabic. *Bose–Einstein Condensation of Atoms in a Uniform Potential*. Phys. Rev. Lett. **110**, 200406 (2013).

[10] C. Eigen. *Realization of a Homogeneous Bose Gas with Tunable Interactions*. Master's thesis, University of Cambridge (2015).

[11] C. Eigen. *Exploring Interacting Bose Gases in and out of Equilibrium*. Ph.D. thesis, University of Cambridge (2019).

[12] L. Chomaz, L. Corman, T. Bienaimé, R. Desbuquois, C. Weitenberg, S. Nascimbène, J. Beugnon, and J. Dalibard. *Emergence of coherence via transverse condensation in a uniform quasi-two-dimensional Bose gas*. Nat. Commun. **6**, 6162 (2015).

[13] B. Mukherjee, Z. Yan, P. B. Patel, Z. Hadzibabic, T. Yefsah, J. Struck, and M. W. Zwierlein. *Homogeneous Atomic Fermi Gases*. Phys. Rev. Lett. **118**, 123401 (2017).

[14] K. Hueck, N. Luick, L. Sobirey, J. Siegl, T. Lompe, and H. Moritz. *Two-Dimensional Homogeneous Fermi Gases*. Phys. Rev. Lett. **120**, 060402 (2018).

[15] C. Eigen, J. A. P. Glidden, R. Lopes, N. Navon, Z. Hadzibabic, and R. P. Smith. *Universal Scaling Laws in the Dynamics of a Homogeneous Unitary Bose Gas*. Phys. Rev. Lett. **119**, 250404 (2017).

[16] C. Eigen, J. A. P. Glidden, R. Lopes, E. A. Cornell, R. P. Smith, and Z. Hadzibabic. *Universal prethermal dynamics of Bose gases quenched to unitarity*. Nature **563**, 221 (2018).

[17] L. H. Dogra, J. A. P. Glidden, T. A. Hilker, C. Eigen, E. A. Cornell, R. P. Smith, and Z. Hadzibabic. *Can Three-Body Recombination Purify a Quantum Gas?* Phys. Rev. Lett. **123**, 020405 (2019).

[18] J. A. P. Glidden, C. Eigen, L. H. Dogra, T. A. Hilker, R. P. Smith, and Z. Hadzibabic. *Bidirectional dynamic scaling in an isolated Bose gas far from equilibrium*. Nat. Phys. **17**, 457 (2021).

[19] S. N. Bose. *Plancks Gesetz und Lichtquantenhypothese*. Z. Phys. **26**, 178 (1924).

[20] A. Einstein. *Quantentheorie des einatomigen idealen Gases*. Sitzungsberichte der preussischen Akademie der Wissenschaften **22**, 261 (1924).

[21] A. Einstein. *Quantentheorie des einatomigen idealen Gases: 2. Abhandlung*. Sitzungsberichte der preussischen Akademie der Wissenschaften **1**, 3 (1925).

[22] C. Pethick and H. Smith. *Bose–Einstein Condensation in Dilute Gases*. Cambridge University Press, 2nd edition (2008).

[23] L. Pitaevskii and S. Stringari. *Bose–Einstein Condensation and Superfluidity*. Oxford University Press (2016).

[24] W. Pauli. *The Connection Between Spin and Statistics*. Phys. Rev. **58**, 716 (1940).

[25] D. V. Schroeder. *An Introduction to Thermal Physics*. Addison Wesley Longman (1999).

[26] C. J. Foot. *Atomic Physics*. Oxford University Press (2005).

[27] J. R. Taylor. *Scattering Theory*. John Wiley & Sons (1972).

[28] L. D. Landau and E. M. Lifshitz. *Quantum Mechanics: Non-Relativistic Theory*. Pergamon Press, New York (1977).

[29] E. Timmermans, P. Tommasini, M. Hussein, and A. Kerman. *Feshbach resonances in atomic Bose–Einstein condensates*. Phys. Rep. **315**, 199 (1999).

[30] T. G. Tiecke. *Feshbach resonances in ultracold mixtures of the fermionic quantum gases ^{6}Li and ^{40}K*. Ph.D. thesis, University of Amsterdam (2009).

[31] T. L. Nicholson, S. Blatt, B. J. Bloom, J. R. Williams, J. W. Thomsen, J. Ye, and P. S. Julienne. *Optical Feshbach resonances: Field-dressed theory and comparison with experiments*. Phys. Rev. A **92**, 022709 (2015).

[32] A. J. Moerdijk, B. J. Verhaar, and A. Axelsson. *Resonances in ultra-cold collisions of ^{6}Li, ^{7}Li and ^{23}Na*. Phys. Rev. A **51**, 4852 (1995).

[33] G. F. Gribakin and V. V. Flambaum. *Calculation of the scattering length in atomic collisions using the semiclassical approximation*. Phys. Rev. A **48**, 546 (1993).

[34] V. Efimov. *Energy levels arising from resonant two-body forces in a three-body system*. Phys. Lett. B **33**, 563 (1970).

[35] E. Braaten and H.-W. Hammer. *Efimov physics in cold atoms*. Ann. Phys. **322**, 120 (2007).

[36] C. Cohen-Tannoudji and D. Guéry-Odelin. *Advances in Atomic Physics: An Overview*. World Scientific, Singapore (2011).

[37] M. J. Davis, S. A. Gardiner, T. M. Hanna, N. Nygaard, N. P. Proukakis, and M. H. Szymańska. *Ch. 4: Introduction to Theoretical Modelling*, in *Quantum Gases: Finite Temperature and Non-Equilibrium Dynamics*, edited by N. Proukakis, S. Gardiner, M. Davis, and M. Szymańska, Imperial College Press (2013).

[38] K. Huang. *Statistical Mechanics*. Wiley, New York (1987).

[39] R. P. Smith. *Effects of Interactions on Bose–Einstein Condensation*, in *Universal Themes of Bose–Einstein Condensation*, edited by N. Proukakis, D. Snoke, and P. Littlewood, Cambridge University Press (2017).

[40] A. L. Gaunt. *Degenerate Bose Gases: Tuning Interactions & Geometry*. Ph.D. thesis, University of Cambridge (2014).

[41] R. L. D. Campbell, R. P. Smith, N. Tammuz, S. Beattie, S. Moulder, and Z. Hadzibabic. *Efficient production of large ^{39}K Bose–Einstein condensates*. Phys. Rev. A **82**, 063611 (2010).

[42] N. Tammuz. *Thermodynamics of ultracold ^{39}K atomic Bose gases with tuneable interactions*. Ph.D. thesis, University of Cambridge (2011).

[43] R. L. D. Campbell. *Thermodynamic properties of a Bose gas with tuneable interactions*. Ph.D. thesis, University of Cambridge (2011).

[44] S. Moulder. *Persistent Currents in Bose–Einstein Condensates*. Ph.D. thesis, University of Cambridge (2013).

[45] A. Suleymanzade. *Ultracold atoms experiment for trapping ^{39}K in an optical box trap*. Master's thesis, University of Cambridge (2014).

[46] D. Nath, R. K. Easwaran, G. Rajalakshmi, and C. S. Unnikrishnan. *Quantum-interference-enhanced deep sub-Doppler cooling of ^{39}K atoms in gray molasses*. Phys. Rev. A **88**, 053407 (2013).

[47] G. Salomon, L. Fouché, P. Wang, A. Aspect, P. Bouyer, and T. Bourdel. *Gray-molasses cooling of ^{39}K to a high phase-space density*. Europhys. Lett. **104**, 63002 (2013).

[48] G. Salomon, L. Fouché, S. Lepoutre, A. Aspect, and T. Bourdel. *All-optical cooling of ^{39}K to Bose–Einstein condensation*. Phys. Rev. A **90**, 033405 (2014).

[49] C. Fort, A. Bambini, L. Cacciapuoti, F. S. Cataliotti, M. Prevedelli, G. M. Tino, and M. Inguscio. *Cooling mechanisms in potassium magneto-optical traps*. Eur. Phys. J. D **3**, 113 (1998).

[50] R. W. Bowman, A. J. Wright, and M. J. Padgett. *An SLM-based Shack–Hartmann wavefront sensor for aberration correction in optical tweezers*. J. Opt. **12**, 124004 (2010).

[51] B. C. Platt and R. Shack. *History and principles of Shack–Hartmann wavefront sensing*. J. Refract. Surg. **17**, 573 (2001).

[52] J.-F. Clément, J.-P. Brantut, M. Robert-de-Saint-Vincent, R. A. Nyman, A. Aspect, T. Bourdel, and P. Bouyer. *All-optical runaway evaporation to Bose–Einstein condensation*. Phys. Rev. A **79**, 061406 (2009).

[53] I. Gotlibovych. *Degenerate Bose Gases in a Uniform Potential*. Ph.D. thesis, University of Cambridge (2014).

[54] R. Saint-Jalm, P. C. M. Castilho, É. Le Cerf, B. Bakkali-Hassani, J.-L. Ville, S. Nascimbene, J. Beugnon, and J. Dalibard. *Dynamical Symmetry and Breathers in a Two-Dimensional Bose Gas*. Phys. Rev. X **9**, 021035 (2019).

[55] C. D'Errico, M. Zaccanti, M. Fattori, G. Roati, M. Inguscio, G. Modugno, and A. Simoni. *Feshbach resonances in ultracold ^{39}K*. New J. Phys. **9**, 223 (2007).

[56] M. Lysebo and L. Veseth. *Feshbach resonances and transition rates for cold homonuclear collisions between ^{39}K and ^{41}K atoms*. Phys. Rev. A **81**, 032702 (2010).

[57] R. J. Fletcher, R. Lopes, J. Man, N. Navon, R. P. Smith, M. W. Zwierlein, and Z. Hadzibabic. *Two- and three-body contacts in the unitary Bose gas*. Science **355**, 377 (2017).

[58] C. Eigen, A. L. Gaunt, A. Suleymanzade, N. Navon, Z. Hadzibabic, and R. P. Smith. *Observation of Weak Collapse in a Bose–Einstein Condensate*. Phys. Rev. X **6**, 041058 (2016).

[59] G. Breit and I. I. Rabi. *Measurement of Nuclear Spin*. Phys. Rev. **38**, 2082 (1931).

[60] E. Arimondo, M. Inguscio, and P. Violino. *Experimental determinations of the hyperfine structure in the alkali atoms*. Rev. Mod. Phys. **49**, 31 (1977).

[61] A. Barker. *Spectroscopic Studies of a Homogeneous Bose–Einstein Condensate with Tunable Interactions*. Master's thesis, University of Cambridge (2016).

[62] W. Gerlach and O. Stern. *Der experimentelle Nachweis der Richtungsquantelung im Magnetfeld*. Z. Phys. **9**, 349 (1922).

[63] M. Kozuma, L. Deng, E. W. Hagley, J. Wen, R. Lutwak, K. Helmerson, S. L. Rolston, and W. D. Phillips. *Coherent splitting of Bose–Einstein condensed atoms with optically induced Bragg diffraction*. Phys. Rev. Lett. **82**, 871 (1999).

[64] J. Stenger, S. Inouye, A. P. Chikkatur, D. M. Stamper-Kurn, D. E. Pritchard, and W. Ketterle. *Bragg Spectroscopy of a Bose–Einstein Condensate*. Phys. Rev. Lett. **82**, 4569 (1999).

[65] K. G. H. Viebahn. *Bragg Spectroscopy of an Interacting Bose–Einstein Condensate*. Master's thesis, University of Cambridge and LMU Munich (2015).

[66] W. L. Bragg. *The Specular Reflection of X-rays*. Nature **90**, 410 (1912).

[67] W. L. Bragg. *The Diffraction of Short Electromagnetic Waves by a Crystal*. Proceedings of the Cambridge Philosophical Society **17**, 43 (1913).

[68] S. Diehl, A. Micheli, A. Kantian, B. Kraus, H. P. Büchler, and P. Zoller. *Quantum states and phases in driven open quantum systems with cold atoms*. Nat. Phys. **4**, 878 (2008).

[69] N. Syassen, D. M. Bauer, M. Lettner, T. Volz, D. Dietze, J. J. García-Ripoll, J. I. Cirac, G. Rempe, and S. Dürr. *Strong Dissipation Inhibits Losses and Induces Correlations in Cold Molecular Gases*. Science **320**, 1329 (2008).

[70] K. G. H. Vollbrecht, C. A. Muschik, and J. Ignacio Cirac. *Entanglement Distillation by Dissipation and Continuous Quantum Repeaters*. Phys. Rev. Lett. **107**, 120502 (2011).

[71] G. Barontini, L. Hohmann, F. Haas, J. Estève, and J. Reichel. *Deterministic generation of multiparticle entanglement by quantum Zeno dynamics*. Science **349**, 1317 (2015).

[72] B. Buča, J. Tindall, and D. Jaksch. *Non-stationary coherent quantum many-body dynamics through dissipation*. Nat. Commun. **10**, 1730 (2019).

[73] N. Dogra, M. Landini, K. Kroeger, L. Hruby, T. Donner, and T. Esslinger. *Dissipation-induced structural instability and chiral dynamics in a quantum gas*. Science **366**, 1496 (2019).

[74] E. I. Rodríguez Chiacchio and A. Nunnenkamp. *Dissipation-Induced Instabilities of a Spinor Bose–Einstein Condensate Inside an Optical Cavity*. Phys. Rev. Lett. **122**, 193605 (2019).

[75] M. H. Szymańska, J. Keeling, and P. B. Littlewood. *Non-Equilibrium Bose–Einstein Condensation in a Dissipative Environment*, in *Quantum Gases: Finite Temperature and Non-Equilibrium Dynamics*, edited by N. Proukakis, S. Gardiner, M. Davis, and M. Szymańska (2013).

[76] J. M. Muñoz, X. Wang, T. Hewitt, A. U. Kowalczyk, R. Sawant, and G. Barontini. *Dissipative Distillation of Supercritical Quantum Gases*. Phys. Rev. Lett. **125**, 020403 (2020).

[77] J. I. Cirac and P. Zoller. *Quantum Computations with Cold Trapped Ions*. Phys. Rev. Lett. **74**, 4091 (1995).

[78] D. A. Lidar, I. L. Chuang, and K. B. Whaley. *Decoherence-Free Subspaces for Quantum Computation*. Phys. Rev. Lett. **81**, 2594 (1998).

[79] A. Beige, D. Braun, B. Tregenna, and P. L. Knight. *Quantum Computing Using Dissipation to Remain in a Decoherence-Free Subspace*. Phys. Rev. Lett. **85**, 1762 (2000).

[80] J. T. Barreiro, M. Müller, P. Schindler, D. Nigg, T. Monz, M. Chwalla, M. Hennrich, C. F. Roos, P. Zoller, and R. Blatt. *An open-system quantum simulator with trapped ions*. Nature **470**, 486 (2011).

[81] D. S. Kothari and B. N. Srivasava. *Joule–Thomson Effect and Quantum Statistics*. Nature **140**, 970 (1937).

[82] T. F. Schmidutz, I. Gotlibovych, A. L. Gaunt, R. P. Smith, N. Navon, and Z. Hadzibabic. *Quantum Joule–Thomson Effect in a Saturated Homogeneous Bose Gas*. Phys. Rev. Lett. **112**, 040403 (2014).

[83] J. Söding, D. Guéry-Odelin, P. Desbiolles, F. Chevy, H. Inamori, and J. Dalibard. *Three-body decay of a rubidium Bose–Einstein condensate*. Appl. Phys. B **69**, 257 (1999).

[84] D. Guéry-Odelin and G. V. Shlyapnikov. *Excitation-assisted inelastic processes in trapped Bose–Einstein condensates*. Phys. Rev. A **61**, 013605 (1999).

[85] T. Weber, J. Herbig, M. Mark, H.-C. Nägerl, and R. Grimm. *Three-Body Recombination at Large Scattering Lengths in an Ultracold Atomic Gas*. Phys. Rev. Lett. **91**, 123201 (2003).

[86] M. Schemmer and I. Bouchoule. *Cooling a Bose Gas by Three-Body Losses*. Phys. Rev. Lett. **121**, 200401 (2018).

[87] I. Bouchoule, M. Schemmer, and C. Henkel. *Cooling phonon modes of a Bose condensate with uniform few body losses*. SciPost Phys. **5**, 043 (2018).

[88] J. R. Ensher, D. S. Jin, M. R. Matthews, C. E. Wieman, and E. A. Cornell. *Bose–Einstein Condensation in a Dilute Gas: Measurement of Energy and Ground-State Occupation*. Phys. Rev. Lett. **77**, 4984 (1996).

[89] F. Gerbier, J. H. Thywissen, S. Richard, M. Hugbart, P. Bouyer, and A. Aspect. *Critical Temperature of a Trapped, Weakly Interacting Bose Gas*. Phys. Rev. Lett. **92**, 030405 (2004).

[90] R. Meppelink, R. A. Rozendaal, S. B. Koller, J. M. Vogels, and P. van der Straten. *Thermodynamics of Bose–Einstein-condensed clouds using phase-contrast imaging*. Phys. Rev. A **81**, 053632 (2010).

[91] N. Tammuz, R. P. Smith, R. L. D. Campbell, S. Beattie, S. Moulder, J. Dalibard, and Z. Hadzibabic. *Can a Bose Gas Be Saturated?* Phys. Rev. Lett. **106**, 230401 (2011).

[92] V. V. Goldman, I. F. Silvera, and A. J. Leggett. *Atomic hydrogen in an inhomogeneous magnetic field: Density profile and Bose–Einstein condensation*. Phys. Rev. B **24**, 2870 (1981).

[93] D. A. Huse and E. Siggia. *The density distribution of a weakly interacting Bose gas in an external potential*. J. Low Temp. Phys. **46**, 137 (1982).

[94] V. N. Popov. *Functional Integrals and Collective Modes*. Cambridge University Press, Cambridge (1987).

[95] A. Griffin. *Conserving and gapless approximations for an inhomogeneous Bose gas at finite temperatures*. Phys. Rev. B **53**, 9341 (1996).

[96] S. Giorgini, L. P. Pitaevskii, and S. Stringari. *Condensate fraction and critical temperature of a trapped interacting Bose gas*. Phys. Rev. A **54**, R4633 (1996).

[97] Y. Kagan, B. V. Svistunov, and G. V. Shlyapnikov. *Effect of Bose condensation on inelastic processes in gases*. JETP Lett. **42**, 209 (1985).

[98] E. A. Burt, R. W. Ghrist, C. J. Myatt, M. J. Holland, E. A. Cornell, and C. E. Wieman. *Coherence, Correlations, and Collisions: What One Learns About Bose–Einstein Condensates from Their Decay*. Phys. Rev. Lett. **79**, 337 (1997).

[99] E. Haller, M. Rabie, M. J. Mark, J. G. Danzl, R. Hart, K. Lauber, G. Pupillo, and H.-C. Nägerl. *Three-Body Correlation Functions and Recombination Rates for Bosons in Three Dimensions and One Dimension*. Phys. Rev. Lett. **107**, 230404 (2011).

[100] H. J. Lewandowski, J. M. McGuirk, D. M. Harber, and E. A. Cornell. *Decoherence–Driven Cooling of a Degenerate Spinor Bose Gas*. Phys. Rev. Lett. **91**, 240404 (2003).

[101] R. Olf, F. Fang, G. E. Marti, A. MacRae, and D. M. Stamper-Kurn. *Thermometry and cooling of a Bose gas to 0.02 times the condensation temperature*. Nat. Phys. **11**, 720 (2015).

[102] Z. Shotan, O. Machtey, S. Kokkelmans, and L. Khaykovich. *Three-Body Recombination at Vanishing Scattering Lengths in an Ultracold Bose Gas*. Phys. Rev. Lett. **113**, 053202 (2014).

[103] M. Fattori, C. D'Errico, G. Roati, M. Zaccanti, M. Jona-Lasinio, M. Modugno, M. Inguscio, and G. Modugno. *Atom Interferometry with a Weakly Interacting Bose–Einstein Condensate*. Phys. Rev. Lett. **100**, 080405 (2008).

[104] C. R. Monroe, E. A. Cornell, C. A. Sackett, C. J. Myatt, and C. E. Wieman. *Measurement of Cs-Cs elastic scattering at $T = 30\,\mu K$*. Phys. Rev. Lett. **70**, 414 (1993).

[105] P. C. Hohenberg and B. I. Halperin. *Theory of dynamic critical phenomena*. Rev. Mod. Phys. **49**, 435 (1977).

[106] P. M. Chaikin and T. C. Lubensky. *Principles of Condensed Matter Physics*. Cambridge University Press (1995).

[107] M. Campostrini, M. Hasenbusch, A. Pelissetto, and E. Vicari. *Theoretical estimates of the critical exponents of the superfluid transition in ^{4}He by lattice methods*. Phys. Rev. B **74**, 144506 (2006).

[108] E. Burovski, J. Machta, N. Prokof'ev, and B. Svistunov. *High-precision measurement of the thermal exponent for the three-dimensional XY universality class*. Phys. Rev. B **74**, 132502 (2006).

[109] T. Donner, S. Ritter, T. Bourdel, A. Ottl, M. Köhl, and T. Esslinger. *Critical Behavior of a Trapped Interacting Bose Gas*. Science **315**, 1556 (2007).

[110] A. A. Pogorelov and I. M. Suslov. *On the critical exponents for the λ transition in liquid helium*. JETP Lett. **86**, 39 (2007).

[111] N. Goldenfeld. *Lectures on Phase Transitions and the Renormalization Group*. Westview Press (1992).

[112] T. W. B. Kibble. *Topology of cosmic domains and strings*. J. Phys. A **9**, 1387 (1976).

[113] W. H. Zurek. *Cosmological experiments in superfluid helium?* Nature **317**, 505 (1985).

[114] J. Beugnon and N. Navon. *Exploring the Kibble–Zurek mechanism with homogeneous Bose gases*. J. Phys. B: At. Mol. Opt. Phys. **50**, 022002 (2017).

[115] A. del Campo and W. H. Zurek. *Universality of phase transition dynamics: Topological defects from symmetry breaking*. Int. J. Mod. Phys. A **29**, 1430018 (2014).

[116] N. Navon, A. L. Gaunt, R. P. Smith, and Z. Hadzibabic. *Critical dynamics of spontaneous symmetry breaking in a homogeneous Bose gas*. Science **347**, 167 (2015).

[117] A. J. Bray. *Theory of phase-ordering kinetics*. Adv. Phys. **43**, 357 (1994).

[118] E. V. Kozik and B. V. Svistunov. *Theory of Decay of Superfluid Turbulence in the Low-Temperature Limit*. J. Low Temp. Phys. **156**, 215 (2009).

[119] M. Prüfer, P. Kunkel, H. Strobel, S. Lannig, D. Linnemann, C.-M. Schmied, J. Berges, T. Gasenzer, and M. K. Oberthaler. *Observation of universal dynamics in a spinor Bose gas far from equilibrium*. Nature **563**, 217 (2018).

[120] R. Micha and I. I. Tkachev. *Turbulent thermalization*. Phys. Rev. D **70**, 043538 (2004).

[121] J. Berges, A. Rothkopf, and J. Schmidt. *Nonthermal Fixed Points: Effective Weak Coupling for Strongly Correlated Systems Far from Equilibrium*. Phys. Rev. Lett. **101**, 041603 (2008).

[122] B. Nowak, J. Schole, D. Sexty, and T. Gasenzer. *Nonthermal fixed points, vortex statistics, and superfluid turbulence in an ultracold Bose gas*. Phys. Rev. A **85**, 043627 (2012).

[123] B. Nowak, J. Schole, and T. Gasenzer. *Universal dynamics on the way to thermalization*. New J. Phys. **16**, 093052 (2014).

[124] J. Berges, K. Boguslavski, S. Schlichting, and R. Venugopalan. *Universality Far from Equilibrium: From Superfluid Bose Gases to Heavy-Ion Collisions*. Phys. Rev. Lett. **114**, 061601 (2015).

[125] A. Piñeiro Orioli, K. Boguslavski, and J. Berges. *Universal self-similar dynamics of relativistic and nonrelativistic field theories near nonthermal fixed points*. Phys. Rev. D **92**, 025041 (2015).

[126] I. Chantesana, A. Piñeiro Orioli, and T. Gasenzer. *Kinetic theory of nonthermal fixed points in a Bose gas*. Phys. Rev. A **99**, 043620 (2019).

[127] A. N. Mikheev, C.-M. Schmied, and T. Gasenzer. *Low-energy effective theory of nonthermal fixed points in a multicomponent Bose gas*. Phys. Rev. A **99**, 063622 (2019).

[128] C.-M. Schmied, A. N. Mikheev, and T. Gasenzer. *Non-thermal fixed points: Universal dynamics far from equilibrium*. Int. J. Mod. Phys. A **34**, 1941006 (2019).

[129] S. Bhattacharyya, J. F. Rodriguez-Nieva, and E. Demler. *Universal Prethermal Dynamics in Heisenberg Ferromagnets*. Phys. Rev. Lett. **125**, 230601 (2020).

[130] J. Berges, K. Boguslavski, M. Mace, and J. M. Pawlowski. *Gauge-invariant condensation in the nonequilibrium quark-gluon plasma*. Phys. Rev. D **102**, 034014 (2020).

[131] K. Fujimoto, R. Hamazaki, and Y. Kawaguchi. *Family–Vicsek Scaling of Roughness Growth in a Strongly Interacting Bose Gas*. Phys. Rev. Lett. **124**, 210604 (2020).

[132] F. Family and T. Vicsek. *Scaling of the active zone in the Eden process on percolation networks and the ballistic deposition model*. J. Phys. A **18**, L75 (1985).

[133] M. Kardar, G. Parisi, and Y.-C. Zhang. *Dynamic Scaling of Growing Interfaces*. Phys. Rev. Lett. **56**, 889 (1986).

[134] B. V. Svistunov. *Highly nonequilibrium Bose condensation in a weakly interacting gas*. J. Moscow Phys. Soc. **1**, 373 (1991).

[135] D. V. Semikoz and I. I. Tkachev. *Kinetics of Bose Condensation*. Phys. Rev. Lett. **74**, 3093 (1995).

[136] N. G. Berloff and B. V. Svistunov. *Scenario of strongly nonequilibrated Bose–Einstein condensation*. Phys. Rev. A **66**, 013603 (2002).

[137] S. Dyachenko, A. C. Newell, A. Pushkarev, and V. E. Zakharov. *Optical turbulence: weak turbulence, condensates and collapsing filaments in the nonlinear Schrödinger equation*. Physica D **57**, 96 (1992).

[138] N. Navon, A. L. Gaunt, R. P. Smith, and Z. Hadzibabic. *Emergence of a turbulent cascade in a quantum gas*. Nature **539**, 72 (2016).

[139] N. Navon, C. Eigen, J. Zhang, R. Lopes, A. L. Gaunt, K. Fujimoto, M. Tsubota, R. P. Smith, and Z. Hadzibabic. *Synthetic dissipation and cascade fluxes in a turbulent quantum gas*. Science **366**, 382 (2019).

[140] E. Levich and V. Yakhot. *Time development of coherent and superfluid properties in the course of a λ-transition*. J. Phys. A **11**, 2237 (1978).

[141] M. J. Davis, T. M. Wright, T. Gasenzer, S. A. Gardiner, and N. P. Proukakis. *Ch. 7: Formation of Bose–Einstein Condensates*, in *Universal Themes of Bose–Einstein Condensation*, edited by N. Proukakis, D. Snoke, and P. Littlewood, Cambridge University Press (2017).

[142] C. N. Weiler, T. W. Neely, D. R. Scherer, A. S. Bradley, M. J. Davis, and B. P. Anderson. *Spontaneous vortices in the formation of Bose–Einstein condensates*. Nature **455**, 948 (2008).

[143] B. Nowak, D. Sexty, and T. Gasenzer. *Superfluid turbulence: Nonthermal fixed point in an ultracold Bose gas*. Phys. Rev. B **84**, 020506 (2011).

[144] M. Karl, B. Nowak, and T. Gasenzer. *Universal scaling at nonthermal fixed points of a two-component Bose gas*. Phys. Rev. A **88**, 063615 (2013).

[145] M. Karl, B. Nowak, and T. Gasenzer. *Tuning universality far from equilibrium*. Sci. Rep. **3**, 2394 (2013).

[146] S. Erne, R. Bücker, T. Gasenzer, J. Berges, and J. Schmiedmayer. *Universal dynamics in an isolated one-dimensional Bose gas far from equilibrium*. Nature **563**, 225 (2018).

[147] D. W. Snoke and J. P. Wolfe. *Population dynamics of a Bose gas near saturation*. Phys. Rev. B **39**, 4030 (1989).

[148] H. T. C. Stoof. *Formation of the Condensate in a Dilute Bose Gas*. Phys. Rev. Lett. **66**, 3148 (1991).

[149] Yu. M. Kagan, B. V. Svistunov, and G. V. Shlyapnikov. *Kinetics of Bose condensation in an interacting Bose gas*. Sov. Phys. JETP **75**, 387 (1992).

[150] Yu. Kagan, G. V. Shlyapnikov, and J. T. M. Walraven. *Bose–Einstein Condensation in Trapped Atomic Gases*. Phys. Rev. Lett. **76**, 2670 (1996).

[151] K. Damle, S. N. Majumdar, and S. Sachdev. *Phase ordering kinetics of the Bose gas*. Phys. Rev. A **54**, 5037 (1996).

[152] C. W. Gardiner, P. Zoller, R. J. Ballagh, and M. J. Davis. *Kinetics of Bose–Einstein Condensation in a Trap*. Phys. Rev. Lett. **79**, 1793 (1997).

[153] H.-J. Miesner, D. M. Stamper-Kurn, M. R. Andrews, D. S. Durfee, S. Inouye, and W. Ketterle. *Bosonic Stimulation in the Formation of a Bose–Einstein Condensate*. Science **279**, 1005 (1998).

[154] M. Köhl, M. J. Davis, C. W. Gardiner, T. W. Hänsch, and T. Esslinger. *Growth of Bose–Einstein Condensates from Thermal Vapor*. Phys. Rev. Lett. **88**, 080402 (2002).

[155] M. J. Davis, T. M. Wright, P. B. Blakie, A. S. Bradley, R. J. Ballagh, and C. W. Gardiner. *Ch. 10: C-Field Methods for Non-Equilibrium Bose Gases*, in *Quantum Gases: Finite Temperature and Non-Equilibrium Dynamics*, edited by N. Proukakis, S. Gardiner, M. Davis, and M. Szymańska, Imperial College Press (2013).

[156] J. H. Lambert. *Observationes variae in mathesin puram*. Acta Helvetica, physico-mathematico-anatomico-botanico-medica **3**, 128 (1758).

[157] R. M. Corless, G. H. Gonnet, D. E. G. Hare, D. J. Jeffrey, and D. E. Knuth. *On the Lambert W function*. Advances in Computational Mathematics **5**, 329 (1996).

[158] A. M. Mood, F. A. Graybill, and D. C. Boes. *Introduction to the Theory of Statistics*. McGraw-Hill (1974).

[159] I. Chantesana. *Strong Wave Turbulence and Non-Thermal Fixed Points in a Kinetic Theory*. Ph.D. thesis, Ruprecht Karl University of Heidelberg (2018).

[160] I. Gotlibovych, T. F. Schmidutz, A. L. Gaunt, N. Navon, R. P. Smith, and Z. Hadzibabic. *Observing properties of an interacting homogeneous Bose–Einstein condensate: Heisenberg-limited momentum spread, interaction energy, and free-expansion dynamics*. Phys. Rev. A **89**, 061604 (2014).

[161] V. E. Zakharov, V. S. L'vov, and G. Falkovich. *Kolmogorov spectra of turbulence*. Springer Berlin (1992).

[162] E. W. Hagley, L. Deng, M. Kozuma, M. Trippenbach, Y. B. Band, M. Edwards, M. Doery, P. S. Julienne, K. Helmerson, S. L. Rolston, and W. D. Phillips. *Measurement of the Coherence of a Bose–Einstein condensate*. Phys. Rev. Lett. **83**, 3112 (1999).

[163] F. Ferlaino, A. Zenesini, M. Berninger, B. Huang, H. C. Nägerl, and R. Grimm. *Efimov Resonances in Ultracold Quantum Gases*. Few-Body Syst. **51**, 113 (2011).

[164] M. Inguscio, W. Ketterle, and C. Salomon, eds. *Proceedings of the International School of Physics "Enrico Fermi": Ultra-cold Fermi Gases*. IOS Press (2007).

[165] W. Zwerger, ed. *The BCS-BEC Crossover and the Unitary Fermi Gas*. Springer (2012).

[166] M. W. Zwierlein. *Superfluidity in ultracold atomic Fermi gases*, in *Novel Superfluids* (Vol. 2), edited by K.-H. Bennemann and J. B. Ketterson, Oxford University Press (2014).

[167] C. A. Regal, M. Greiner, and D. S. Jin. *Observation of Resonance Condensation of Fermionic Atom Pairs*. Phys. Rev. Lett. **92**, 040403 (2004).

[168] M. W. Zwierlein, C. A. Stan, C. H. Schunck, S. M. F. Raupach, A. J. Kerman, and W. Ketterle. *Condensation of Pairs of Fermionic Atoms near a Feshbach Resonance*. Phys. Rev. Lett. **92**, 120403 (2004).

[169] C. Chin, M. Bartenstein, A. Altmeyer, S. Riedl, S. Jochim, J. Hecker Denschlag, and R. Grimm. *Observation of the Pairing Gap in a Strongly Interacting Fermi Gas*. Science **305**, 1128 (2004).

[170] T. Bourdel, L. Khaykovich, M. E. Cubizolles, J. Zhang, F. Chevy, M. Teichmann, L. Tarruell, S. J. J. M. F. Kokkelmans, and C. Salomon. *Experimental Study of the BEC-BCS Crossover Region in Lithium 6*. Phys. Rev. Lett. **93**, 050401 (2004).

[171] J. Kinast, S. L. Hemmer, M. E. Gehm, A. Turlapov, and J. E. Thomas. *Evidence for Superfluidity in a Resonantly Interacting Fermi Gas*. Phys. Rev. Lett. **92**, 150402 (2004).

[172] M. W. Zwierlein, J. R. Abo-Shaeer, A. Schirotzek, C. H. Schunck, and W. Ketterle. *Vortices and superfluidity in a strongly interacting Fermi gas*. Nature **435**, 1047 (2005).

[173] L. Radzihovsky, J. Park, and P. B. Weichman. *Superfluid Transitions in Bosonic Atom-Molecule Mixtures near a Feshbach Resonance*. Phys. Rev. Lett. **92**, 160402 (2004).

[174] M. W. J. Romans, R. A. Duine, S. Sachdev, and H. T. C. Stoof. *Quantum Phase Transition in an Atomic Bose Gas with a Feshbach Resonance*. Phys. Rev. Lett. **93**, 020405 (2004).

[175] S. Piatecki and W. Krauth. *Efimov-driven phase transitions of the unitary Bose gas*. Nat. Commun. **5**, 3503 (2014).

[176] S. Cowell, H. Heiselberg, I. E. Mazets, J. Morales, V. R. Pandharipande, and C. J. Pethick. *Cold Bose Gases with Large Scattering Lengths*. Phys. Rev. Lett. **88**, 210403 (2002).

[177] T.-L. Ho. *Universal Thermodynamics of Degenerate Quantum Gases in the Unitarity Limit*. Phys. Rev. Lett. **92**, 090402 (2004).

[178] J. M. Diederix, T. C. F. van Heijst, and H. T. C. Stoof. *Ground state of a resonantly interacting Bose gas*. Phys. Rev. A **84**, 033618 (2011).

[179] W. Li and T.-L. Ho. *Bose Gases near Unitarity*. Phys. Rev. Lett. **108**, 195301 (2012).

[180] D. Borzov, M. S. Mashayekhi, S. Zhang, J.-L. Song, and F. Zhou. *Three-dimensional Bose gas near a Feshbach resonance*. Phys. Rev. A **85**, 023620 (2012).

[181] X. Yin and L. Radzihovsky. *Quench dynamics of a strongly interacting resonant Bose gas*. Phys. Rev. A **88**, 063611 (2013).

[182] A. G. Sykes, J. P. Corson, J. P. D'Incao, A. P. Koller, C. H. Greene, A. M. Rey, K. R. A. Hazzard, and J. L. Bohn. *Quenching to unitarity: Quantum dynamics in a three-dimensional Bose gas*. Phys. Rev. A **89**, 021601 (2014).

[183] M. Rossi, L. Salasnich, F. Ancilotto, and F. Toigo. *Monte Carlo simulations of the unitary Bose gas*. Phys. Rev. A **89**, 041602 (2014).

[184] H. T. C. Stoof and J. J. R. M. van Heugten. *Resummation of Infrared Divergencies in the Theory of Atomic Bose Gases*. J. Low Temp. Phys. **174**, 159 (2014).

[185] S.-J. Jiang, W.-M. Liu, G. W. Semenoff, and F. Zhou. *Universal Bose gases near resonance: A rigorous solution*. Phys. Rev. A **89**, 033614 (2014).

[186] A. Rançon and K. Levin. *Equilibrating dynamics in quenched Bose gases: Characterizing multiple time regimes*. Phys. Rev. A **90**, 021602 (2014).

[187] S. Laurent, X. Leyronas, and F. Chevy. *Momentum Distribution of a Dilute Unitary Bose Gas with Three-Body Losses*. Phys. Rev. Lett. **113**, 220601 (2014).

[188] D. H. Smith, E. Braaten, D. Kang, and L. Platter. *Two-Body and Three-Body Contacts for Identical Bosons near Unitarity*. Phys. Rev. Lett. **112**, 110402 (2014).

[189] S.-J. Jiang, J. Maki, and F. Zhou. *Long-lived universal resonant Bose gases*. Phys. Rev. A **93**, 043605 (2016).

[190] F. Chevy and C. Salomon. *Strongly correlated Bose gases*. J. Phys. B: At. Mol. Opt. Phys. **49**, 192001 (2016).

[191] T. Comparin and W. Krauth. *Momentum Distribution in the Unitary Bose Gas from First Principles*. Phys. Rev. Lett. **117**, 225301 (2016).

[192] X. Yin and L. Radzihovsky. *Postquench dynamics and prethermalization in a resonant Bose gas*. Phys. Rev. A **93**, 033653 (2016).

[193] Y. Ding and C. H. Greene. *Renormalized contact interaction in degenerate unitary Bose gases*. Phys. Rev. A **95**, 053602 (2017).

[194] J. Carlson, S. Gandolfi, U. van Kolck, and S. A. Vitiello. *Ground-State Properties of Unitary Bosons: From Clusters to Matter*. Phys. Rev. Lett. **119**, 223002 (2017).

[195] M. W. C. Sze, A. G. Sykes, D. Blume, and J. L. Bohn. *Hyperspherical lowest-order constrained-variational approximation to resonant Bose–Einstein condensates*. Phys. Rev. A **97**, 033608 (2018).

[196] V. E. Colussi, J. P. Corson, and J. P. D'Incao. *Dynamics of Three-Body Correlations in Quenched Unitary Bose Gases*. Phys. Rev. Lett. **120**, 100401 (2018).

[197] V. E. Colussi, S. Musolino, and S. J. J. M. F. Kokkelmans. *Dynamical formation of the unitary Bose gas*. Phys. Rev. A **98**, 051601 (2018).

[198] J. P. D'Incao, J. Wang, and V. E. Colussi. *Efimov Physics in Quenched Unitary Bose Gases*. Phys. Rev. Lett. **121**, 023401 (2018).

[199] V. E. Colussi, B. E. van Zwol, J. P. D'Incao, and S. J. J. M. F. Kokkelmans. *Bunching, clustering, and the buildup of few-body correlations in a quenched unitary Bose gas*. Phys. Rev. A **99**, 043604 (2019).

[200] E. J. Halperin, M. W. C. Sze, J. P. Corson, and J. L. Bohn. *Stable production of a strongly interacting Bose–Einstein condensate via mode matching*. Phys. Rev. A **100**, 013608 (2019).

[201] M. W. C. Sze and J. L. Bohn. *Two-step production of resonant Bose–Einstein condensates*. Phys. Rev. A **99**, 033606 (2019).

[202] S. Musolino, V. E. Colussi, and S. J. J. M. F. Kokkelmans. *Pair formation in quenched unitary Bose gases*. Phys. Rev. A **100**, 013612 (2019).

[203] A. Muñoz de las Heras, M. M. Parish, and F. M. Marchetti. *Early-time dynamics of Bose gases quenched into the strongly interacting regime*. Phys. Rev. A **99**, 023623 (2019).

[204] C. Gao, M. Sun, P. Zhang, and H. Zhai. *Universal Dynamics of a Degenerate Bose Gas Quenched to Unitarity*. Phys. Rev. Lett. **124**, 040403 (2020).

[205] N. Navon, S. Piatecki, K. Günter, B. Rem, T. C. Nguyen, F. Chevy, W. Krauth, and C. Salomon. *Dynamics and Thermodynamics of the Low-Temperature Strongly Interacting Bose Gas*. Phys. Rev. Lett. **107**, 135301 (2011).

[206] B. S. Rem, A. T. Grier, I. Ferrier-Barbut, U. Eismann, T. Langen, N. Navon, L. Khaykovich, F. Werner, D. S. Petrov, F. Chevy, and C. Salomon. *Lifetime of the Bose Gas with Resonant Interactions*. Phys. Rev. Lett. **110**, 163202 (2013).

[207] R. J. Fletcher, A. L. Gaunt, N. Navon, R. P. Smith, and Z. Hadzibabic. *Stability of a Unitary Bose Gas*. Phys. Rev. Lett. **111**, 125303 (2013).

[208] P. Makotyn, C. E. Klauss, D. L. Goldberger, E. A. Cornell, and D. S. Jin. *Universal dynamics of a degenerate unitary Bose gas*. Nat. Phys. **10**, 116 (2014).

[209] U. Eismann, L. Khaykovich, S. Laurent, I. Ferrier-Barbut, B. S. Rem, A. T. Grier, M. Delehaye, F. Chevy, C. Salomon, L.-C. Ha, and C. Chin. *Universal Loss Dynamics in a Unitary Bose Gas*. Phys. Rev. X **6**, 021025 (2016).

[210] C. E. Klauss, X. Xie, C. Lopez-Abadia, J. P. D'Incao, Z. Hadzibabic, D. S. Jin, and E. A. Cornell. *Observation of Efimov Molecules Created from a Resonantly Interacting Bose Gas*. Phys. Rev. Lett. **119**, 143401 (2017).

[211] R. J. Fletcher, J. Man, R. Lopes, P. Christodoulou, J. Schmitt, M. Sohmen, N. Navon, R. P. Smith, and Z. Hadzibabic. *Elliptic flow in a strongly interacting normal Bose gas*. Phys. Rev. A **98**, 011601 (2018).

[212] T. Kraemer, M. Mark, P. Waldburger, J. G. Danzl, C. Chin, B. Engeser, A. D. Lange, K. Pilch, A. Jaakkola, H.-C. Nägerl, and R. Grimm. *Evidence for Efimov quantum states in an ultracold gas of caesium atoms*. Nature **440**, 315 (2006).

[213] P. Naidon and S. Endo. *Efimov physics: a review*. Rep. Prog. Phys. **80**, 056001 (2017).

[214] J. P. D'Incao. *Few-body physics in resonantly interacting ultracold quantum gases*. J. Phys. B **51**, 043001 (2018).

[215] C. Langmack, R. Schmidt, and W. Zwerger. *Efimov states near a Feshbach resonance and the limits of van der Waals universality at finite background scattering length*. Phys. Rev. A **97**, 033623 (2018).

[216] Y. Yudkin, R. Elbaz, P. Giannakeas, C. H. Greene, and L. Khaykovich. *Coherent Superposition of Feshbach Dimers and Efimov Trimers*. Phys. Rev. Lett. **122**, 200402 (2019).

[217] R. Chapurin, X. Xie, M. J. Van de Graaff, J. S. Popowski, J. P. D'Incao, P. S. Julienne, J. Ye, and E. A. Cornell. *Precision Test of the Limits to Universality in Few-Body Physics*. Phys. Rev. Lett. **123**, 233402 (2019).

[218] F. Zhou and M. S. Mashayekhi. *Bose gases near resonance: Renormalized interactions in a condensate*. Ann. Phys. **328**, 83 (2013).

[219] T. D. Lee and C. N. Yang. *Many-Body Problem in Quantum Mechanics and Quantum Statistical Mechanics*. Phys. Rev. **105**, 1119 (1957).

[220] T. D. Lee, K. Huang, and C. N. Yang. *Eigenvalues and Eigenfunctions of a Bose System of Hard Spheres and Its Low-Temperature Properties*. Phys. Rev. **106**, 1135 (1957).

[221] P. O. Fedichev, M. W. Reynold, and G. V. Shlyapnikov. *Three-Body Recombination of Ultracold Atoms to a Weakly Bound s Level*. Phys. Rev. Lett. **77**, 2921 (1996).

[222] B. S. Rem. *The Road to the Unitary Bose Gas*. Ph.D. thesis, École Normale Supérieure de Paris (2013).

[223] C. H. Greene, B. Esry, and H. Suno. *A revised formula for 3-body recombination that cannot exceed the unitarity limit*. Nucl. Phys. A **737**, 119 (2004).

[224] J. P. D'Incao, H. Suno, and B. D. Esry. *Limits on Universality in Ultracold Three-Boson Recombination*. Phys. Rev. Lett. **93**, 123201 (2004).

[225] N. P. Mehta, S. T. Rittenhouse, J. P. D'Incao, J. von Stecher, and C. H. Greene. *General Theoretical Description of N-Body Recombination*. Phys. Rev. Lett. **103**, 153201 (2009).

[226] C. E. Klauss. *Resonantly Interacting Degenerate Bose Gas Oddities*. Ph.D. thesis, University of Colorado at Boulder (2018).

[227] C. A. Regal, C. Ticknor, J. L. Bohn, and D. S. Jin. *Creation of ultracold molecules from a Fermi gas of atoms*. Nature **424**, 47 (2003).

[228] E. Altman and A. Vishwanath. *Dynamic Projection on Feshbach Molecules: A Probe of Pairing and Phase Fluctuations*. Phys. Rev. Lett. **95**, 110404 (2005).

[229] E. Hodby, S. T. Thompson, C. A. Regal, M. Greiner, A. C. Wilson, D. S. Jin, E. A. Cornell, and C. E. Wieman. *Production Efficiency of Ultracold Feshbach Molecules in Bosonic and Fermionic Systems*. Phys. Rev. Lett. **94**, 120402 (2005).

[230] E. A. Donley, N. R. Claussen, S. T. Thompson, and C. E. Wieman. *Atom-molecule coherence in a Bose–Einstein condensate*. Nature **417**, 529 (2002).

[231] R. J. Wild, P. Makotyn, J. M. Pino, E. A. Cornell, and D. S. Jin. *Measurements of Tan's Contact in an Atomic Bose–Einstein Condensate*. Phys. Rev. Lett. **108**, 145305 (2012).

[232] B. Kain and H. Y. Ling. *Nonequilibrium states of a quenched Bose gas*. Phys. Rev. A **90**, 063626 (2014).

[233] S. Tan. *Energetics of a strongly correlated Fermi gas*. Ann. Phys. **323**, 2952 (2008).

[234] V. E. Colussi, H. Kurkjian, M. Van Regemortel, S. Musolino, J. van de Kraats, M. Wouters, and S. J. J. M. F. Kokkelmans. *Cumulant theory of the unitary Bose gas: Prethermal and Efimovian dynamics*. Phys. Rev. A **102**, 063314 (2020).

[235] F. Werner and Y. Castin. *General relations for quantum gases in two and three dimensions. II. Bosons and mixtures*. Phys. Rev. A **86**, 053633 (2012).

[236] M. Zaccanti, B. Deissler, C. D'Errico, M. Fattori, M. Jona-Lasinio, S. Müller, G. Roati, M. Inguscio, and G. Modugno. *Observation of an Efimov spectrum in an atomic system*. Nat. Phys. **5**, 586 (2009).

[237] S. Roy, M. Landini, A. Trenkwalder, G. Semeghini, G. Spagnolli, A. Simoni, M. Fattori, M. Inguscio, and G. Modugno. *Test of the Universality of the Three-Body Efimov Parameter at Narrow Feshbach Resonances*. Phys. Rev. Lett. **111**, 053202 (2013).

[238] P. M. A. Mestrom, J. Wang, C. H. Greene, and J. P. D'Incao. *Efimov–van der Waals universality for ultracold atoms with positive scattering lengths*. Phys. Rev. A **95**, 032707 (2017).

[239] O. Machtey, Z. Shotan, N. Gross, and L. Khaykovich. *Association of Efimov Trimers from a Three-Atom Continuum*. Phys. Rev. Lett. **108**, 210406 (2012).

[240] P. Arnold and G. Moore. *BEC Transition Temperature of a Dilute Homogeneous Imperfect Bose Gas*. Phys. Rev. Lett. **87**, 120401 (2001).

[241] G. Baym, J.-P. Blaizot, M. Holzmann, F. Laloë, and D. Vautherin. *Bose–Einstein transition in a dilute interacting gas*. Eur. Phys. J. B **24**, 107 (2001).

[242] M. Holzmann, J.-N. Fuchs, G. A. Baym, J.-P. Blaizot, and F. Laloë. *Bose–Einstein transition temperature in a dilute repulsive gas*. C. R. Physique **5**, 21 (2004).

[243] J. O. Andersen. *Theory of the weakly interacting Bose gas*. Rev. Mod. Phys. **76**, 599 (2004).

[244] R. P. Smith, R. L. D. Campbell, N. Tammuz, and Z. Hadzibabic. *Effects of Interactions on the Critical Temperature of a Trapped Bose Gas*. Phys. Rev. Lett. **106**, 250403 (2011).

[245] P. L. DeVries. *A First Course in Computational Physics*. Wiley (1984).

[246] R. Lopes, C. Eigen, N. Navon, D. Clément, R. P. Smith, and Z. Hadzibabic. *Quantum Depletion of a Homogeneous Bose–Einstein Condensate*. Phys. Rev. Lett. **119**, 190404 (2017).